MONTE CARLO SIMULATIONS OF THE ABC-STACKED KAGOME SPIN STRUCTURE OF XY AND HEISENBERG MODELS

VAHID HEMMATI

Monte Carlo Simulations of the ABC-Stacked Kagome Spin Structure of XY and Heisenberg Models.

by:

Vahid Hemmati

A thesis submitted to the
School of Graduate Studies
in partial fulfilment of the
requirement for the degree of
Master of Science

Computational Science Program
Memorial University of Newfoundland

November 2011

St. John's Newfoundland

Acknowledgment

I would like to thank **Memorial University of Newfoundland** to give me the opportunity of an academic life in the gentle society. Also, I am most grateful to Prof. Martin Plumer and Prof. John Whitehead for their kind and generous support. I appropriate kind help of Dr. Byron Southern. I should thank all other members of the research group; Timothy Fal, Jason Mercer, Martin LeBlanc, and Bassel Al-kadour.

I would like to dedicate my thesis to my mother; Gohartaj Sharifi.

Contents

List of Figures

List of Tables

Abstract

For many years, Ir-Mn alloys have been widely used by the magnetic storage industry in thin-film form as the antiferromagnetic pinning layer in GMR (Giant Magneto Resistance) and TMR (Tunnel Magneto Resistance) spin valves. Despite the technological importance of this structure, it has not previously been noted that the magnetic Mn-ions of fcc $IrMn_3$ reside on Kagome layers ABC stacked along $< 111 >$ axes normal to the film plane. Results of Monte Carlo simulations will be reported on the bulk fcc Kagome lattice for both XY and Heisenberg models including the eight NN exchange interactions. Degeneracies persist in the 3D case and there is strong evidence for a fluctuation-driven first-order transition to well-defined long-range order characterized as the layered q=0 120-degree spin structure. Effects of varying the inter-layer coupling are also examined.

List of Symbols and Abbreviations

$\vec{S}$, $\vec{S_i}$, $\vec{S_j}$	Spin
$\vec{H}$, h_j^z, $\vec{B}$	External magnetic field
$\vec{M}$	Magnetization
$\vec{M}_{AF}$	Net spin per area of the anti-ferromagnetic layer
E	Energy
$\Delta\sigma$	Inter-facial energy difference
T, T_N, T_C	Temperature, Néel temperature, critical temperature
J, J_{ij}, J'	Exchange interaction coefficient
FM, AF, NM	Ferromagnetic, anti-ferromagnetic, non-magnetic
t_{FM}	Thickness of ferromagnetic layer
$\vec{\mu_s}$	Spin magnetic moment
μ_0	Vacuum permeability
μ_B	Bohr Magneton
q	Electrical charge
g	g-factor
D	Anisotropy coefficient
k_β	Boltzmann constant
Z	Partition function
C	Specific heat
χ	Susceptibility
V_4(L)	Binder's fourth cumulant
V_4^M(L)	Magnetic cumulant
OP	Order parameter
m	Mass
H_{EB}	Exchange pinning field
τ, t	Reduced temperature
L	Lattice size
d	Dimension
PBC	Periodic boundary condition
MCS	Monte Carlo step
MNS	Magnetic neutron scattering
MA	Magnetic anisotropy
PEEM	Photo-emmission electron microscopy
MCA	Magneto-crystalline anisotropy
H	Hamiltonian
H_{dip}	Hamiltonian of dipole interaction
H_z	Zeeman Hamiltonian
H_{ex}	Exchange interaction Hamiltonian
H_{mca}	magneto-crystalline anisotropy Hamiltonian
fcc	Face-centered cubic
fct	Face-centered tetragonal
MC	Monte Carlo

Chapter 1

Introduction

1.1 Magnetic Sensors

Sensors that detect a wide variety of phenomena which rely on thin-film magnetic technology are in everyday use. Those include magnetometers, hard disk read-heads, as well as Magnetic Random Access Memory (MRAM). The technology in these devices is based on the spin-valve, which consists of two thin-film ferromagnetic (FM) layers as well as a stabilizing anti-ferromagnetic (AF) film.

Magnetometers are instruments to measure the strength and direction of a magnetic field. Very high sensitivity to detect magnetic fields have been reported in the spin-valve magnetometers [1]. Magnetometers are used in a wide range of applications. In archeology, magnetometers can detect shipwrecks and other buried or submerged objects; in mining, they are used to determine the direction of drilling; in the military they monitor submarine activity[1]; and in astronomy they predict cosmic activity, such as aurora borealis (see Fig 1.1). A grid of magnetometers around the world constantly measures the effect of the solar wind on the Earth's magnetic field. Also in mobile telephones and Global Positioning System (GPS) devices, magnetometers are used for

[1] On the defensive side, the Russian 'Goldfish' (titanium submarines) were designed and built at great expense to thwart such systems (pure titanium is non-magnetic)

showing direction.

Hard disk read-heads are devices that read the orientation of nano-scale magnetic grains embedded in hard disks. This device converts the external magnetic fields, coming from hard disk, into the electrical signals. High sensitivity in detecting small variation in the magnetic fields improves resolution in detecting the orientation of the magnetic grains over a small area of the hard disk. In other words, spin-valves enable hard disks with higher storage capacity. Fig 1.2 shows the effect on areal density by using spin-valve structures in hard disk read-heads.

Magnetic Random Access Memory(MRAM) is widely used to save data. Unlike electrical charge in conventional Random Access Memory (RAM), a magnetic field is used to store data in MRAM. The magnetic elements, with a spin-valve structure, make up a MRAM bit. The structure of spin-valves are also used to detect magnetic orientation of each cell on the MRAM. MRAM, as non-volatile memory, not only preserves information during loss of power, but also consumes less electrical energy. The random accessibility makes this device fast, as read-heads are able to select the shortest path over the MRAM grid to access a specific cell.

Figure 1.1: Aurora Borealis.
Picture from: travel.ezinemark.com

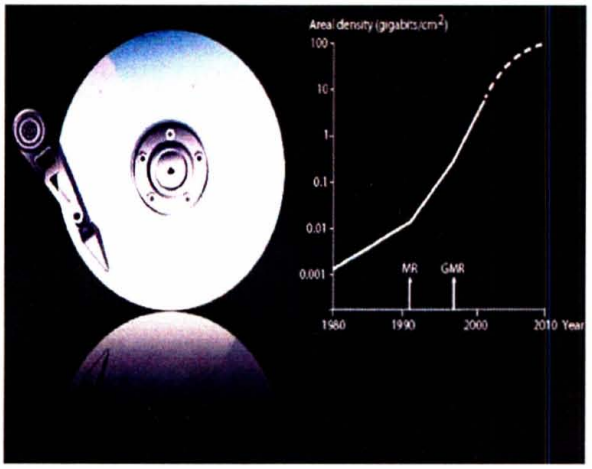

Figure 1.2: Gaint Magneto Resistance (GMR) spin-valve allowed for a significant progress in the capacity of the hard disks since 1997.
Picture from: www.physicscentral.com/explore/action/mr-research.cfm

1.2 Spin-Valves and Giant Magneto Resistance (GMR)

A spin-valve is a device consisting of two or more ferromagnetic layers. The electrical resistance of a spin-valve changes as a function of the relative alignment of the layer's magnetizations with respect to each other. This effect has its origin in spin-dependent momentum scattering. The electrical resistance for conducting electrons can be controlled by tuning the magnetic orientation of the layers. Spin dependent scattering has been studied as the main magnetic contribution to electrical resistance [2].

The schematic behavior of spin scattering from the interface of a ferromagnet is shown in Fig 1.3. As can be seen, the beam of electrons splits up into a reflected and transmitted beam. The reflected beam includes mostly spin-down electrons while the transmitted beam consists of spin-up electrons. When electrons of one spin encounter the FM layer with opposite magnetization, the electrons have a probability to flip their spins. The spin flips consume extra energy which it gains from the electrons in the FM layer. The energy dissipation of the electrons is measured as high resistance of the device. On the other hand, when electrons with the same spin alignment as the FM layer magnetization passes the device, no spin flip occurs, and consequently, these electrons do not loose

energy because of their spin. This is measured as a low resistance in the device.

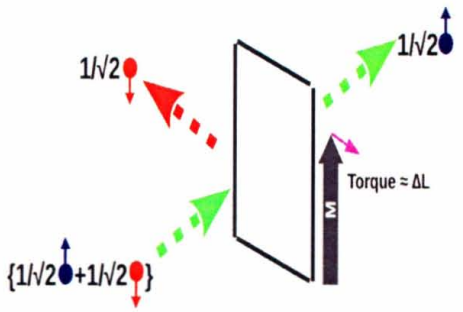

Figure 1.3: Spin-dependent Momentum Scattering

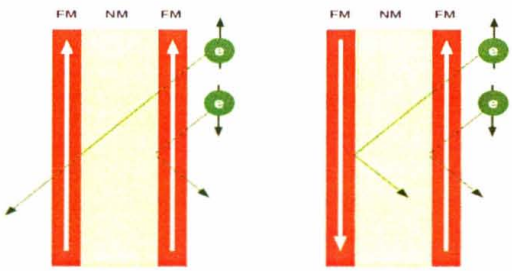

Figure 1.4: Schematic of a Spin-Valve Structure

Fig. 1.4 shows the schematic structure of a spin-valve. The spin-valve consists of two FM layers which are separated with a non-magnetic (NM) metal. In the spin-valve the current electrons encounter two FM layers, and energy dissipation of electrons depends on the angle of their spin orientation with respect to the magnetization of each FM layer. Due to this property, a spin-valve may act as a magnetic switch which is activated by magnetic field. When the magnetic orientation of the two layers is opposite, the device is highly resistive, and the electrical current drops down; on the contrary, when the magnetizations are aligned, the device is highly conductive, and no significant drop in electrical current is measured.

The crucial part of the spin-valve is in pinning the magnetization of one of the FM layers, so that its magnetization vector does not rotate in an external field. The method

used to pin the magnetization of the first layer should not affect the magnetization of the other one. Therefore, using a permanent magnet or hard FM may not provide a solution. A solution to this problem is to pin the FM layer by adding an AF layer adjacent to it [3]. This is known as Exchange Bias, or Exchange Pinning. The exchange pinning occurs due to quantum mechanical exchange coupling between spins across the interface. FM/AF coupling causes a stable magnetization in the adjacent FM layer. Since the AF layer has no magnetic moment, this layer does not respond to an external field. The study of FM/AF coupling has drawn the attention of many research groups [5]. Finding the appropriate multilayer structure with high efficiency is the challenge in manufacturing applicable magnetic switches [6]. The efforts of Peter Grunberg and Albert Fert as pioneers in discovering the change in electrical resistance as a function of external magnetic field, known as Giant Magneto-Resistance (GMR), was appreciated with the Nobel Prize in Physics in 2007[4](see Fig. 1.5).

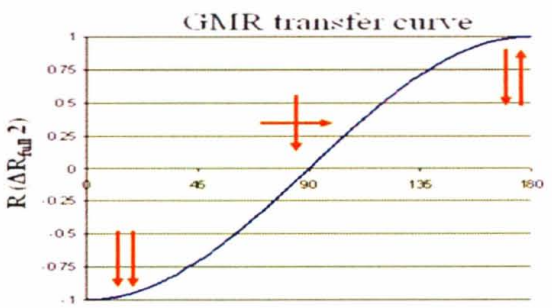

Figure 1.5: Change in electrical resistance as a function of relative angle between FM magnetizations

Fig. 1.6 illustrates the schematic structure of a simple read-head. The read-head consists of four parts; two FM layers (free layer and pinned layer), one NM layer (spacer layer), and one AF layer. The magnetization of the pinned layer is stabilized with the adjacent AF layer.

$IrMn_3$ is the most widely used material as the AF layer in read-heads due to its high

[4]Nobelprize.org

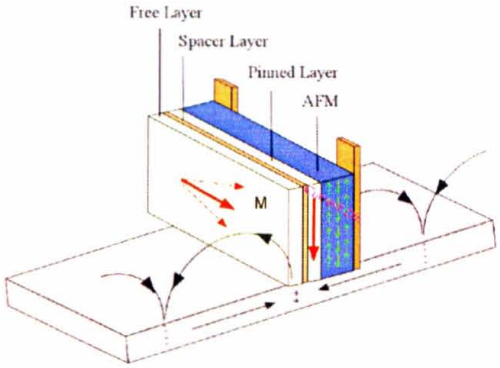

Figure 1.6: Read-Head Structure
Picture from: Dr. M. Plumer

ordering temperature and suitable interface pinning properties. The magnetic field of the media (black arrows in Fig. 1.6) causes a rotation in the magnetization of the free layer, but the pinned layer preserves its magnetization due to exchange pinning phenomenon. The electrical resistance of the system changes due to variation of the relative angle between magnetization in the free layer and the pinned layer, and this is detected by voltage from passing a current through the NM spacer layer. The high sensitivity of the device in detecting smaller and weaker fields, allows the memory cell to shrink, and consequently, the capacity of hard disks increases.

1.3 Exchange Pinning

The magnetic order of an AF material which consists of a spontaneous anti-parallel arrangement of neighboring spins disappears at high temperature. This perfect magnetic order at absolute zero temperature completely vanishes above the critical temperature called the Néel temperature.

At the Néel temperature, T_N in Fig. 1.7, the thermal energy is enough to destroy the magnetic order in the AF film. Note that exchange pinning leads to an exchange bias field, H_{EB} as shown in Fig. 1.7, which shifts the hysteresis loop (see appendix A). Below the Néel temperature, the spins in an AF film in a spin-valve interact with the adjacent

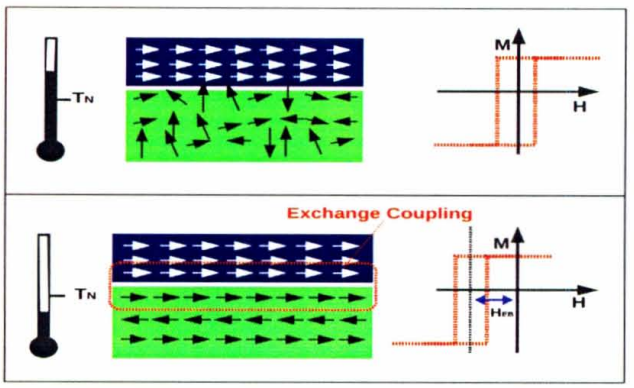

Figure 1.7: Exchange Pinning and Temperature

spins in the FM layer. The exchange coupling pins the spins in the FM layer. As a consequence, the orientation of the magnetization in the FM layer is not affected by the applying field which is weaker than pinning bias field, H_{EB}. Above the Néel temperature, the exchange coupling is still present, but this interaction does not determine a unique direction to pin the magnetization of FM layer due to the absence of any magnetic order on the AF interface. The temperature dependence of the magnetic order of the AF layer contributes crucially to create the exchange pinning in the multi-layer FM/AF system. In this thesis, the thermal behavior of the magnetic order in the AF $IrMn_3$ is investigated.

Since the discovery of exchange pinning in 1956 by W. H. Meiklejohn and C. P. Bean [3], there have been many theoretical models presented to explain the mechanism of this effect. Several of these models are reviewed below, and, despite the lack of comprehensiveness, this may offer a general picture to partially understand this phenomenon. The majority of models focus on the possible spin-configurations at the AF surface, emphasizing the substantial role of thermal behavior of AF layer which must be considered in any comprehensive study of exchange pinning. The Meiklejohn and Bean model, known as the direct exchange model, was the first model to describe the mechanism of exchange pinning. In this model, a direct exchange interaction between the magnetization of the FM layer, $\vec{M}_{FM}$, and the net spin per area of the AF layer, $\vec{M}_{AF}$, is assumed [3], and the

energy of the system is given by:

$$E_{Dir} = J\vec{M}_{AF} \cdot \vec{M}_{FM} \tag{1.1}$$

Another popular model is the Mauri model known as the AF spring model. In the Mauri model, a domain wall in the AF substrate is assumed. As can bee seen in Fig. 1.8, in the vicinity of the FM layer an interface of thickness ξ is formed where the uncompensated inter-facial moments[6] at the interface AF couple with the FM moments. On the other hand, in the centre of AF substrate, and far from FM layer, the magnetic moment of AF is aligned toward its uniaxial anisotropy (along x axis in Fig. 1.8). A domain wall is formed between these two layers. The assumption of a domain wall reduces the calculated exchange pinning field in agreement with experiments. Moreover, the x-ray observation confirms the existence of domain walls in some AF materials.

The coupling energy of this system is given by:

$$\mathrm{E} = -\vec{H} \cdot \hat{M} - J\left[\hat{M} \cdot \hat{m}\right] + \frac{\sigma}{2}\left[1 - \hat{m} \cdot \hat{u}\right] \tag{1.2}$$

where $\hat{M}$ is FM orientation, $\hat{m}$ is the net spin of AF at the interface, $\hat{u}$ is the direction

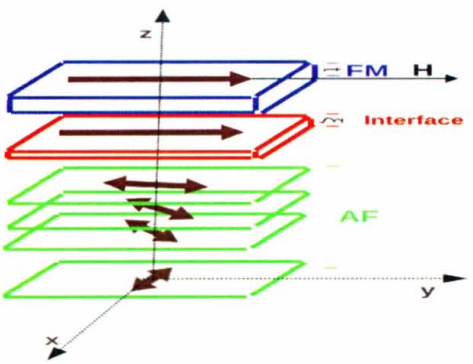

Figure 1.8: Mauri Model

of the uniaxial anisotropy axis of the AF layer, and σ is the energy of domain wall in the AF. A defect of this model[7] is revealed when the exchange pinning field is measured in very thin AF substrate. In very thin AF substrates, there is not sufficient space for

[6]Non zero magnetic moment over the surface of AF layer
[7]Paul Haney Ref. at http://www.ph.utexas.edu/ macdgrp/

domain wall; nevertheless, the measurements still show a significant exchange pinning [4].

In the Malozemoff model, which is known as the random field model, a statistical treatment of the random field model describes the effects of AF domain size on the magnitude of exchange pinning field. A random roughness on the surface causes a random local magnetic field. The surface spins are affected by this local magnetic field. This phenomenon on the surface eventually divides the AF into many domains, as shown in Fig. 1.9. The exchange and an additional uniaxial in-plane anisotropy play main roles in determining the size of these AF domains and consequently in determining the exchange pinning field. Malozemoff further states that the balance between applied field

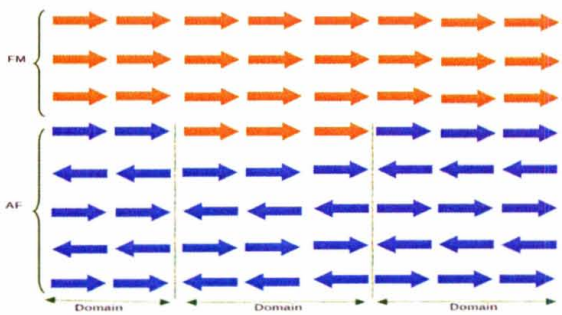

Figure 1.9: Domains in Malozemoff Model

pressure $2HM_{FM}t_{FM}$, on one hand, and the effective pressure from the inter-facial energy difference $\Delta\sigma$, on the other hand, determines the exchange pinning field [7].

$$H_{EB} = \frac{\Delta\sigma}{2M_{FM}t_{FM}} \tag{1.3}$$

Results from Photo-Emission Electron Microscopy (PEEM) confirm the theoretical prediction of the Malozemoff model of the existence of an inverse linear relationship between the exchange pinning field H_{EB} and domain size [8]. The Malozemoff model is successful in explaining many of the features of the exchange pinning. However, this model fails to justify some empirical results. As an example, the experimental observation of the tendency of the FM to align perpendicular to the AF easy axis has no justification in Malozemoff model [9].

The last model discussed here is the Koon/Butler model which is known as the spin-flop coupling model. In the Koon/Butler model, it is assumed that the AF spins in the interface are inclined slightly out of plane toward the FM layer. This surface spin configuration results in a net magnetic moment toward FM layer. The net magnetic moment interacts with FM spins and the new term in the energy, a spin-flop term, decreases the exchange pinning [11]. In contrast with the Mauri model, the Koon/Butler assumption does not require a thick AF substrate to give reasonable values for exchange pinning.

The energy of the spin-flop coupling is $J_{sf}(\hat{M} \cdot \hat{m})^2$. This term must be added to

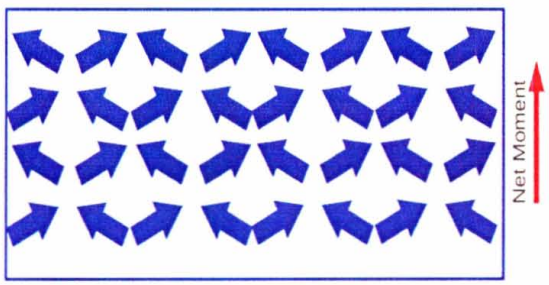

Figure 1.10: Spin-Flop in Koon/Butler Model

the energy expression 1.2; therefore, the energy in the Koon/Butler model is given as follows [12][7]:

$$E = -\vec{H} \cdot \hat{M} - J\left[\hat{M} \cdot \hat{m}\right] + J_{sf}\left[\hat{M} \cdot \hat{m}\right]^2 + \frac{\sigma}{2}\left[1 - \hat{m} \cdot \hat{u}\right] \tag{1.4}$$

A combination of the spin-flop coupling model and Malozemoff random field model has been used to find the exchange pinning field. The results showed significant compatibility with the measured values [9].

1.4 Phase Transitions

In a thermodynamic system, the transformation from one state of matter, or phase, to another phase passes through a threshold temperature where the symmetry of the ordered

[7]Paul Haney Ref. at http://www.ph.utexas.edu/ macdgrp/

phase is broken in order to create a new state in the system. At this temperature, which is called critical temperature (T_c), the temperature dependence of the free energy of the thermodynamic system may not be a well-behaved function. The phase transition is often accompanied by a discontinuity in the free energy at the critical temperature. A famous example of a phase transition is melting phenomenon, while thermal fluctuations break the microscopic symmetry of the crystal structure of a solid at the melting temperature, absorbing thermal energy shows no change in the temperature of the system. The peak in the specific heat curve, C, at this point reflects this behavior. Phase transitions can also occur between different magnetic states of a material. The interaction between the spins often forms a symmetric configuration in orientations known as a magnetic crystal. Breaking the symmetry of magnetic crystals occurs at the some specific temperatures, T_c. To study the phase transition, it is conventional to define a parameter which reflects

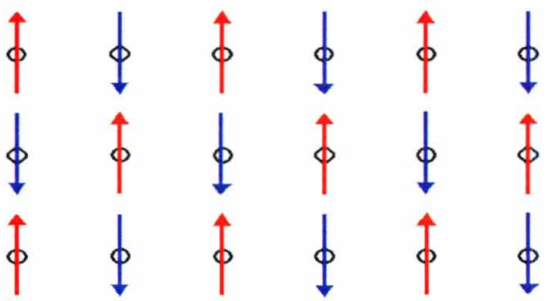

Figure 1.11: Schematic of an AF Magnetic Crystal in 2D

the symmetry of the system. This parameter, known as the order parameter, typically varies from zero to one. At absolute zero temperature, where the thermal fluctuation is minimum, order parameter has its maximum value which is one. The order parameter decreases with increasing temperature. At the critical temperature, T_c, the order parameter falls to zero. In FM systems, the magnetization can be used as the order parameter, while in AF systems the definition of order parameter is different. The fact that each AF magnetic lattice consists of several FM magnetic sub-lattices is used to define an order parameter based on magnetizations of these sub-lattices [13]. Fig 1.11 shows the magnetic lattice of square AF in 2D. As can be seen, this magnetic lattice consists of

two FM sub-lattices which are illustrated in red and blue. Phase transitions, observed in physical systems, are conventionally classified in two categories. The criteria of the classification is in discontinuity of the free energy of systems. First-order phase transitions exhibit a discontinuity in first derivatives of this energy with respect of thermodynamic variables, while in second-order phase transitions, the first derivatives of the free energy are continuous, but discontinuities are seen in the second derivate. Fig 1.12 shows the

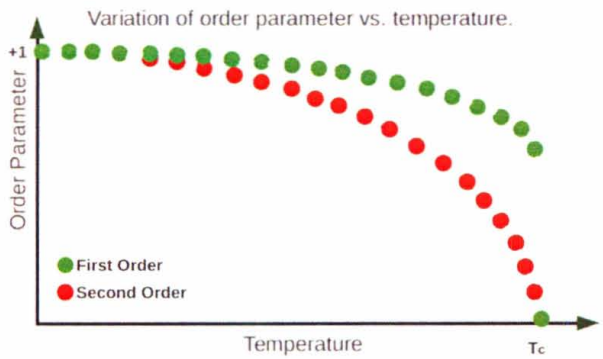

Figure 1.12: Order of Phase Transition

order parameters of two systems. As can be seen, in the second-order phase transition, the order parameter curve rises more smoothly than its counterpart in the first-order phase transition.

Around critical points of any continuous phase transition, the physical quantities behave universally. This means that this behavior is independent of the details of the physical interaction. The critical exponents, which are generally a function of the symmetry and dimension of systems and the range of interactions, are used to describe the critical behavior. The critical exponent, k, of any physical quantity, such as $f(T)$, as a function of temperature, T, is defined as follows [14][8]:

$$k = lim \frac{log\,|f(\tau)|}{log\,|\tau|} \tag{1.5}$$

$$\tau \to 0$$

where τ is the reduced temperature, and defined as $\tau = (T - T_c)/T_c$.

[8]Also http://en.wikipedia.org/wiki/Critical_exponent

The above definition assumes that the asymptotic behavior of the physical quantity, $f(\tau)$, when reduced temperature goes to zero, $\tau \to 0$, is as follows:

$$f(\tau) = A\tau^k(1 + b\tau^{k_1} + \cdots) \tag{1.6}$$

It is more conventional to write the equation 1.6 in the following form:

$$f(\tau) \propto \tau^k \quad , \ \tau \approx 0 \tag{1.7}$$

The calculation of critical exponents, even for simple models, is nontrivial. Despite the absence of a comprehensive theoretical proof for universality in the critical exponents, this theory is confirmed by experimental and computational data [10].

1.5 Magnetism in Condensed Matter

According to the Bohr-van Leeuwen theorem, there is no thermal equilibrium magnetization in a classical system [15]. Classical physics completely fails in predicting the existence of magnetism. In quantum physics, the concept of a particle's spin plays a significant role to describe the intrinsic magnetic moment of ions. The observable spin magnetic moment of a particle, $\vec{\mu}_s$, with electrical charge q, mass m, and spin angular momentum $\vec{S}$ is given by:

$$\vec{\mu}_s = -g\frac{q}{2m}\vec{S} \tag{1.8}$$

where g, called g-factor, is a dimensionless number which depends on the type of particle; for example, the g-factor is 2.0023 for the electron, while it is 5.586 for the proton. It is assumed that all magnetic properties arise from the interaction between atomic magnetic moments inside the materials. There are three well-known models, Heisenberg, xy and Ising models, to describe the magnetism in condensed matter. A tremendous amount of research has been done, based on these three models; therefore, these models are discussed in more detail in this thesis.

1.5.1 Heisenberg Model

In this model, atomic spin vectors $\vec{S}_i = (S_i^x, S_i^y, S_i^z)$ with a fixed length S, localized on lattice site i, interact with other magnetic moments and magnetic fields according to the following Hamiltonian:

$$H = H_{ex} + H_{mca} + H_{dip} + H_z \tag{1.9}$$

where the isotropic exchange interaction, H_{ex}, is given by:

$$H_{ex} = -\frac{1}{2} \sum_{<i,j>} J_{ij} \vec{S}_i \cdot \vec{S}_j \tag{1.10}$$

This term originates as a consequence of Coulomb interactions together with Pauli's exclusion principle and the antisymmetry of the total electronic wave-function(electrons as fermions) [16]. This interaction usually is short range and usually only include the nearest neighbors lattice sites. The symmetry condition, $J_{ij} = J_{ji}$, is always valid for this term. Furthermore, the sign of interaction coefficient, J_{ij}, determines the type of interaction between the i^{th} spin with the j^{th} spin and consequently their mutual arrangements. A negative coefficient forces the spins align in an anti-ferromagnetic fashion (in non-frustrated systems, anti-parallel), while a positive coefficient forces the spins to align in a ferromagnetic fashion [17].

Another important term in Hamiltonian 1.9 is the magneto-crystalline anisotropy, H_{mca}. The magneto-crystalline anisotropy (MCA), in its simplest form, represents the tendency of the material's spins to align along some specific axes in crystal structure, the easy-axes of the magnetization.

$$H_{mca} = \sum_i D(S_i^z)^2 \tag{1.11}$$

In Eq. 1.11, the z-axis defines the easy-axis of crystal providing D is negative. A positive value for the anisotropy coefficient, D, makes the z-axis as the hard-axis, and the spins prefer to lie in the xy-plane. This term is strongly affected by the spatial symmetry of the magnetic electron orbitals; therefore, in crystal structures, the symmetry of the

bravais lattice and the orbital angular momentum of magnetic electron in the atomic structure determine the strength of the MCA. For example for itinerant electron structure, where the orbital angular momentum is almost quenched, MCA is usually ignorable in comparison with the isotropic exchange interaction. This condition causes a small MCA in the bulk of transition-metals [17, 20].

In the case of thin films, the MCA term for the surface atoms is more complex than the corresponding translation value in the bulk due to broken symmetry at the surface. The surface MCA determines the domain size in the Malozemoff model for exchange pinning; furthermore, the perpendicular net momentum predicted in the Koon/Butler model may be explained by this term. Eq. 1.12 and Eq. 1.13 give the MCA energy for thin films and surfaces [17]. As can be seen, the energy is written separately as perpendicular and parallel terms with the respect to the surface plane (z-axis coincides with the surface normal axis).

$$H_{mca}^{\perp} = -\sum_{l,i} K_{l,i}^{\perp} (S_i^z)^l \tag{1.12}$$

$$H_{mca}^{\parallel} = -\sum_{i} \left(K_{2,i}^{\parallel} (S_i^x)^2 + K_{4,i}^{\parallel} \left((S_i^x)^4 + (S_i^y)^4 \right) + K_{6,i}^{\parallel} \left((S_i^+)^6 + (S_i^-)^6 \right) \right) \tag{1.13}$$

where ($S_i^{\pm} = S_i^x \pm i S_i^y$). The most frequent terms are shown in Eq. 1.13. These terms are used based on the symmetry of the film face. The unixial (twofold) term, the quartic (fourfold) term, and the hexagonal (sixfold) term are explicitly considered in this equation.

The magnetic dipole interaction, H_{dip} in Eq. 1.9, can be written as follows:

$$H_{dip} = \frac{\mu_0}{2} \sum_{ij} \frac{\mu_i \mu_j}{r_{ij}^5} \left[(\vec{S}_i \cdot \vec{S}_j) r_{ij}^2 + 3(\vec{r}_{ij} \cdot \vec{S}_i)(\vec{r}_{ij} \cdot \vec{S}_j) \right] \tag{1.14}$$

where μ_0 is the vacuum permeability, $4\pi \times 10^{-7} Vs/(Am)$, and the vector $\vec{r}_{ij}$ starts from the i^{th} site and ends at the j^{th}. The dipole interaction energy becomes important when FM thin films or multi-layer systems are studied. Including this term in simulations, such as Monte Carlo simulations, makes the computer code slow since it is longe range; and moreover, the magnitude of this term in AF systems is small in comparison with the

magnitude of other terms in Hamiltonian. Therefore, in simulations of AFs this term is usually ignored.

The Zeeman term, H_z, gives the interaction between an external magnetic field, $\vec{B}$, and the spins of the system.

$$H_z = -\mu_0 \mu_B \sum_i g_i \vec{B} \cdot \vec{S} \tag{1.15}$$

where g_i is the site-dependent Lande factor.

1.5.2 XY Model

In this model, magnetic moments are described by $\vec{S}_i = (S_i^x, S_i^y)$ or $\vec{S}_i = S(\mathbf{cos}\ \theta_i, \mathbf{sin}\ \theta_i)$, which is the two-dimensional spin localized on lattice site i. Due to the fixed magnitude for spins, it is convention to use polar coordinates in the xy model. Therefore the Hamiltonian of this model can be written as follows:

$$H = -\frac{1}{2} \sum_{<ij>} J_{ij}\ \ \mathbf{cos}(\theta_i - \theta_j) S^2 - \sum_i h_i\ \ \mathbf{cos}(\theta_i)\ S \tag{1.16}$$

where $\theta_i \in (-\pi, \pi]$, $h_i = |\mu_0 \mu_B\ g_i \vec{B}|$. This model can be considered as the asymptotic limit of the Heisenberg model when the z-axis is an extremely hard axis. In this case, the magneto-crystalline anisotropy term, Eq. 1.11, forces the spins to stay in xy plane due to $D \to \infty$. It is clear in this case, considering spins as quantities with only one degree of freedom, the polar angle, makes the simulation significantly faster.

1.5.3 Ising Model

In the Ising model, the spins are one-dimensional normal vectors; therefore, the spins only have two possible values, ± 1. This model was invented by W. Lenz in 1920, but E. Ising was the pioneer using this model to predict the magnetic property of one-dimensional crystals in 1924 [18]. The 1D Ising model shows no phase transition. This model has been used for more complex systems in higher dimensions. In this model, Hamiltonian

can be written as follows:

$$H = -\frac{1}{2}\sum_{<ij>} J_{ij}\ S_i S_j - \sum_i h_i^z S_i \tag{1.17}$$

with S_i=±1. Many scientists used to believe that the partition function for 2D Ising model as an analytical function of temperature could not show any singularity in physical quantities, especially in finite systems. Eventually, L. Onsager established an argument based on Ising model to abolish this idea.[19].

1.6 Magnetic States and Frustrated Systems

In AF magnetic structures, each spin wants to align anti-parallel to its nearest-neighbor due to the AF exchange interaction. Sometimes, the geometery of the lattice structure in AF systems makes the perfect AF arrangement impossible. Geometrical frustration occurs when the geometry of some lattice structures forbids simultaneous minimization of the exchange energy all the nearest neighbor pairs of sites of an AF. At absolute zero temperature, the spin-configurations of the system achieves its maximum order. Fig 1.13

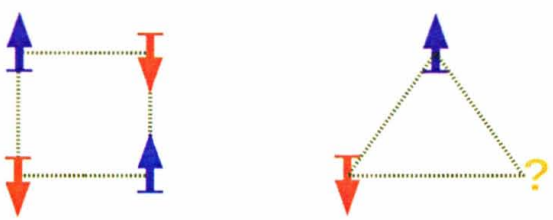

Figure 1.13: AF ground-state illustration frustration

indicates the AF magnetic structure in the square and the triangular lattices. As can be seen, in the square lattice, AF exchange energies acting between near neighbor sites are simultaneously minimized, while minimizing the interacting energies between all sites in the triangular lattice is impossible. Fig 1.14 shows the ground-state configuration for AF triangular structure in xy model, the alignment is not colinear; nevertheless, this configuration has the lowest possible energy. In this spin-configuration, the direction of each spin makes an angle of 120° with its adjacent spin. This means that there are only

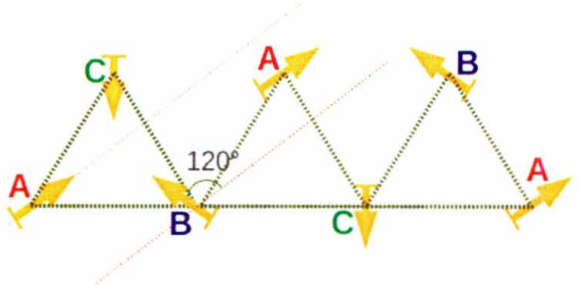

Figure 1.14: 120° spin structure of the triangular lattice.

three possible orientations for spins in the triangular structure. These three orientations are labeled A, B, and C in the picture [21].

1.6.1 Kagome Lattice

The 2D Kagome lattice, as shown in Fig. 1.15, consists of a triangular lattice with one-fourth of the sites removed. In nature some minerals like jarosites, $KFe_3^{3+}(OH)_6(SO_4)_2$, and HerbertSmithite, $ZnCu_3(OH)_6Cl_2$, are composed of the Kagome layers [22] [23]. The name, Kagome, is derived from the Japanese language. It means the pattern of holes in a specific basket which are called "Kago". Kagome, just like the triangular lattice, has a frustrated magnetic structure at absolute zero temperature; furthermore, this structure shows a great flexibility to create domain walls. Domain walls can be considered as the origin of the degeneracy in the energy of this system. This means because of forming domain walls in the Kagome structure many different spin-configurations have the same minimum energy.

This degeneracy of the system due to domain wall formation has an extensive characteristic. This means the number of possible spin-configurations with the same energy increases in direct proportion to the volume of the system. Consequently, the order of the degeneracy goes to infinity in a infinite system.

Fig. 1.16 shows two different spin-configurations, α and β, with the same energy. In the α structure, only one domain is formed; however, in the β structure, two domains are formed, above and below a wall. This wall consists of the horizontal line with the

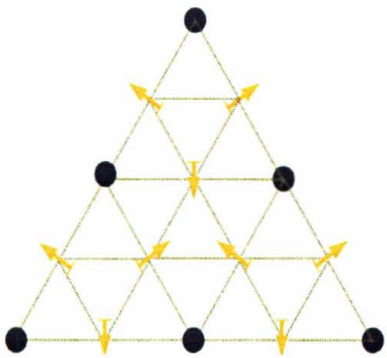

Figure 1.15: Schematic Kagome structure

C-type spin alignment and vacancies (black spots). Such a phenomenon is not seen in the triangular lattice structure. The Kagome has this property due to the strategic position of vacancies. These vacancies permit that the spins in each domain rotate with the angle of 120° with respect to their corresponding points in adjacent domains without costing energy. Domain wall formation in the AF substrate plays a significant role in the theory of exchange pinning.

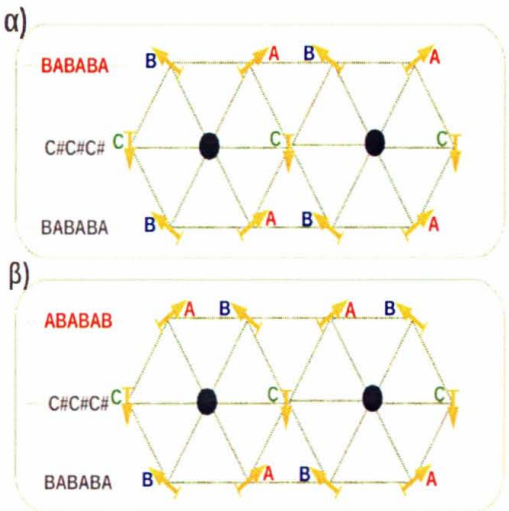

Figure 1.16: Degeneracy of two possible spin structures.

In three-dimensions, many interesting lattice structures can be composed by stacking triangular and Kagome layers. Among all of these structures, face centered cubic (fcc),

pyrochlore, and ABC-stacked Kagome, as three-dimensional frustrated systems, are the most interesting. The fcc structure can be viewed as stacked square lattices or triangular lattices along different crystallographic directions. Along [001] direction, fcc is consisted of square lattice, while along [111] direction, it is composed of stacked triangular lattices.

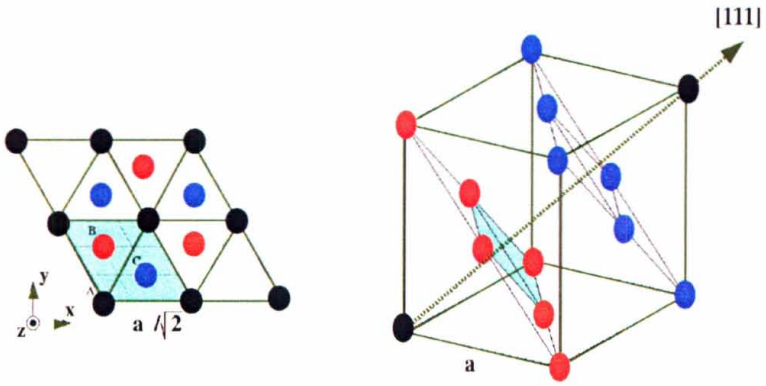

Figure 1.17: Face Centered Cubic FCC
(See Solid State Physics, by: Ashcroft/Mermin, Fig. 4-22)

In Fig. 1.17, layer structure of fcc along [111] is shown with three different colors, black, red, and blue. As can be seen, each unit cell consists of three layers which are denoted by A,B,and C, and each of these layers shifts with respect to the adjacent layers. In the other words, fcc is ABC-stacked triangular layers. Another interesting ABC-stacked structure is the ABC-stacked Kagome lattice which describes $IrMn_3$, studied in this thesis. As can be seen in Fig. 1.18, the only magnetic ions (Mn) in the fcc structure are in the center of the faces. Along [111] directions in this structure, there are 2D Kagome planes.

Pyrochlore is also composed of stacked layers, but this structure is formed from both Kagome and triangular lattices. In pyrochlores, the triangular layers interleave Kagome layers as shown in Fig. 1.19.

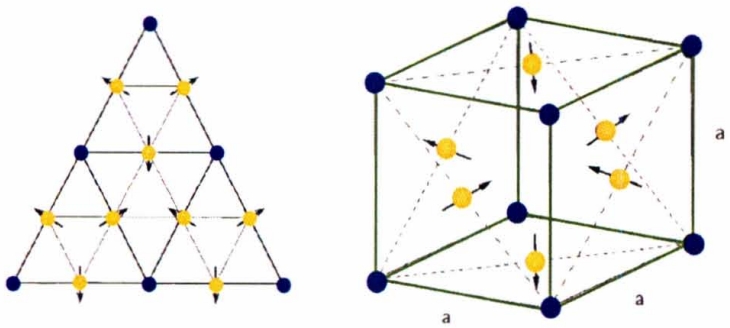

Figure 1.18: ABC-Stacked Kagome [30].

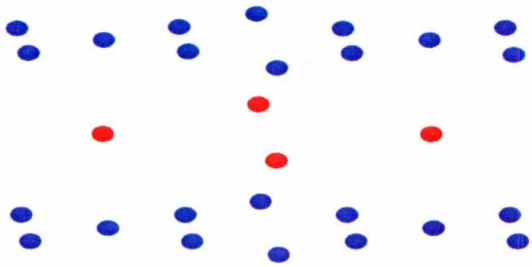

Figure 1.19: Pyrochlore structure composed of both triangular (read) and Kagome (blue) layers.

1.7 Monte Carlo Simulations

The Monte Carlo method provides a statistical approach to calculate the behavior of a system with many coupled degrees of freedom. A macroscopic system consists of many microscopic components. The link between macroscopic measurements and all possible microscopic configurations in many-body systems has raised crucial questions in science. Boltzmann constructed a significant mathematical bridge between these two worlds. In the microscopic frame, interaction energy tends to organize, while thermal energy is acting to disorder the system. In the Monte Carlo method, random numbers are used to produce the microscopic ensembles with a particular probability distribution of states. The Monte Carlo method, as a statistical approach, is usually compared with deterministic methods. In deterministic methods, the algorithm behaves predictably, and the sequence of states produced in any two runs is the same. In this particular method, a long list of details such as boundary conditions and the precise interaction equations are usually used to

solve a system of equations in each iteration. The advantage of the Monte Carlo method appears in dealing with systems with high degrees of freedoms, where the deterministic methods do not economically work. The name, Monte Carlo, dates back to 1940, when several famous scientists, including S. Ulam, were working on Manhattan Project in the Los Alamos National Laboratory. Monte Carlo casino was the place where Ulam's uncle would often gamble [24].

The Metropolis algorithm consists of a Markov chain of configurations. In this method, an arbitrary first spin configuration, S_{i-1}, is updated to construct a subsequent configuration, S_i, by using an appropriate probability function, $W(S_{i-1} \rightarrow S_i)$, that satisfies the condition of detailed balance:

$$\frac{W(S_I \rightarrow S_F)}{W(S_F \rightarrow S_I)} = \exp^{-\Delta E/k_\beta T} \tag{1.18}$$

where $\Delta E = E_F - E_I$ is the energy difference between final and initial spin-configurations, $k_\beta = 1.38 \times 10^{-23}\ J/K$ is Boltzmann constant and T is temperature. It can be shown that it is possible to generate a set of spin-configurations that form a canonical ensemble, with a probability, P, given by:

$$P \propto \exp^{(-E/k_\beta T)} \tag{1.19}$$

The following is a simple example of Metropolis algorithm [25]:

1. Take an arbitrary initial spin-configurations; $S_k = \{s_1, s_2, ..., s_n\}$.
2. Calculate the energy of the initial spin-configurations, $E(S_k)$.
3. Produce a new spin-configuration S_{k+1}.
   (a) Take i^{th} spin (randomly or in order of $i \in \{1, 2, 3, ..., n\}$).
   (b) Change i^{th} direction randomly to make trial configuration S_{tr}.
   (c) Calculate the new energy $E(S_{tr})$ of the trial configuration.
   (d) If $E(S_{tr}) \leq E(S_k)$, accept the trial; that is, set $S_{k+1} = S_{tr}$.

(e) If $E(S_{tr}) > E(S_k)$, accept with probability $P = exp^{(-\frac{\Delta E}{kT})}$:

Choose a uniform random number: $0 \leq r \leq 1$

i. Let $S_{k+1} = S_{tr}$; if $P \geq r$, accept

ii. Let $S_{k+1} = S_k$; if $P < r$, reject

This part of the algorithm is used to make only one "move". Equilibrium is achieved through many "moves" of every spin in the lattice or Monte Carlo Steps (MCS). The Ergodicity of the algorithm assumes that all possible states are produced given a sufficiently long simulation time. The length of required time, or the number of MCS, depends substantially on the geometry of the system and temperature. In highly frustrated systems and low temperature, the simulation time can be very long. As a matter of fact, to achieve a reasonable configuration, the system must produce enough accepted moves according to above-mentioned algorithm. In complicated systems, the orientation of each spin makes a small effect on the energy of the entire system. Producing an accepted "move" in such a sensitive system based on a random change is required; therefore, longer simulations must be expected for this type of system. The ABC-stacked Kagome and fcc lattice can be classified as complicated structures requiring longer simulation time.

To understand the thermal behavior of a system, multiple Monte Carlo simulations at different temperatures are usually used. It is assumed that the result at each temperature is completely independent of the result at any other temperature. This fact permits designing Monte Carlo simulation programs in a parallel fashion. In parallel programing, a massive task is broken down into many smaller tasks. These small tasks are separately performed by many CPUs; and eventually, the results are gathered in one output file. Running time is dramatically shortened with parallel programing. As a matter of fact, parallel programing is the only feasible way to simulate some systems. On the other hand, some complexities, such as race conditions, are involved in parallel programing. In programing, especially parallel programing, the race condition is a challenge when the result depends significantly on the sequence of events in such a way that the answer is quite

unpredictable due to different timings in using several processors. In the other words, the race condition occurs when the output is influenced by the timing of two signals. The Monte Carlo algorithm does not involve the race condition as long as the parallel programing is designed based on independent temperatures.

The result of Monte Carlo simulations is a canonical ensemble of possible spin-configurations of the system. From this measurable quantities can to be calculated in order to make contact with experimental data. Thermodynamics provides the mathematical instrument to perform this task. In the statistical simulation, the probability that the system is in a specific state, labeled by a, is simply related to the number of times that this state is reproduced in the ensemble. On the other hand, in thermodynamics, this probability is given as follows:

$$P_a = \frac{1}{Z} \exp^{-\beta E_a} \tag{1.20}$$

where $\beta = \frac{1}{kT}$ and E_a is the energy of the state a. Z is the normalization factor, called partition function, and it is defined as follows:

$$Z = \sum_a \exp^{-\beta E_a} \tag{1.21}$$

As a matter of fact, the expectation value of a quantity corresponds to the experimental measurement. The expectation value is the average of the quantity taken over the entire ensemble. This value for a measurable quantity, denoted Q, is calculated as follows:

$$\langle Q \rangle = \frac{1}{Z} \sum_a Q_a \exp^{-\beta E_a} \approx \frac{1}{N} \sum_{a'=1}^{N} Q_{a'} \tag{1.22}$$

where the first sum is over all possible states (a represents a state) , while the second sum is over the sequence of N states obtained from a Monte Carlo simulation and which are therefore selected with a probality $P_a = \frac{1}{Z} \exp^{-\beta E_a}$. Among the thermodynamic quantities, the magnetization $\vec{M}$, specific heat C, and susceptibility χ are calculated in this thesis. The specific heat of a system, which is the amount of the heat required to

change a substance's temperature, is defined as follows:

$$C(T) = \frac{\partial E(T)}{\partial T} \tag{1.23}$$

Eq. 1.23 is not the most useful form for statistical simulations. To calculate an equivalent formula of the specific heat in a statistical approach, the partition function plays an important role. From the partition function definition Eq. 1.21, we find:

$$\frac{\partial Z}{\partial \beta} = -\sum_a E_a \exp^{-\beta E_a} \tag{1.24}$$

comparing Eq. 1.24 to the formula of the expectation values, Eq. 1.21,we get:

$$\langle E \rangle = \frac{1}{Z}\sum_a E_a \exp^{-\beta E_a} = -\frac{1}{Z}\frac{\partial Z}{\partial \beta} = -\frac{\partial \log\, Z}{\partial \beta} \tag{1.25}$$

From Eq. 1.23 and using Eq. 1.25, specific heat is thus given by:

$$C(T) = \frac{\partial \langle E \rangle}{\partial T} = k_\beta \beta^2 \frac{\partial^2 \log\, Z}{\partial \beta^2} \tag{1.26}$$

From Eq. 1.22, the average of square energy is given by:

$$\langle E^2 \rangle = \frac{1}{Z}\sum_a E_a^2 \exp^{-\beta E_a} = \frac{1}{Z}\frac{\partial^2 Z}{\partial \beta^2} \tag{1.27}$$

Substitution of Eq. 1.27 and Eq. 1.25 in $\langle E^2 \rangle - \langle E \rangle^2$ gives :

$$\langle E^2 \rangle - \langle E \rangle^2 = \frac{1}{Z}\frac{\partial^2 Z}{\partial \beta^2} - \left(-\frac{1}{Z}\frac{\partial Z}{\partial \beta}\right)^2 = \frac{\partial^2 \log\, Z}{\partial \beta^2} \tag{1.28}$$

From Eq. 1.28 and Eq. 1.26, specific heat is then given by:

$$C(T) = k_\beta \beta^2 \left(\langle E^2(T) \rangle - \langle E(T) \rangle^2\right) \tag{1.29}$$

In statistical simulations, the average values of energy and squared energy are easily calculated; therefore, Eq. 1.29 is applicable for a statistical approach.

The magnetization per spin is defined as follows:

$$M(T) = \frac{1}{N}\left\langle \left| \sum_i^N \vec{S}_i \right| \right\rangle \tag{1.30}$$

where N is the number of the lattice sites. The magnetization can be considered as an

order parameter (OP) only for FM systems. In AF structures, the definition of order parameter depends on details of the spin structure; therefore, it must be calculated on a case by case basis. In statistical simulations of the magnetic structure of a system, the OP is calculable from the spin-configurations of each state. Furthermore, the expectation value of this quantity is simply calculated by accumulating the OP of all states divided by the number of the states in the ensemble. The thermodynamic susceptibility is the response of the system to a change of coupling field, and is defined as follows:

$$\chi = \frac{\partial \langle M \rangle}{\partial H} \tag{1.31}$$

where $\langle M \rangle$ is the average OP and H is the field which couples to $\vec{M}$. From 1.22 the average OP and squared OP are given by:

$$\langle M \rangle = \frac{1}{Z} \sum_a M_a \exp^{-\beta E_a} \tag{1.32}$$

$$\langle M^2 \rangle = \frac{1}{Z} \sum_a M_a^2 \exp^{-\beta E_a} \tag{1.33}$$

In the energy Eq. 1.9, the only term which includes the field is the Zeeman term; therefore, the derivative of the partition function to the respect of external field is given by:

$$\frac{\partial Z}{\partial H} = \beta \sum_a M_a \exp^{-\beta E_a} \tag{1.34}$$

From 1.31 and using 1.32, χ is given by:

$$\chi = \frac{\partial \langle M \rangle}{\partial H} = \frac{1}{Z^2} \left(Z \, (\frac{\partial \sum_a M_a \exp^{-\beta E_a}}{\partial H}) - \sum_a M_a \exp^{-\beta E_a} (\frac{\partial Z}{\partial H}) \right) \tag{1.35}$$

Thus, the susceptibility is given as:

$$\chi = \frac{1}{Z^2} \left(\beta \, (\sum_a M_a^2 \exp^{-\beta E_a} Z) - \beta (\sum_a M_a \exp^{-\beta E_a})^2 \right) = \beta (\langle M^2(T) \rangle - \langle M(T) \rangle^2) \tag{1.36}$$

Eq. 1.29 and Eq. 1.36 are actually the energy and OP variance which are known as the specific heat and susceptibility. Generally, variance shows how far a set of measurements are spread out from each other. In the case of a magnetic material, it is expected that

there will be peaks in the variance of energy and order parameter at phase transitions.

In studying phase transitions of magnetic systems using Monte Carlo methods, the order of the phase transition is often difficult to determine due to finite lattice size effects. True critical behavior only occurs in the thermodynamic limit of an infinite system. One of the suitable methods to investigate the order of a phase transition is finite-size scaling method. This method is based on the fact that for a first-order phase transition, the characteristic discontinuity in the energy and magnetization of the system behaves differently from the second-order phase transition. As can be seen in Fig. 1.20 [26],

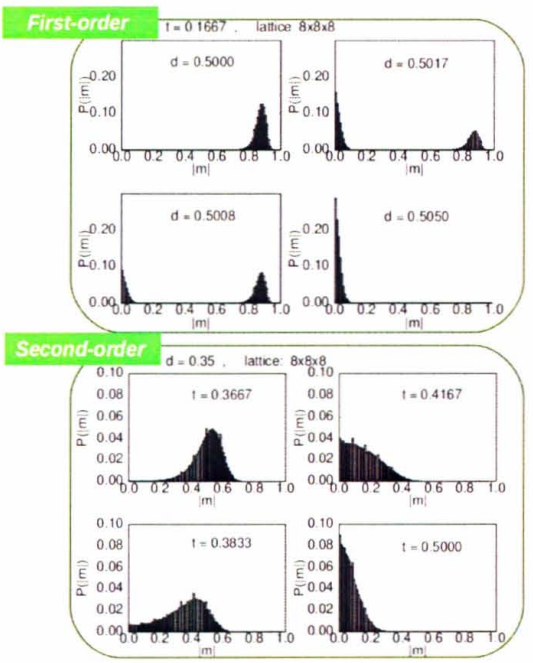

Figure 1.20: Histograms of the magnetisation illustrating first and second -order phase transitions.

[S. Tsai, *Brazilian Journal of Physics* **28**, 58 (1998)]

in the first-order phase transition the calculated distribution in the absolute value of magnetization splits up in two separated regions. In a second-order phase transition, there is a single continuous distribution. The same behavior is also observed in the energy of the system. The existence of two peaks in the histogram of magnetization (or energy) of a system around the critical temperature is a sign of the coexistence of two phases

(with different energy and magnetization). This phenomenon is seen in first-order phase transitions. On the other hand, in second order phase transitions, one phase switches to another phase smoothly through broadening the histogram of magnetization (or energy), and no sign of the coexistence phases is seen in the histogram of magnetization (or energy).

In a first-order phase transition, the following expression can represent the partition function of the system [27]:

$$Z(\beta, L) = q \exp^{(-\beta\ f_1(\beta)\ L^d)} + \exp^{(-\beta\ f_2(\beta)\ L^d)} \tag{1.37}$$

where L is lattice size, d is dimension of system, f_1 is the free energy of the ordered states, f_2 is the free energy of disordered states, and q is the relative weight coefficient. Eq. 1.37 shows the separation in the energy values around critical temperature. In Eq. 1.37, when $f_1 = f_2$ and $L \to \infty$, the partition function presents only one phase. For temperatures which are close to the critical temperature a Taylor expansion gives the following:

$$\beta f_i(\beta) = \beta_c\ f_i(\beta_c) - \beta_c e_i t - \frac{1}{2} C_i t^2 + O(t^3) \tag{1.38}$$

Where $t = 1 - \frac{T_c}{T} << 1$ is the reduced temperature, $e_i = \frac{(\partial \beta f_i)}{\partial \beta}|_{\beta_c}$ is the energy of i^{th} bulk phase, and $C_i = -\beta_c^2\ (\frac{\partial^2 \beta f_i}{\partial \beta^2})|_{\beta_c}$ is the specific heat of the i^{th} bulk phase. Eq. 1.37, with Eq. 1.38, can be rewritten as follows:

$$Z = q \exp^{(x + \frac{1}{2}ax^2)} + \exp^{(rx + \frac{1}{2}ayx^2)} \tag{1.39}$$

where $x = \beta_c e_1 t L^d$, $a = C_1/\beta_c^2 e_1^2 L^2$, $r = e_2/e_1 < 1$, and $y = C_2/C_1$. The partition function defined in Eq. 1.39 can be used to calculate $\langle E^1 \rangle_L$ and $\langle E^2 \rangle_L$ and define Binder's fourth cumulant, $V_4(L)$, as follows:

$$V_4(L) = 1 - \frac{\langle E^1 \rangle_L}{3 \langle E^2 \rangle_L^2} \tag{1.40}$$

Binder's fourth cumulant can be used to distinguish between first-order and second-order phase transitions. In first-order phase transition, when $T \neq T_c$ and in thermodynamic limits, this function converges to $\frac{2}{3}$, but at the critical temperature it shows a minimum,

and these minimums have a linear relationship with L^{-d}(see Fig. 1.21).

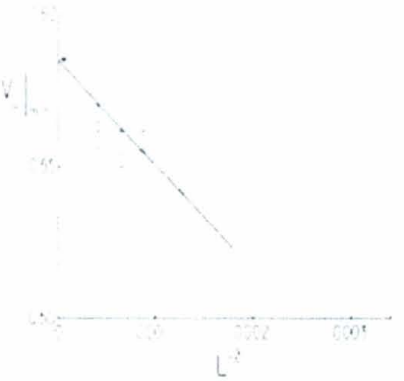

Figure 1.21: Example of Binder's fourth cumulant
[M.S.S. Challa, D. P. Landau and K. Binder, *Phys. Rev. B* **34**, 1841 (1986)]

1.8 Periodic Boundary Conditions

To eliminate surface effects, periodic boundary condition (PBC) are implemented. In this method, the entire space is covered by repeating the finite system (see Fig. B). In simulating a crystal structure, it is logical to assume that the system is repeated in space; however, the system size must be much larger than the correlation length in the system to see the periodic behavior. The PBC is also used in other fields of computational physics which involve less periodicity such as molecular dynamics of liquids. Nevertheless, the PBC shows little effect on the thermodynamic property of system with a short-range interaction in such systems [29]. Also using PBC gives the opportunity to simulate the system with less spatial symmetry such as thin-films. In this case, the system is only repeated in two dimensions (for example x and y), and the third dimension (z) is limited with the surface of system.

1.9 Outline of Thesis

Despite the technological significance of the binary alloy $Ir_{1-x}Mn_{3+x}$, surprisingly little theoretical or experimental work has been done to study the magnetic properties of

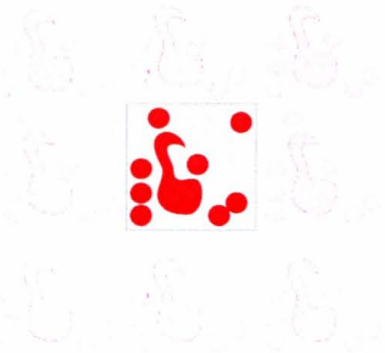

Figure 1.22: Periodic Boundary Condition

$Ir_{1-x}Mn_{3+x}$. In this work, we present one of the most complete simulation studies to date of the magnetic properties of bulk $Ir_{1-x}Mn_{3+x}$. The simulation studies focus on the fact that the magnetic lattice composed of the Mn atoms form a stacked 2D Kagome lattices, which we refer to as the fcc Kagome lattice. While stacked Kagome lattice has been studied extensively both theoretically and by simulations, little work has been done on the fcc Kagome lattice. The results of this work suggest that the degeneracy inherent in the stacked Kagome lattice may play an important role in the exchange pinning mechanism observed in $Ir_{1-x}Mn_{3+x}$.

The remainder of the thesis is organized as follows. In Chapter 2, the properties of $IrMn_3$ are discussed. This describes the magnetic, electrical, and crystallographic structure of this material in bulk and as a thin film. Chapter 3 is dedicated to the Monte Carlo simulation results of the two-dimensional Kagome lattice. The simulation of triangular lattice is also performed in order to compare the thermal behavior of the magnetic properties of the two systems. In Chapter 4, the three-dimensional ABC-stacked Kagome lattice (fcc Kagome lattice) is studied and the results are compared with the corresponding quantities of the usual fcc structure. The type of phase transition is determined by using Binder's fourth cumulant. Finally, in chapter 5, the main results are summarized as are the conclusion of this thesis, and also some suggestions are offered for future work.

Chapter 2

Properties and Models of $IrMn_3$

$Mn_{(1-x)}Ir_{(x)}$ alloys are of interest to many research groups. The bi-layer consisting of AF $Mn_{(1-x_1)}Ir_{(x_1)}$ and FM $Co_{(1-x_2)}Fe_{(x_2)}$ is widely used in the manufacture of spin-valves [30]. Mn-Ir alloys are widely used as the AF pinning layer in magneto-resistance junctions for two important reasons. First, the magnitude of exchange pinning field produced in the bi-layer made of a FM layer and this AF layer is appreciable. Second, this AF structure, as a magnetic system, is quite stable over a wide temperature range.

The magnitude of the exchange pinning field, H_{EB}, depends on the thickness of the FM layer, t_{FM}. It may be expressed as [31]:

$$H_{EB} = \frac{\Delta\sigma}{M_{FM}\, t_{FM}} \tag{2.1}$$

where $\Delta\sigma$ is the inter-facial unidirectional energy density, and this quantity is determined by the properties of the AF pinning layer. A recent measurement of $\Delta\sigma$ for the above-mentioned alloy shows a value close to 0.19 erg/cm^2. This amount is decreased by different annealing process to 0.16 erg/cm^2 [32]. The experimental results also show that the Néel temperature of this alloy increases from 600 K to 750 K, when the concentration of Mn increases from 10% to 30% [33]. The higher Néel temperature indicates the more stable AF magnetic order in the structure. In this chapter, some literature on Ir−Mn alloys are reviewed to establish a general picture of the relevant physics.

According to Szunyogh et al. [34], the magnetic anisotropy (MA) of the AF alloy plays a substantial role in the exchange pinning phenomenon. The MA can be used to predict the mean blocking temperature, T_B. The mean blocking temperature is the temperature

at which the sign of the exchange pinning field changes through thermal activation. Recent studies indicate a quite different amount for the MA in Ir−Mn depending on the quality of the crystal ordering in the thin films. For example, in research performed in 2007, the MA is reported to be 5.5×10^{6} erg/cc, while a value of 3.3×10^{7} erg/cc is reported by another group [35, 36]. Higher degrees of crystallographic order give larger MA. Despite experimental interest, the MA of Mn-based alloys has rarely been investigated theoretically. Szunyogh and colleagues have performed self-consistent calculation of the fully relativistic screened Korringa-Khon-Rostoker (SKKR) method. The SKKR method is used to solve the Kohn-Sham-Dirac equation for the alloy structure. As a first step, the fixed orientations for Mn atoms have been considered based on the results of previous research [37, 38], and the results were in agreement with the earlier calculations [37, 39]. In the next step, the following Hamiltonian is used to investigate the effect of symmetry in the energy per cell.

$$H = -\frac{1}{2}\sum_{a,b=1}^{n} J_{ab}\vec{S}_a\vec{S}_b - \frac{1}{2}\sum_{a,b=1}^{n} \vec{S}_a\mathbf{D_{ab}}\vec{S}_b - \sum_{a=1}^{n} \vec{S}_a\mathbf{K_a}\vec{S}_a \tag{2.2}$$

The Hamiltonian 2.2 includes two MA terms. The second term gives the anisotropic two-site (exchange) coupling. In this term, $\mathbf{D}_{ab}$ are symmetric and traceless matrices, Eq. 2.3. The third term is one-site anisotropy. In this term, $\mathbf{K}_a$ are also considered matrices as shown in Eq. 2.4 below

$$\mathbf{D_{ab}} = D_{ab}\begin{pmatrix} -\frac{1}{2} & 0 & 0 \\ 0 & -\frac{1}{2} & 0 \\ 0 & 0 & 1 \end{pmatrix} \tag{2.3}$$

$$\mathbf{K_a} = K\begin{pmatrix} 0 & 0 & 0 \\ 0 & 0 & 0 \\ 0 & 0 & 1 \end{pmatrix} \tag{2.4}$$

The rotations of the AF configuration are simply considered in the Hamiltonian 2.2 by selecting the appropriate coefficients, D_{ab}. For example; when D_{11} =D_{22} =D and D_{12} = D'

are taken, it means the AF configuration rotates around(100) axis. The symmetry of system, which affects the MA, is investigated by calculating energy change, ΔE, upon changing the rotation angle, ϕ. Szunyogh and colleagues also analyse the results, which

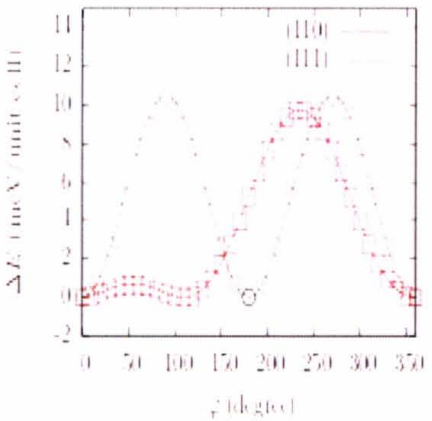

Figure 2.1: Energy Change vs Rotation Angle.
[L. Szunyogh,B. Lazarovits, L. Udvardi, J. Jackson and U. Nowak, *Phys. Rev. B* **79**, 020403 (2009)]

are plotted in Fig 2.1, to find the MA of the system. As can be seen, energy is degenerate for some specific angles. For example, for the rotation angle, $\phi = 109.47°$, around (110) axis, the calculated energy is the same as at $\phi = 0$. The single-site anisotropy is also calculated for each case. The results show a strong second-order MA in $IrMn_3$. While it may seem suprising given the cubic symmetry of $IrMn_3$, it is due to the fact that the cubic symmetry is broken by non-magnetic Ir atoms.

The authors go on to perform finite-temperature simulations based on the Landau-Lifshitz-Gilbert equations. For this, the following Hamiltonian is used;

$$H = -\frac{1}{2}\sum_{i \neq j} J_{ij}\ \vec{S}_i \vec{S}_j - \frac{K_{eff}}{2}\sum_i (\vec{S}_i \cdot \vec{n}_i)^2 \tag{2.5}$$

where J_{ij} are the isotropic Heisenberg exchange parameters. The second term in Hamiltonian 2.5 is the second-order anisotropy term. In the anisotropic term, $\vec{n}_i$ are the unit vectors along the local uniaxial axis. The relativistic torque method is used to calculate exchange interactions as function of the distance between magnetic sites [40, 41]. As can

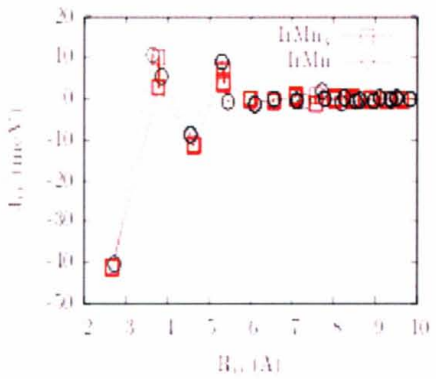

Figure 2.2: Isotropic Exchange Interaction vs Distance.
[L. Szunyogh,B. Lazarovits, L. Udvardi, J. Jackson and U. Nowak, *Phys. Rev. B* **79**, 020403 (2009)]

be seen in Fig. 2.2, the isotropic interaction is almost negligible beyond $6\dot{A}$; furthermore, the AF interaction of the nearest-neighbor is almost four times stronger than the FM interaction of the second nearest-neighbor in these structures. Only the nearest-neighbor interactions were used in our simulations. In the last part of this article, they calculate the sub-lattice staggered magnetization, M_s, as follows;

$$M_s = \frac{1}{n}\sum_{a=1}^{n}\left\langle\sqrt{M_{ax}^2 + M_{ay}^2 + M_{az}^2}\right\rangle \tag{2.6}$$

where $\vec{M}_a = \sum_{i\in a}\vec{S}_i$ is proportional to the magnetization of sub-lattice **a**, and n is the number of sub-lattices in the AF structure. As matter of fact, the sub-lattice staggered magnetization defines the order parameter of the system. The Fig. 2.3 illustrates the phase transition at 1360 K in the $IrMn_3$ alloy and 1005 K in the IrMn alloy. These *Néel* temperatures are also confirmed by experimental measurements. The most interesting result of this research is detecting a giant second-order MA for $IrMn_3$. This giant MA suggests the (111) direction as the uniaxial axis of this structure. The (111) direction in fcc lattice of $IrMn_3$ coincides with the z-axis of ABC-stacked triangular lattice (see Fig. 1.17).

Tomeno and his colleagues used magnetic neutron scattering (MNS) to investigate magnetic order $IrMn_3$ in 1999 [30]. In this project, for a wide range of temperatures

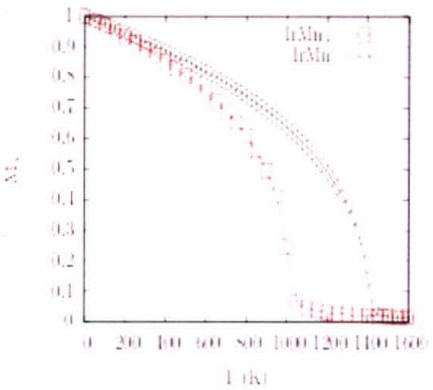

Figure 2.3: Sub-lattice Staggered Magnetization vs Temperature
[L. Szunyogh,B. Lazarovits, L. Udvardi, J. Jackson and U. Nowak, *Phys. Rev. B* **79**, 020403 (2009)]

the ordered magnetic moment and lattice parameter are measured from the (100) Bragg reflection. In the first stage of this research, single crystals were grown by the Bridgeman method. To avoid defects in the crystal structure, samples were annealed at 1000 K for three weeks, and then they were cooled to room temperature in a furnace. In the neutron scattering process, large absorption by Ir atoms is observed. Tomeno and his colleagues used the disk form of specimen to diminish the absorption effect. The neutron beams with wavelength of 2.437 $\dot{A}$ are used. The results show that the annealed samples have the Cu_3Au-type crystal structure which is the ABC-stacked Kagome structure.

Fig. 2.4, which includes four plots, illustrates the longitudinal scans taken by Tomeno and colleagues at room temperature. In this figure, the Gaussian fits (solid lines) are used to find the intensity peak positions. As can be seen in Fig. 2.4, the result around (100), plot (a), is quite similar to the result around (110), plot (c), and also, the result around (111), plot (b), is similar to the result around (200), plot (d). The broad Gaussian curves in plots (b) and (d) are interpreted as an indication of the many disorder phases which causes nuclear diffuse scattering around (200) and (111). From the experimental data in these plots, the ratio of reflection integrated intensities, are also evaluted; for example, the value of 9.2×10^{-3} is calculated for I_{111}/I_{100}. The squares of the nuclear structure

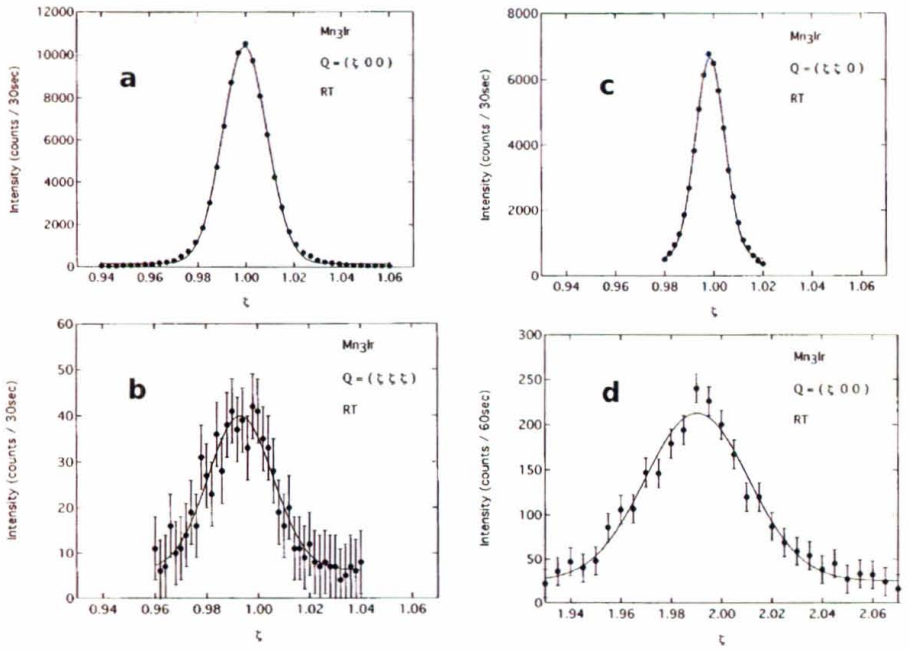

Figure 2.4: Longitudinal scanes around a.(100), b.(111), c.(110), and d.(200) Bragg Peak Positions.

[I. Tomeno, H. N. Fuke, H. Iwasaki, et al., *J. Appl. Phys.* **86**, 3853 (1999)]

factors are calculated as follows;

$$F^{\,2}_{100} = F^{\,2}_{110} = (\,b_{Ir} - \,b_{Mn})^2$$
$$F^{\,2}_{111} = F^{\,2}_{200} = (b_{Ir} + 3\,b_{Mn})^2 \tag{2.7}$$

where the $b_{Ir} = 10.6 \times 10^{-13}$cm and $b_{Mn} = -3.73 \times 10^{-13}$cm are the nuclear scattering lengths. The (111) reflection is the nuclear peak; while, the (100) Bragg reflection is the sum of nuclear and magnetic peaks. Thus the integrated intensity ratio, I_{111}/I_{100}, is expected to be less than F^2_{111}/F^2_{100}. Surprisingly, the calculated values, F^2_{111}/F^2_{100}=1.7×10^{-3}, is much less than the excepted value. Tomeno and colleagues explain this discrepancy by the presence of the disordered phase which causes the enhancement of the integrated intensity ratio, I_{111}/I_{100}, and the broadening of the (111) linewidth. Furthermore, they state that the (200) reflection occurs due to magnetic and nuclear scattering; the (111) reflection is caused only by nuclear scattering. The absence of magnetic scattering around the (111) suggests that the Mn magnetic moments are in the (111) plane. Fig. 2.5 shows the possible magnetic structure suggested by Tomeno and colleagues.

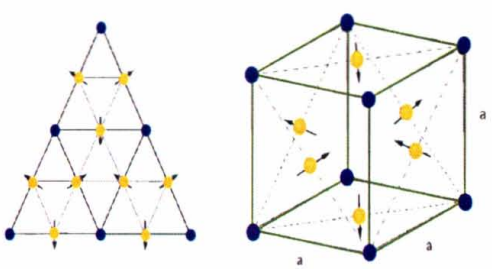

Figure 2.5: AF Structure of $IrMn_3$.
[I. Tomeno, H. N. Fuke, H. Iwasaki, et al., *J. Appl. Phys.* **86**, 3853 (1999)]

Tomeno and colleagues also measure the *Néel* temperature of the AF structure using MNS. As described, the disordered phase broadens the intensity of reflected neutrons beam; and consequently, it decreases the intensity of the peak. This is shown in Fig. 2.6.

As can be seen in Fig. 2.6, the maximum intensity decreases with inceasing temperature due to thermal fluctuations; therefore, the height of the peak in the integrated intensity

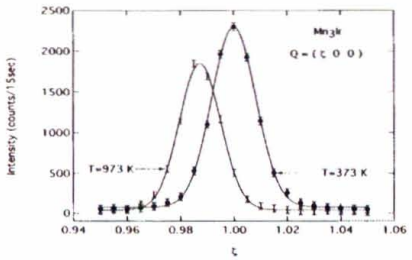

Figure 2.6: Decrement of intensity due to thermal disordered.
[I. Tomeno, H. N. Fuke, H. Iwasaki, et al., *J. Appl. Phys.* **86**, 3853 (1999)]

has a direct relationship with the order parameter of the system. This is used to determine the Néel temperature of the system by investigating the thermal behavior of the integrated intensity peaks around the (100). The (100) direction is selected due to existence of the strong magnetic scattering direction. The peak of the integrated intensity can be affected

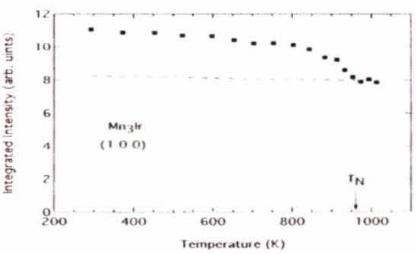

Figure 2.7: Temperature dependence of the integrated intensity.
[I. Tomeno, H. N. Fuke, H. Iwasaki, et al., *J. Appl. Phys.* **86**, 3853 (1999)]

by disorder in both the crystal structure and magnetic structure of the system. The nuclear-scattering part, shown with the dashed line in Fig. 2.7, can describe the disorder in crystal structure, while the squares illustrates the entire scattering. In the selected temperature range, crystal disorder, the dashed line, remains almost fixed; therefore, the entire change in the integrated intensity can be assumed as the result of the magnetic order. Based on this argument, Tomeno and his colleagues depict the magnetic scattering part, which represents the order parameter vs temperature.

As can be seen in Fig. 2.8, the results show the Néel temperature around 960±10 K. The lattice parameter is another quantity which is measured by Tomeno and colleagues.

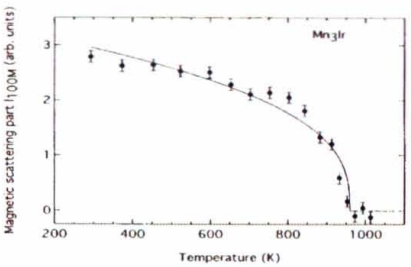

Figure 2.8: Temperature dependence of the magnetic part of scattering.
[I. Tomeno, H. N. Fuke, H. Iwasaki, et al., *J. Appl. Phys.* **86**, 3853 (1999)]

The measurements of the lattice parameter in $IrMn_3$ also shows that in the ordered phase, it is slightly smaller than in the disordered phase. Almost the same behavior has been reported for $PtMn_3$ [42].

The Magnetic structure of ordered and disordered Ir-Mn alloys has also been studied by Sakuma and colleagues [39]. Some experimental and theoretical research had previously been performed to investigate the magnetic and crystallographic properties of other Mn-based alloys. These indicate that the Néel temperature of the AF samples is substantially affected by the type and the concentration of the additional elements (such as Ru, Cu, Au, Pb, Fe, Ni, Ir, and Pt). Generally, the magnetic property of Mn-based alloys is described by the number of magnetic electrons and spatial distribution of $3d$ orbitals of Mn atoms in crystal structures [43]. Despite these efforts, the magnetic structures of Mn-based alloys are still not completely understood; furthermore, these alloys are widely used in many applications in industry. These facts motivated Sakuma and colleagues to perform the first-principle study of the magnetic of Mn-Ir alloys. The tight-binding (TB) linear muffin tin orbital (LMTO) method was used to study the electronic and the magnetic structure of disordered Ir_xMn_{100-x} and ordered $IrMn_3$ by Sakuma and his colleagues. Based on the TB-LMTO method [44], the effective exchange constant, J_0, is given by;

$$J_0 = -\frac{1}{4\pi}\int^{E_f} d\omega\ \mathbf{Tr}_{lm}\left\{\Omega_0(\omega)\left[g^{\gamma\uparrow\uparrow}_{00}(\omega) - g^{\gamma\downarrow\downarrow}_{00}(\omega)\right] + \Omega_0(\omega)\ g^{\gamma\uparrow\uparrow}_{00}(\omega)\ \ \Omega_0(\omega)\ g^{\gamma\downarrow\downarrow}_{00}(\omega)\right\} \tag{2.8}$$

where the $\Omega(\omega)$ is the potential function difference for an electron due to changing its spin, $\Omega_i(\omega) = p_i^{\uparrow}(\omega) - p_i^{\downarrow}(\omega)$, and $g^{\gamma}(\omega)$ is called the auxiliary green function (AGF). The AGF is composed of the potential function, $p^{\gamma}(\omega)$, and the screened structure constance, $\overline{S^{\gamma}}$, as $g^{\gamma}(\omega) = [p^{\gamma}(\omega) - \overline{S^{\gamma}}]^{-1}$. Eq. 2.8 is valid to describe the non-collinear magnetic structure of both ordered and disordered alloys. In the next step, the generalized molecular field theory is used to calculate the Néel temperature as follows [41];

$$T_N = \frac{2\ J_0}{3\ k_\beta} \tag{2.9}$$

Sakuma and colleagues in their article claim that two kinds of crystal structures for $IrMn_3$ alloy exist; $L1_2$-type (γ-phase) ordered (O) and γ-phase disordered (DO) alloy[15]. Fig. 2.9 shows the $L1_2$-type ordered $IrMn_3$. As can be seen in the figure, this structure consists of triangular (T1) in (111) plane as in Fig. 2.5. The same structure has been reported for $RhMn_3$ and $PtMn_3$ [46].

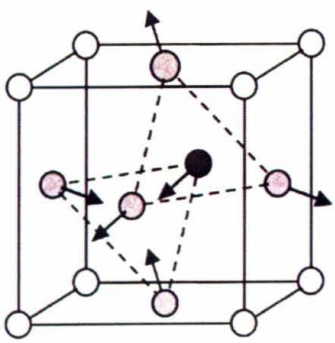

Figure 2.9: Triangular (T1) Magnetic Structure of $IrMn_3$. Open circles represent Ir atoms.
[A. Sakuma, K. Fukamichi, K. Sasao and R. Y. Umetsu, Phys. Rev. B **67**, 024420 (2003).]

Sakuma and colleagues have also studied the density of states (DOS) of these systems. The DOS curve of Ir atoms for electrons with spin up and down is completely symmetric with respect to energy axis. It means the number of the electrons with upward spin is equal with the number of the electrons with downward spin in Ir atoms. However, the

[15]The DO structures have been observed in the Ir_xMn_{100-x} alloys, when 14<x<31 [49].

DOS curve of Mn atoms show a significant spin polarization, this spin polarization gives a magnetic moment to the Mn atoms. The magnetic moment of Mn is calculated from the difference of DOS for spin up and down. The magnetic moments for the Mn and Ir atoms in the $L1_2$-type order $IrMn_3$ are 2.62 μ_B and zero, respectively.

They have also calculated the effective exchange constant, J_0, for the $L1_2$-type order $IrMn_3$ by using Eg. 2.8. The result shows the effective exchange constant is around 160meV . The Néel temperature calculated by substituting the J_0=160meV in Eq. 2.9 gives T_N=1250K. This is around thirty percent larger than the experimental value. The higher values have been reported for Mn alloys before this research. It seems the molecular field approximation gives the higher Néel temperature [47, 48].

The disordered alloys of $IrMn_3$ can form three possible magnetic structures which are illustrated in Fig. 2.10 [44]. The DOS of these three magnetic structures, named

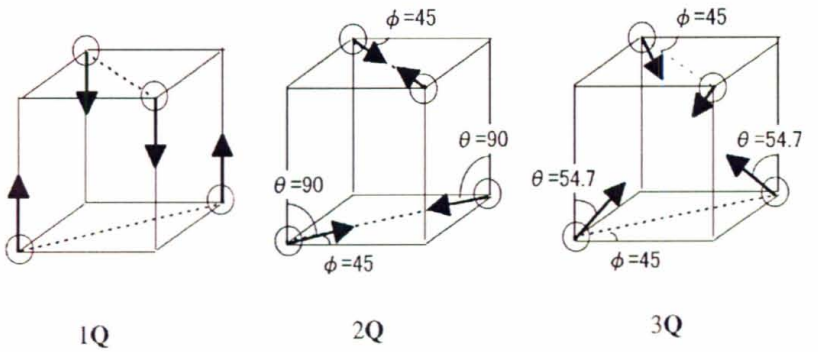

Figure 2.10: Magnetic Structures of Disordered $IrMn_3$.
[A. Sakuma, K. Fukamichi, K. Sasao and R. Y. Umetsu, Phys. Rev. B **67**, 024420 (2003).]

1Q, 2Q, and 3Q, have been calculated, the DOS curves in all configurations are quite similar to the order structure of T1. Such a phenomenon has not been reported in Mn alloys with Pt. The most similar disordered DOS to the DOS of the ordered structure of T1 is the 3Q structure; therefore, it is expected that the 3Q structure is the most stable disordered structure. The lowest energy has also been calculated for 3Q structure. Table 2.1 shows the calculated energy and the corresponding magnetic properties for

$IrMn_3$ alloys. The most surprising data in the table are the Néel temperatures given for 2Q and 3Q magnetic structures. Eq. 2.9 gives Néel temperatures of 648 K and 735 K for 2Q and 3Q magnetic structures according to calculated values for J_0, so there may be a misprint in the article. As can be seen in Table 2.1, the closest energy to the ordered configuration, 3Q, shows the energy differences around 5.6 mRy/atom. Also, as the discrepancy with the calculated Néel temperature of ordered structure, the calculated Néel temperature for 1Q magnetic structure is much less than experimental report. This may conflict with the the claim that the molecular field approximation may be the reason for higher calculated Néel temperatures. Sakuma and colleagues explain this discrepancy by considering the fact that difference between 1Q and 3Q magnetic structure is not clearly distinguishable by using the powder neutron diffractions method; therefore, the Néel temperature measured experimentally for 1Q structure could actually be the Néel temperature of 3Q structure [49]. According to this explanation, the calculated Néel temperature, T_N^{calc}=735 K, is close to and higher than the experimental Néel temperature, T_N^{expt}=730 K, of 3Q magnetic structure. The table also shows that in all disordered magnetic structures, Ir atoms have magnetic moments. This means that the symmetry of the DOS of Ir atoms breaks due to the binding with magnetic Mn atoms in disordered structures. This phenomenon is not observed in the ordered structure, T1.

Table 2.1: The Energy and Magnetic Results of $IrMn_3$ Alloys [39].

Phase	Mag. St.	ΔE	μ_{Mn}	μ_{Ir}	J_0	$T_N^{calc.}$	$T_N^{expt.}$
$L1_2$ type	T1	0.0	2.62	0.00	162	1253	960
DO	1Q	6.9	2.46	0.09	41	317	730
DO	2Q	6.0	2.47	0.11	85	66	
DO	3Q	5.6	2.51	0.12	95	0	

Sakuma and colleagues also discuss the effect of Ir concentration on the stable magnetic structures. The energy is calculated as a function of the angle θ to show which disordered magnetic structure is the most stable structure in different concentrations of

Ir (0, 5, 15, and 25% of Ir). As can be seen in Fig. 2.11 part (a), θ is defined as the angle between magnetic moments and z-direction. Based on this definition, θ=0°, 54.7° , and 90° correspond to 1Q, 2Q, and 3Q. As can be seen in Fig. 2.11 part (b), the energy curves

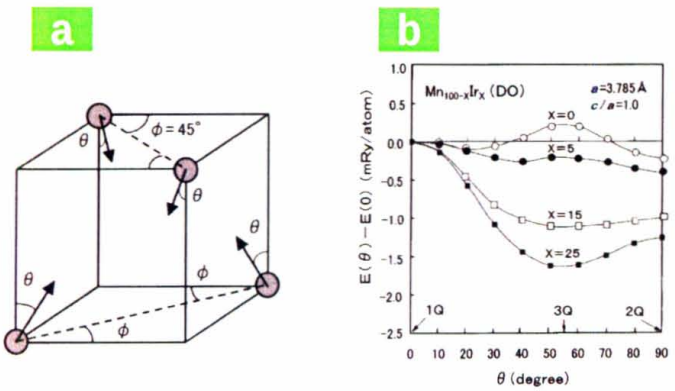

Figure 2.11: Energy of Disordered IrMn Alloys.
[A. Sakuma, K. Fukamichi, K. Sasao and R. Y. Umetsu, Phys. Rev. B **67**, 024420 (2003).]

show the minimum at θ = 54.7° when the Ir concentration is 15 and 25%. This angle presents 3Q structure as the most stable disordered structure. It is important to note that when x=25% the ordered structure, T1, is the most stable. Sakuma and colleagues have also investigated the phase diagram of two disordered structures, 2Q and 3Q, by increasing the concentration of Ir in alloys. Fig. 2.12 shows that the 2Q magnetic structure is the stable phase when the Ir concentration is less than $x_m \approx 13$ %. Above this critical concentration, x_m, the system prefers the 3Q magnetic structure. The assumption of an fcc structure for alloys with every concentration of Ir is not obvious. Therefore, Sakuma and colleagues have performed X-ray diffraction tests to investigate the effect of the concentration on the structure distortion. It seems that the face-centered tetragonal (fct) structure, with c/a>1, converts gradually into face-centered cubic (fcc), with c/a=1, by increasing temperature. The structural phase transition from the fct to fcc at the temperature $T_{fct/fcc}$ causes no anomaly on the magnetic behavior of the specimen. Sakuma and colleagues have investigated this assumption by measuring the magnetic susceptibility of

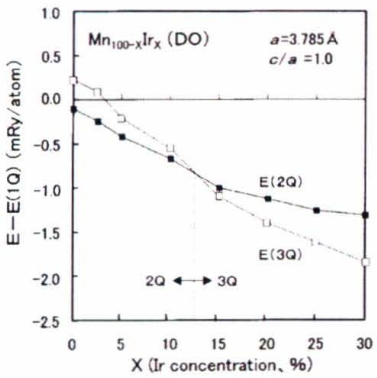

Figure 2.12: Energy of 2Q and 3Q magnetic structures.
[A. Sakuma, K. Fukamichi, K. Sasao and R. Y. Umetsu, Phys. Rev. B **67**, 024420 (2003)]

the $Ir_{15}Mn_{85}$ alloy in a field of 10 kOe, and there is no sign of unusual magnetic behavior at the temperature of $T_{fct/fcc}$.

The majority of research on Ir_xMn_{100-x} focuses on the pinning role of these AF alloys in the AF/FM bi-layers. The effect of AF thickness on exchange pinning has been studied by Ali and colleagues [50]. This work consists of experimental and MC simulation parts. For simplicity in the simulations, they have used the simple cubic (sc) lattice instead of the true fcc Kagome lattice. The observed results in the experimental part of the research are restudied by using simulation. The simulation results show significant compatibility with the experimental measurements. As can be seen in Fig. 2.13, the exchange pinning fields, H_{ex}, and coercivity, H_c, (see appendix 1) as function of the AF thickness are depicted at different temperatures. The same behavior have been observed in experimental and simulation data. These compatible results confirm the validity of the Hamiltonian which is used in simulation code, given by;

$$\begin{aligned} H = & -J_F \textstyle\sum_{<i,j>} \vec{S}_i \cdot \vec{S}_j - \sum_i (d_z S_{iz}^2 + d_x S_{ix}^2 + \vec{S}_i \cdot \vec{B}) \\ & - J_{AF} \textstyle\sum_{<i,j>} \epsilon_i \epsilon_j \vec{\sigma}_i \cdot \vec{\sigma}_j - \sum_i \epsilon_i (k_z \sigma_{iz}^2 + \vec{\sigma}_i \cdot \vec{B}) \\ & - J_{INT} \textstyle\sum_{<i,j>} \epsilon_j \vec{S}_i \cdot \vec{\sigma}_j \end{aligned} \tag{2.10}$$

In Eq. 2.10 the spins of FM and AF layer are denoted by $\vec{S}$ and $\vec{\sigma}$, respectively. The

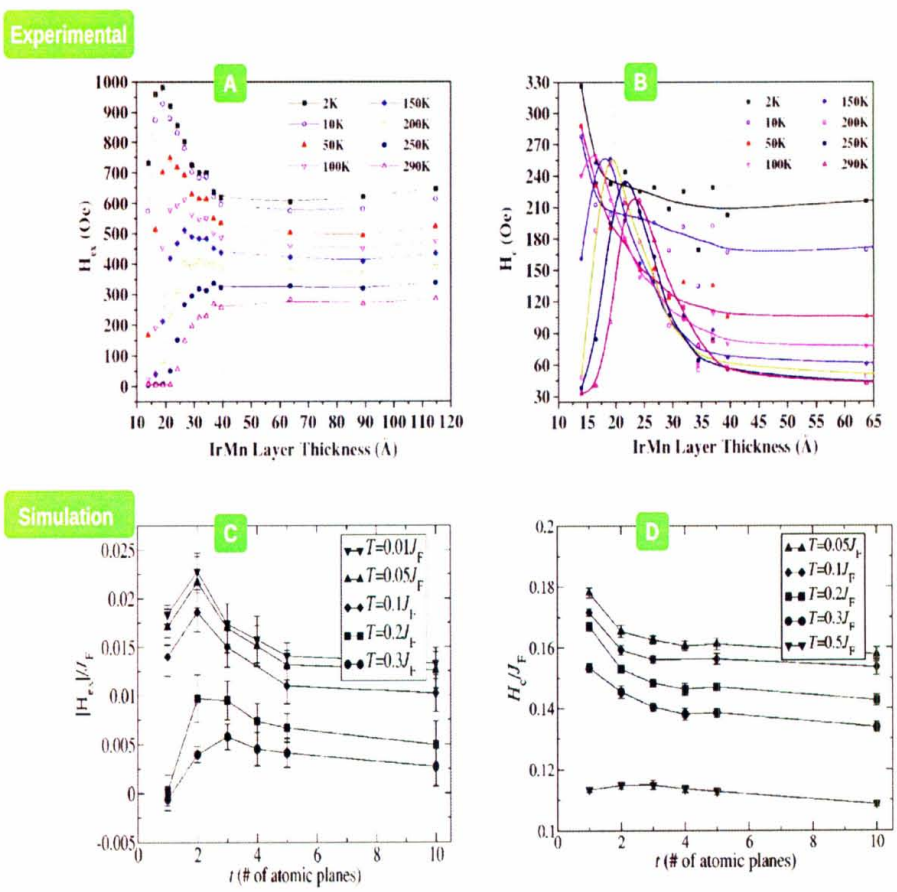

Figure 2.13: Exchange Pinning Field H_{ex} and Coercivity H_c in $IrMn_3$ from experiment and simulation.

[M. ALi, C. H. Marrows, M. Al. Jawad, B. J. Hickey, A. Misra, U. Nowak and K. D. Usadel, *Phys. Rev. B* **68**, 214420 (2003)]

external magnetic field, $\vec{B}$, is along the z-axis, while the x-axis is normal to the layers. In the simulations, the z-axis has been considered as an easy axis of the magnetic system by selecting $d_z > 0$, and the x-axis as the hard axis of FM layer, $d_x < 0$. Defining the x-direction as the hard axis causes the FM spins to remain in the yz-plane.

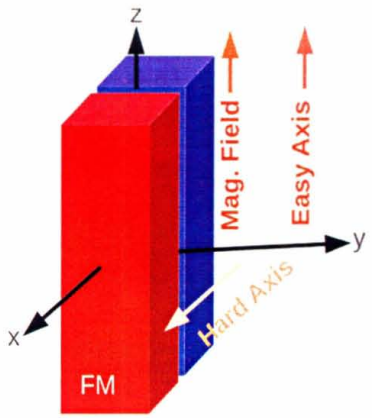

Figure 2.14: Orientations and Geometry of Exchange Pinning System used by Ali et al.

Based on the article by Ali and colleagues the geometry and orientations of the simulated system are schematically shown in Fig 2.14. Another important parameter in this Hamiltonian is the quenched disorder parameter, ϵ. This parameter can have one of only two values, ($\epsilon = 0, 1$). It seems that by selecting zero as the value for this parameter, a vacancy in AF is introduced in the simulation. This could be interpreted as causing roughness in the AF layer as the Malozemoff model (See chapter 1). Three different exchange interactions exist in this Hamiltonian; FM-FM, FM-AF, and AF-AF interaction. The strength of these interactions is defined by the magnitude of J_F, J_{AF}, and J_{INT}. Ali and colleagues have chosen $J_F = -2 \times J_{AF} = 2 \times J_{INT}$ in the simulation. Temperature plays a crucial role in the simulation of exchange pinning systems. As described in chapter 1, the exchange pinning occurs below the Néel temperature. Ali and colleagues have initialized the system at a temperature, T_1, below the Curie temperature, T_C, of the FM layer and above the Néel temperature, T_N, of the AF layer ($T_N < T_1 < T_C$), then through a cooling process [in the absence of any external magnetic field], the tempera-

ture of system is reduced to T_2, below the Néel temperature ($T_2 < T_N < T_C$). Then the external magnetic field has been applied while the temperature of system was kept fixed at T_2, and an MH loop for the FM layer calculated. The hysteresis loop of the system (see appendix 1), the curve of the magnetization vs external magnetic field, indicates the the exchange pinning field, H_{ex}, and the coercivity, H_c, of the systems with the different AF thicknesses. According to the results shown in Fig. 2.13, Ali and colleagues conclude that the exchange pinning field at low temperatures shows a sharp peak for a very thin AF layers and by increasing the thickness of the AF layers, the exchange pinning field decreases until it levels off. This phenomenon seems to be a fundamental property of exchange pinning; therefore, this research suggests that any significant theory of exchange pinning must be capable to explain this interesting functionality of the pinning field on the thickness of the AF layer. On the other hand, they show that the in-plane domains, as predicted in Malozemoff model, play a crucial role in the exchange pinning, especially in very thin layers.

To explain the exchange pinning in bi-layers, knowledge of the interface anisotropy and exchange interactions are crucial. The surface anisotropy plays an essential role in widely-used Malozemoff model. On the other hand, exchange interaction strengths show the influence of the number and ordering of neighbors of the energy of system.

In another research by Szunyogh and colleagues the form and strength of the anisotropy in $IrMn_3$/Co(111) interface has been studied [51]. In this work, the ordered bulk phase ($L1_2$) for $IrMn_3$ and fcc phase for Co were studied. The screened Korringa Kohn-Rostoker (SKKR) method was used to calculate the magnetic structure of the $IrMn_3$/Co(111) interface. It seems this research can be useful for future simulations to determine the magnetic interaction and anisotropy of the bilayer FM/AF with AF of Mn-Ir alloys.

Chapter 3

MC Simulations of the 2D Kagome and the 3D Triangular Stacked, and fcc Lattices

As a precursor to the simulation on the fcc Kagome lattice, we present MC simulation results on three lattices which are structurally close to the fcc Kagome. Results from these simulations are compared with previously published simulations. All computer codes are written in Fortran 90, and Perl is used to make links among the Fortran codes and also in post processing of the data. Most graphs are plotted using xmgrace and Mathematica7.

3.1 2D Kagome lattice

As discussed in the chapter 1, the Kagome lattice is constructed by removing one fourth of the lattice points of the triangular lattice. The interesting behavior of the 2D Kagome lattice at very low temperature (around absolute zero) has attracted the attention of many research groups. The 2D Kagome AF lattice was theoretically studied by Harris and colleagues in 1992 [52]. The essential results of this comprehensive work are used to evaluate the validity of the computer code written for this thesis which was eventually expanded to simulate the fcc Kagome lattice(3D).

In the 2D Kagome structure for XY and Heisenberg models with only the nearest neighbors AF exchange interactions, there is no single stable ground-state due to a high degree of degeneracy (see chapter 1). This theoretical prediction is confirmed by our Monte Carlo results. Results for the energy calculated for a 12×12 Kagome lattice are plotted as a function of temperature in Fig. 3.1. The data were averaged over 150,000

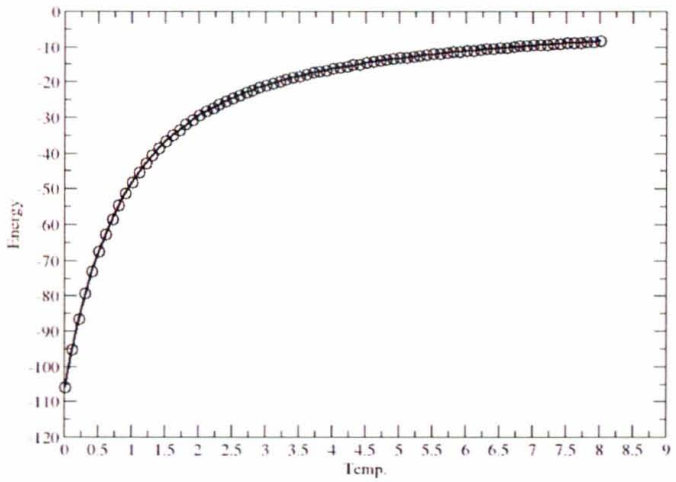

Figure 3.1: MC simulation results for energy vs temperature.
In the 2D Heisenberg Kagome lattice, no phase transition is observed.

MCS. The results show no indication of a discontinuity or sudden change in slope. As a consequence, the specific heat, C, plotted as a function of temperature in Fig. 3.2 does not show any local peaks or discontinuities, indicative of a first or second order phase transition. This is consistent with previous results [52]. It is impossible to define the order parameter for such a system due to the absence of the well defined ground-state configuration.

Zhitomirsky has shown that in using MC simulation to calculate the specific heat of the nearest-neighbor AF 2D Kagome lattice, just like our simulated system, particular care has to be taken at very low temperature, 10^{-4} <T<10^{-1}, as the acceptance rate decreases exponentially [53]. There are two strategies to tackle this problem; first, increasing the number of Monte Carlo steps in order to produce enough accepted 'moves', second, using a modified form of the algorithm. The first method is not very economic, and it may take a long time to produce enough accepted configurations based on random trials. An alternative approach, discussed by Zhitomirsky, is the *Metropolis rejection scheme* [53]. In this scheme, the acceptance rate is increased by imposing a new condition of $\Delta S^z \leq T$, (this formula can be the reduced form of $J \times \Delta S^z \leq k_\beta \times T$). This means that only the

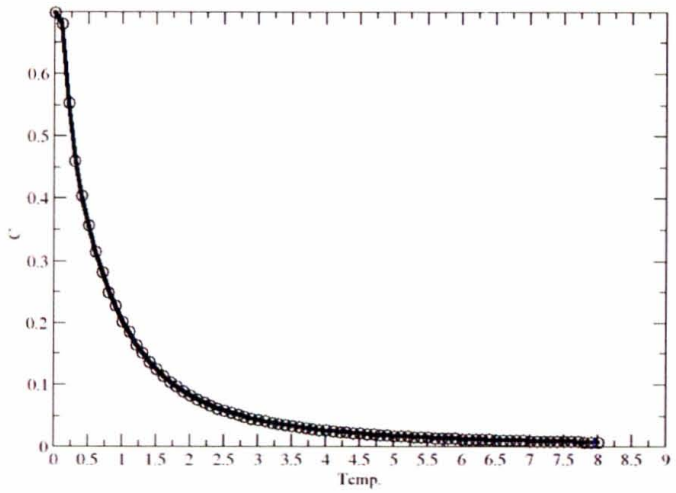

Figure 3.2: MC simulation results of specific heat vs temperature.
In 2D Heisenberg Kagome lattice, no phase transition is observed.

random changes in spin-configuration with the energy cost less than the thermal energy of system are taken as trial configurations. This method makes the code faster to produce accepted 'moves'. As can be seen in Fig. 3.3, the published results by Zhitomirsky (part

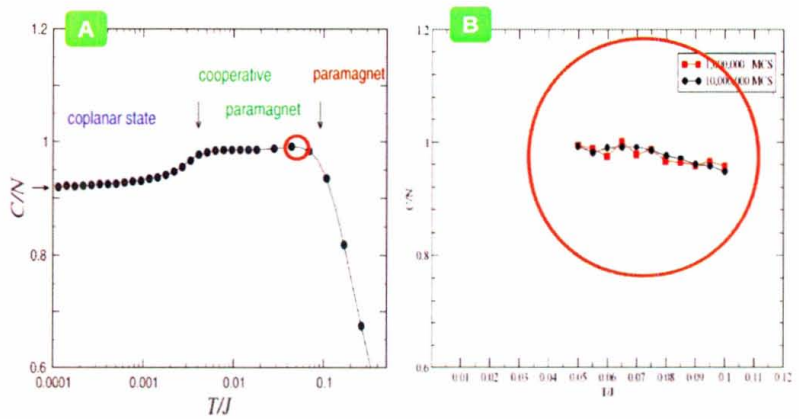

Figure 3.3: Specific heat vs temperature for 2D Heisenberg Kagome lattice at very low temperature.(A) from Ref. [53], and (B) from our Monte Carlo simulations.
[M. E. Zhitomirsky, *Phys. Rev. B* **78**, 094423 (2008)]

A) is confirmed by our results shown in the part B. The interesting fact is the number of MCS required to produce a smooth curve for the specific heat is around a million MCS. The need to use such a huge number of steps on the modified version of the MC code

shows how long the standard MC method takes to give results.

The possible ground-state configurations for the 2D Kagome lattice have been simulated including first, second, and third nearest neighbors exchange interactions. There are two usual schemes to determine ground-state of a lattice; the first scheme is by applying the standard Monte Carlo algorithm at very low temperature and then calculating the thermal average of spins. This scheme can take a long time and the final result is only an estimation of ground-state spin-configuration (the configuration does not show the exact configuration at absolute zero temperature). The second scheme is designed in a deterministic way. In this scheme the initial configuration is updated by imposing the AF constraint. The spin-orientation of each point is alinged anti-parallel to the magnetic field produced by the result of all its neighboring spins [45]. The simulation results for

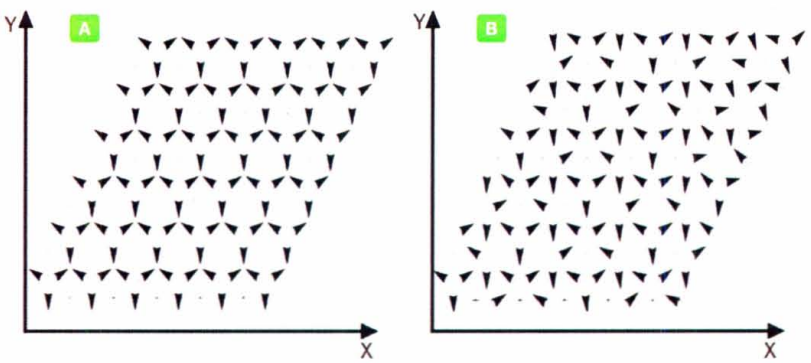

Figure 3.4: Ground-state 2D. (A) q=0, and (B) $\sqrt{3} \times \sqrt{3}$

the ground-states of the 2D XY Kagome (12×12) after 10^6 steps are shown in Fig. 3.4. As can be seen, there are two possible ground-states for the system defined to as the q=0 state(A) and the $\sqrt{3} \times \sqrt{3}$ state (B). Each of these configurations minimizes the energy of the system based on which pair of exchange interaction coefficients, J_2 and J_3, is selected for the following Hamiltonian;

$$H = -\frac{J_1}{2} \sum_{N.N} \vec{S}_i \cdot \vec{S}_j - \frac{J_2}{2} \sum_{S.N.N.} \vec{S}_i \cdot \vec{S}_j - \frac{J_3}{2} \sum_{T.N.N.} \vec{S}_i \cdot \vec{S}_j \tag{3.1}$$

As theoretically discussed by Harris and colleagues, the q=0 state is the ground-

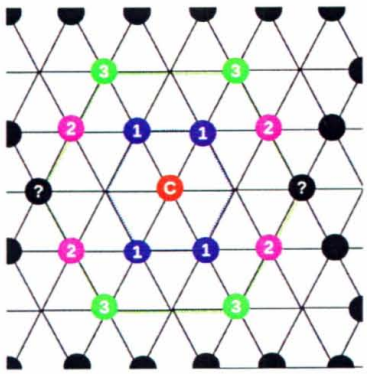

Figure 3.5: Nearest Neighbors (NN), Second Nearest Neighbors (SNN), and Third Nearest Neighbors (TNN) in the 2D Kagome lattice.

state of the system for $J_2 > J_3$ and $\sqrt{3} \times \sqrt{3}$ state is the ground-state for $J_2 < J_3$ [52]. To check our simulation code, the output ground-state configurations, shown in Fig 3.4, are used to calculate the energy of the system by changing the exchange coefficients, J_2 and J_3. Blue in Fig. 3.6 shows the area where the q=0 structure is the minimum

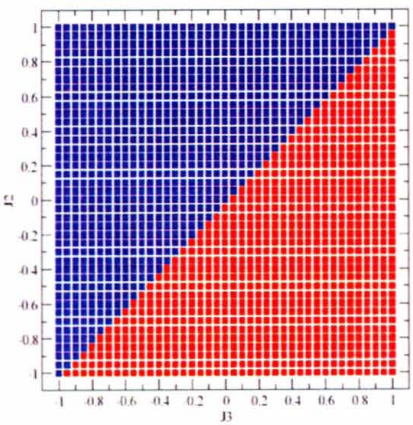

Figure 3.6: Stable area for q=0 (in blue) ,and $\sqrt{3} \times \sqrt{3}$ (in red)

energy state, while red is used to illustrate the area where the $\sqrt{3} \times \sqrt{3}$ structure is more stable. As can be seen, above the line y=x the stable structure is q=0 and below the line $\sqrt{3} \times \sqrt{3}$ structure possess lower energy, completely consistent with theoretical prediction. Harris and colleagues also have calculated the energy of the ground-states for both configurations. The following relationships between the ground-states energy, E_0,

and the exchange coefficients, J_1, J_2, and J_3, have been derived by minimizing the energy of system [52].

$$\begin{aligned} q = 0 \quad ; \quad & E_0 \propto -J_1 - J_2 + 2J_3 \\ \sqrt{3} \times \sqrt{3}; \quad & E_0 \propto -J_1 + 2J_2 - J_3 \end{aligned} \tag{3.2}$$

In the next stage of checking the simulation results, the functionality of energy with respect of exchange coefficients has been evaluated. The results of this evaluation is shown in Fig. 3.7. As can be seen, the energy has a linear relationship with the exchange

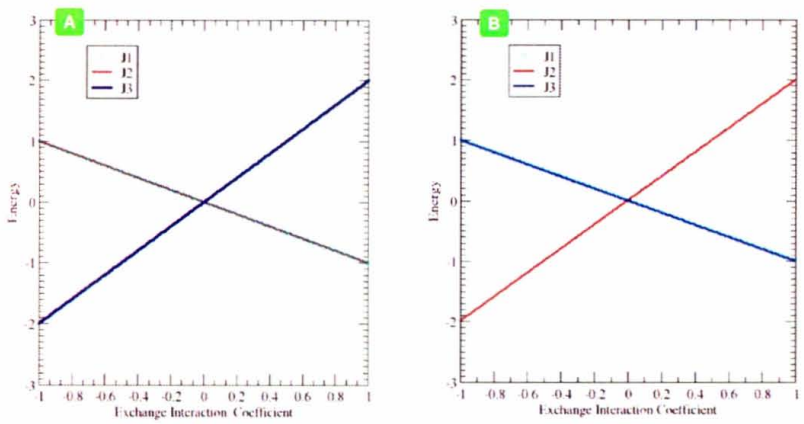

Figure 3.7: Energy as a function of exchange interaction coefficient

coefficients with the slopes that agree with the expressions (3.2). In part (A) of Fig. 3.7, the q=0 structure shows the exact -1, -1, and 2 as the slopes for energy lines vs J_1, J_2, and J_3, and in the part (B), the slopes for $\sqrt{3} \times \sqrt{3}$ are -1, 2, and -1, respectively.

3.2 Stacked Triangular Lattice

The AA-stacked triangular lattice is illustrated in Fig. 3.8. As can be seen, each lattice point has eight nearest neighbors in this structure (six in the plane and one above and one below). This crystallographic structure is seen in materials with ABX_3 chemical formula such as $CsNiF_3$ [54]. The Heisenberg model is used to simulate the stacked triangular lattice, and then the results are compared with the results published in 1990 by Mailhot and colleagues [13]. The Hamiltonian includes the exchange interaction between the

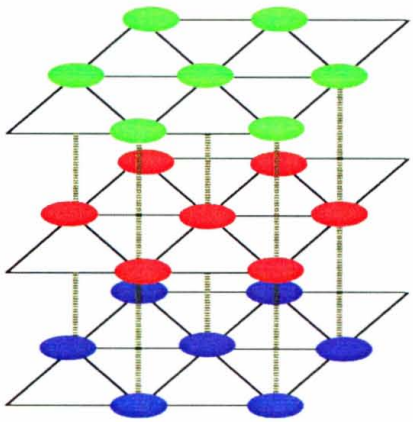

Figure 3.8: AA-Staked Triangular Lattice

nearest neighbors and uniaxial anisotropy as follows;

$$H = -\frac{J}{2} \sum_{<NN>} \vec{S}_i \cdot \vec{S}_j - \sum_i D S_{zi}^2 \tag{3.3}$$

For $J = -1$ (AF interaction) and $D = 1$ (z-axis as uniaxial easy axis), the results for the energy, E, and specific heat, C, are plotted in Fig.3.9 and Fig. 3.10, respectively. These results were obtained on a 12×12×12 lattice after 10^5 MCS.

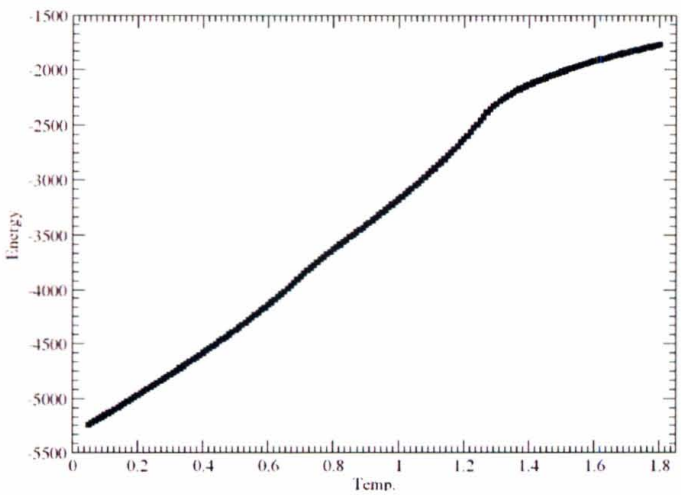

Figure 3.9: MC simulation results for energy vs temperature in the AA-stacked triangular lattice.

As can be seen in the Fig. 3.9, the curve shows sudden changes in the slope of the

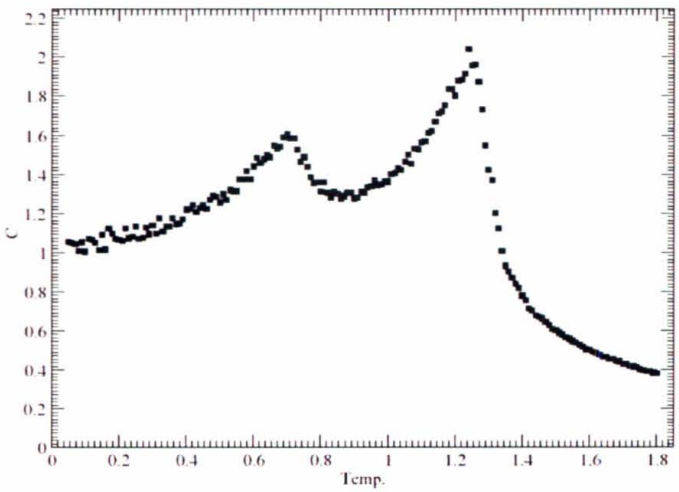

Figure 3.10: MC simulation results for specific heat vs temperature in AA-stacked triangular lattice.

energy at two temperatures (T=0.6 and T=1.2) indicating two possible phase transitions. The specific heat curve, in Fig. 3.10, also suggests the existence of two possible phase transitions in the stacked triangular lattice. These phases match with the critical temperatures reported by Mailhot and colleagues [13]. The interesting property is the existence of two critical temperatures. In Ref. [13], a scheme is used to understand the character of these two phase transitions through thermal behavior of various order parameters. The order parameters are defined separately for z-components and xy-components of spins as follows;

$$\begin{aligned} M_t &= (3/N)\left\{\langle M_A^2 + M_B^2 + M_C^2\rangle/3\right\}^{1/2} \\ M_z &= (3/N)\left\{\langle (M_A^z)^2 + (M_B^z)^2 + (M_C^z)^2\rangle/3\right\}^{1/2} \\ M_{xy} &= (3/N)\left\{\langle (M_A^x)^2 + (M_B^x)^2 + (M_C^x)^2 + (M_A^y)^2 + (M_B^y)^2 + (M_C^y)^2\rangle/3\right\}^{1/2} \end{aligned} \tag{3.4}$$

where N is the number of the sites and M_η^σ and M_η^2 are defined as follows;

$$\begin{aligned} M_\eta^\sigma &= \textstyle\sum_j (-1)^j \sum_i S_{i,j}^{\sigma,\eta} \\ M_\eta^2 &= (M_\eta^x)^2 + (M_\eta^y)^2 + (M_\eta^z)^2 \end{aligned} \tag{3.5}$$

with $\sigma \in \{x, y, z\}$ and η indicates the magnetic sub-lattices as mentioned in Sec. 1.4. There are three sub-lattices A, B, and C, in the triangular lattice. These sub-lattices are

shown in Fig.3.11. This scheme has been used to calculate order parameters and the

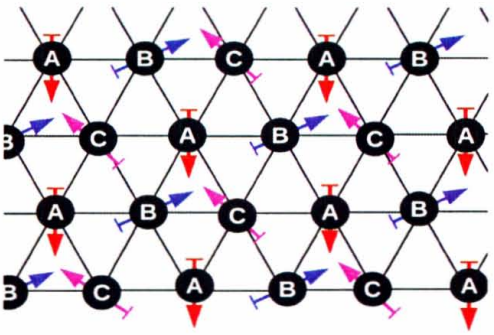

Figure 3.11: Magnetic sub-lattices in the triangular lattice.
(The 120° spin-structure)

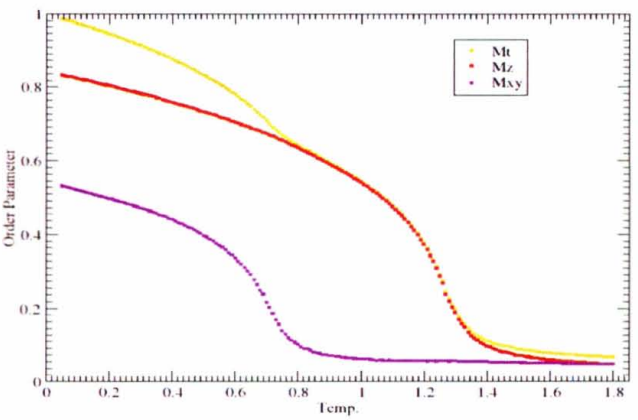

Figure 3.12: Order parameters in triangular lattice vs temperature from our MC simulations.

results are shown in Fig. 3.12. As can be seen, below the higher critical temperature, T_c=1.2, only z-components of spins start to be ordered and the xy-components take their ordered orientation below a lower critical temperature, $T_c = 0.6$. These results are confirmed by Ref. [13]. The same scheme is used later for the fcc Kagome lattice, as discussed in chapter 4.

3.3 Face-Centered Cubic (fcc)

The AF fcc lattice was also simulated in order to check the computer code. The fcc lattice can be viewed as an ABC-stacked triangular lattice along [111] directions. The only difference between fcc Kagome and regular fcc is vacancies of 25 percent of lattice points in the Kagome lattice. A previous study of a Heisenberg AF on fcc lattice has been preformed by Puma and colleagues [55]. Their results show a phase transition at $T_c \cong 0.4J/k_\beta$. As can be seen in Fig.3.13, the energy of our simulations also shows a discontinuity around T=0.445 which is close to the result obtained by Puma and colleagues. Also the discontinuity in the energy curve suggests the existence of a first order phase transition. In Fig. 3.14, the specific heat shows the critical temperature with a clear peak. This result has been produced for the lattice size of $18 \times 18 \times 18$ with MCS=2.0×10^5.

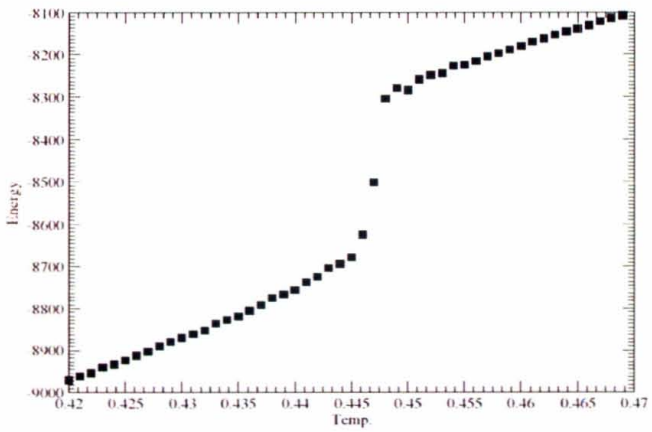

Figure 3.13: MC simulation results for the energy vs temperature in the Heisenberg fcc lattice.

3.4 Summary

The agreement between our results and previously published results on 2D Kagome lattice, A-A stacked triangular lattice and fcc lattice confirms the validity of our code in simulating the structures close to the fcc Kagome lattice. Also, the written subroutine based on the method described in Sec. 3.2 was confirmed in practice. This method is

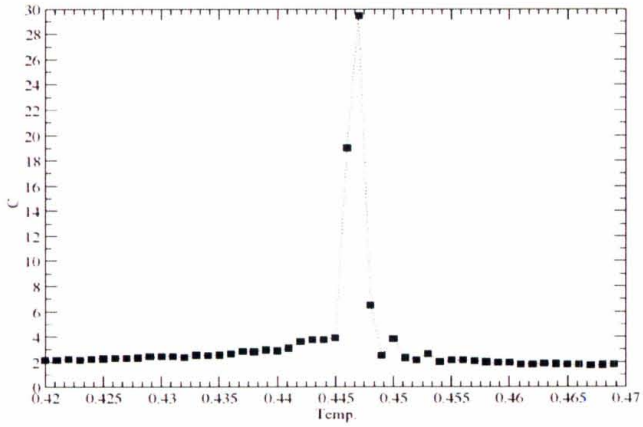

Figure 3.14: MC simulation results for the C vs temperature in the Heisenberg fcc lattice.

used to calculate order parameters in chapter 4. In the following chapter, we focus on the fcc Kagome lattice as a new structure. There are no published results available about MC simulation of the fcc Kagome lattice.

Chapter 4

MC Simulations of the FCC Kagome Lattice

4.1 Crystallographic and Magnetic Structure of the Fcc Kagome Lattice

In this chapter, simulation results of the AF Heisenberg and xy fcc Kagome (ABC-stacked Kagome) lattices are presented. The crystallographic structure of the fcc Kagome is illustrated in Fig. 4.1. As can be seen, this three dimensional structure consists of 2D Kagome layers which are shifted with respect to the adjacent layers. In ABC-stacked triangular lattice, each point in the lattice has 12 nearest neighbors; however, in the fcc Kagome, 4 of these positions of nearest neighbors are vacant. Therefore, each point has 8 nearest neighbors; 4 nearest neighbors in the plane and 2 on the upper layer and 2 on the lower layer.

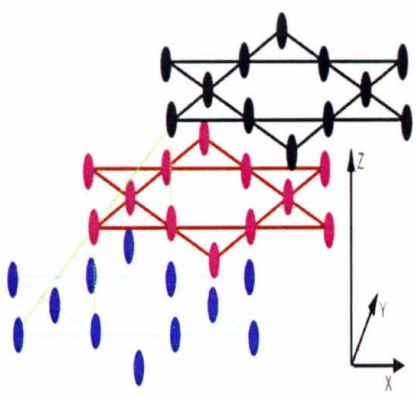

Figure 4.1: fcc Kagome structure. ABC planes shown are in the xy plane. <111> is along the z axis.

Based on previously published results on the 2D Kagome lattice (see chapter 2 and 3), the existence of three magnetic sub-lattices in the fcc Kagome is assumed to define the order parameter of the system, as will be described in this chapter, this assumption is confirmed numerically by the MC simulations. In Fig. 4.2, we show the ground-state spin-configuration for a single layer of the fcc Kagome lattice, with different sub-lattice shown in different colors (blue (sub-lattice A), red (Sub-lattice B), and black (sub-lattice C)). As can be seen, the spin-configuration of this ground-state corresponds to the q=0 state found in the 2D Kagome lattice. It is important to recall that the q=0 structure for the 2D Kagome lattice is achieved only when second and third nearest neighbors exchange interactions are included. Another important fact about the magnetic structure of the fcc Kagome lattice, which must be taken into account, is the possibility of the existence of degeneracy due to the location of the vacancies (see Sect. 1.6.1).

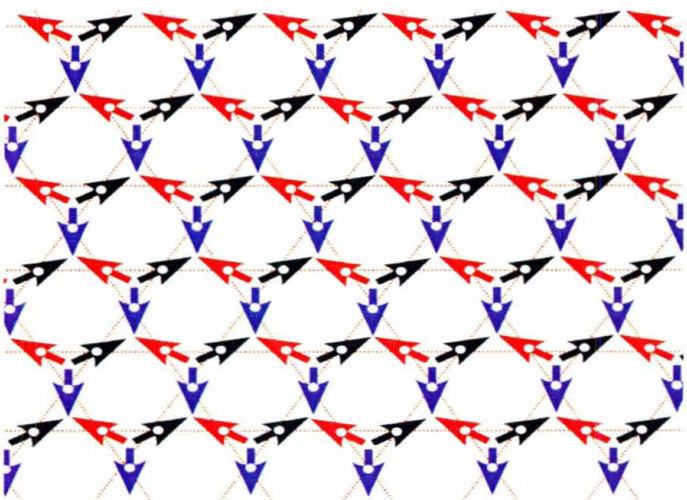

Figure 4.2: Magnetic sub-lattices of the fcc Kagome lattice.

4.2 Energy and Specific Heat of the Fcc Kagome Lattice

To investigate the magnetic structure of the fcc kagome lattice, three simulation processes, heating, cooling, and runs at independent temperatures, have been performed. In the heating processes, the q=0 structure was used as initial spin-configuration of the system

at the lowest temperature, and in a serial run of increasing temperature, the initial spin-configuration at next temperatures was the final spin-configuration of the previous lower temperature. In the cooling processes, a random spin-configuration was used as initial spin-configuration of the system at the highest temperature, and in a serial run of decreasing temperature, the initial spin-configuration at next temperatures was the final spin-configuration of the previous higher temperature. In the independent temperatures simulations, a random spin-configuration was used as initial spin-configuration at each temperature. Moreover, runs at different temperatures were completely independent and performed on different CPUs.

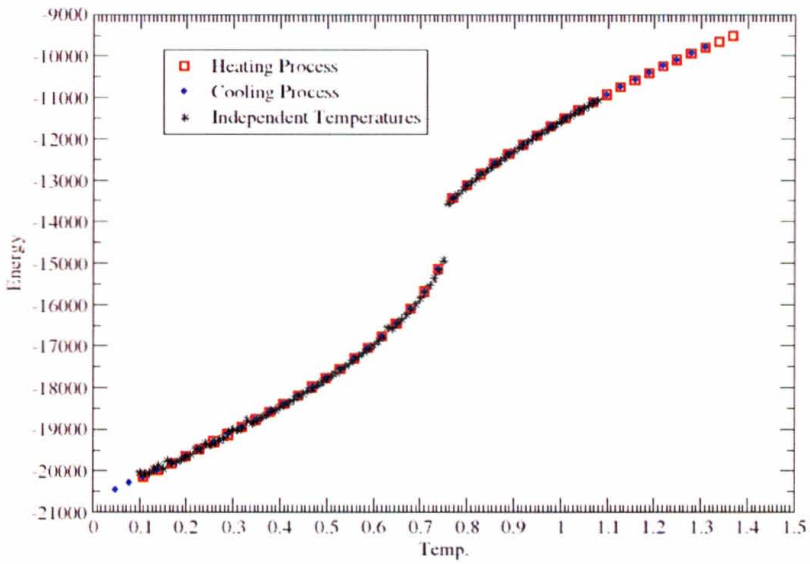

Figure 4.3: Simulation results of energy vs temperature for the xy fcc Kagome lattic.

Figs. 4.3 and 4.4 show the energy of the fcc Kagome system vs temperature for xy and Heisenberg models. These results have been achieved with a 24×24×24 lattice after 10^5 MCS in the heating and cooling processes and after 10^7 MCS in the independent temperatures simulation. As can be seen, the results of the heating, cooling, and independent temperatures processes completely agree. The energy of the system is a function of number of spins (lattice size), the interaction types (Hamiltonian), and the temperature of the system; moreover, the energy is independent of initialization of the system. Therefore,

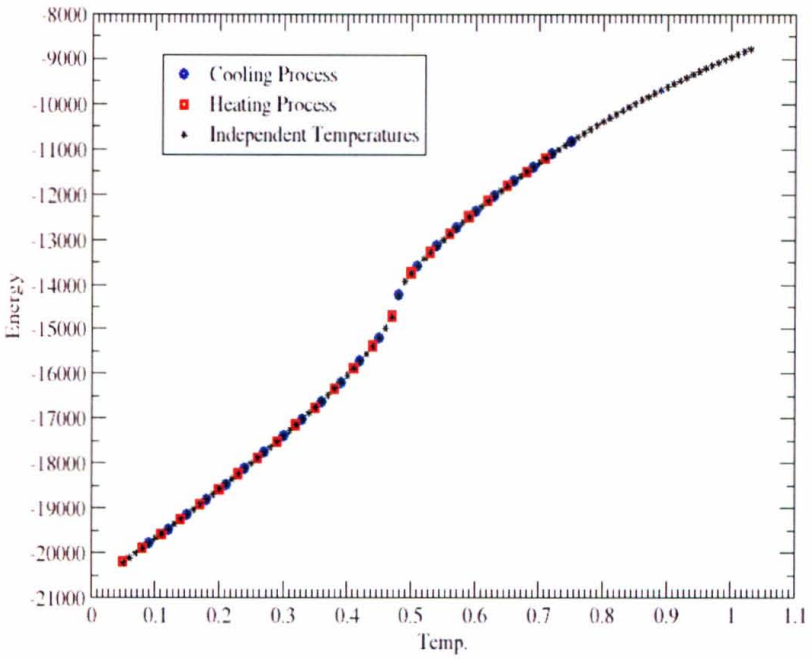

Figure 4.4: Simulation results of energy vs temperature for the Heisenberg fcc Kagome lattice.

for each model (Heisenberg or xy) the results are completely independent of the selected process (heating, cooling, or independent temperature). These two figures show possible phase transitions at T=0.76 and T=0.47 for xy and Heisenberg fcc Kagome, respectively. The obvious discontinuity in the curve of the xy fcc Kagome energy suggests a first order phase transition, while the discontinuity observed in the Heisenberg model shows only a possible weak first order phase transition at a lower temperature.

Figs. 4.5 and 4.6 show the specific heat, C, of the xy and Heisenberg fcc Kagome systems. As expected, the specific heat vs temperature is completely independent of initialization of system; therefore, the results of three different processes, heating, cooling, and independent temperature, overlap each other in both xy and Heisenberg cases. Also, the sharp peaks at T=0.76 and at T=0.47 for xy and Heisenberg models, respectively, confirm our observation of the discontinuity in energy of the system (see Figs. 4.3 and 4.4). Also as an addition check on the results obtained from our simulations, we note that the specific heat of the xy results converge to 0.5 at low temperature, while the

Heisenberg case, specific heat converges to 1.

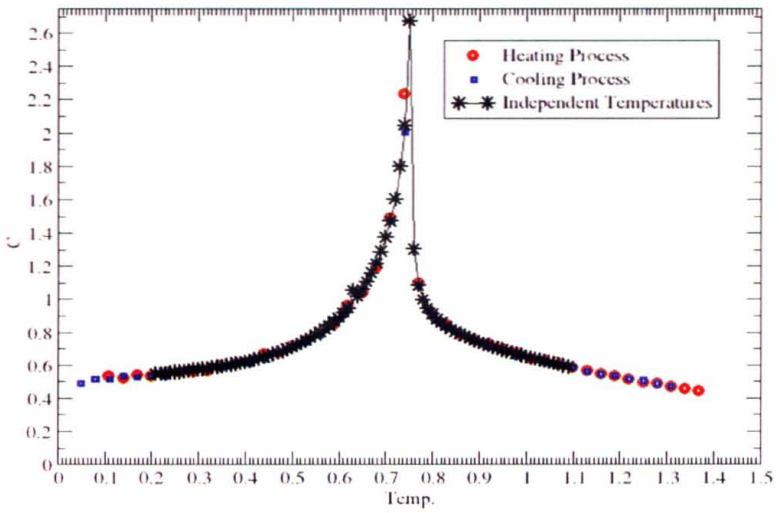

Figure 4.5: Simulation results of C vs temperature for the xy fcc Kagome lattice.

4.3 Kagome Inter-Layer Interactions

In the fcc Kagome lattice, each spin interacts with its eight nearest neighbors. Four of these nearest neighbors are in the plane and two of them located in the layer above and two in the layer below. It is of interest to study the effect of the inter-plane interactions on the specific heat. As discussed in chapter 3, no phase transition is observed in the 2D Kagome lattice when only nearest neighbors are in the exchange interaction. Based on this fact, decreasing the inter-layer interaction coefficient, J′, to zero must finally destroy long range order, because in the case of J′=0, the system consists of independent 2D Kagomes which have no phase transition. On the other hand, experiments show that the effect of changing J′ can explain the real system. As described in chapter 2, the fcc structure of $IrMn_3$ may show not a perfect cubic ($c/a \neq 1$) lattice, with the vertical lattice parameter, c, is slightly longer than in-plane lattice parameter, a [39].

In order to simulate the effect of changing J′ on the specific heat, we have used a Perl code to simulate the independent temperatures process using around 400 CPUs on ACEnet machines. Recall that the previous results of energy and specific heat shows the

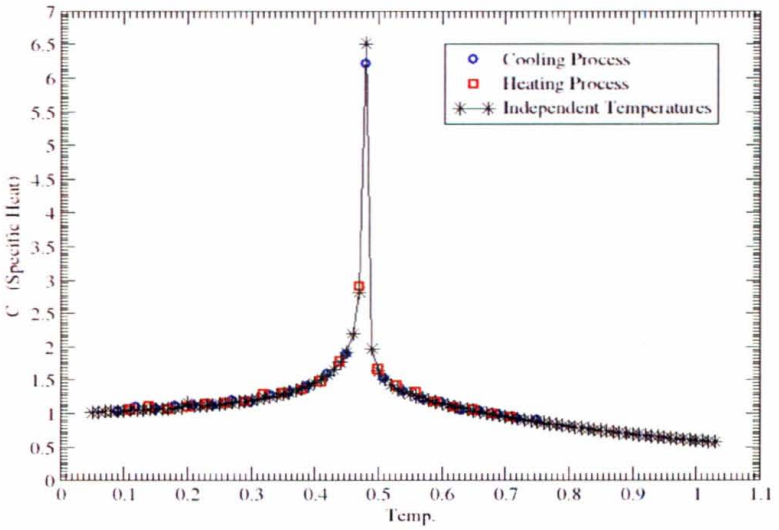

Figure 4.6: Simulation results of C vs temperature for the Heisenberg fcc Kagome lattice.

equivalence of the three different processes (see Figs. 4.3 to 4.6). Note that this part of simulation requires very long times in serial runs. The 3D Kagome lattice with the lattice size of 24×24×24 was simulated for xy and Heisenberg models by changing the inter-plane interaction, $0.05 \leq J' \leq 0.95$, with 10^7 MCS in the independent temperatures process. We set $J_1=1$.

As can be seen in Figs. 4.7, 4.8, and 4.9, decreasing the inter-layer exchange interaction coefficient, J′, reduces the temperature of the specific heat peaks values which approach zero temperature. When $J' \to 0$, this local peak in curve has completely disappeared. At low temperatures, much lower than the critical temperature, the temperature dependence of the specific heat exhibits large fluctuating due to low acceptance rate. To overcome this problem, significantly more MCS would be required. As a consequence the low temperature data are not included in Figs. 4.7, 4.8. All the curves for the xy model converge to 0.5 at zero temperature while the curves in the Heisenberg models converge into 1.0. Also, the results show that the specific heat in the xy model is almost two times more sensitive than Heisenberg model to the vatiation in J′. In order to compare

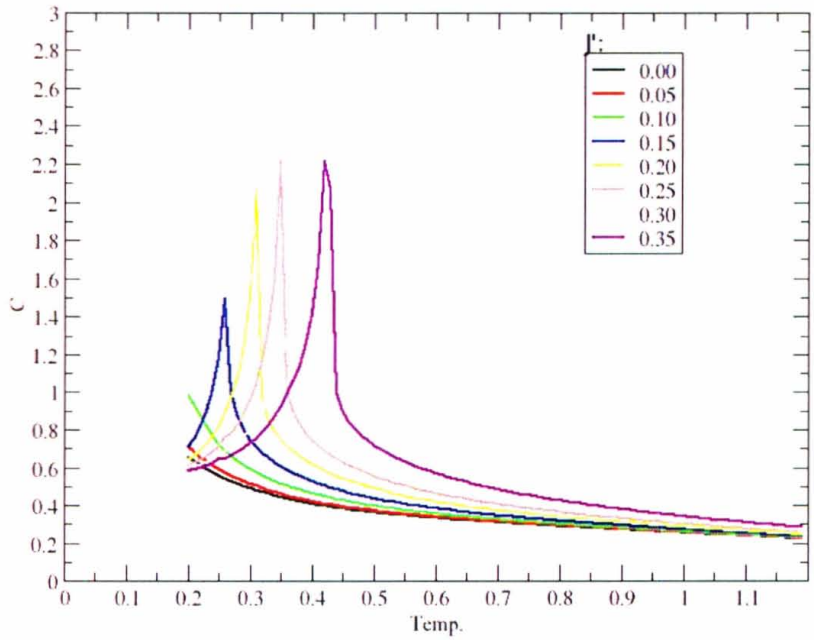

Figure 4.7: Simulation results of C vs temperature in xy 3D Kagome with different inter-layer exchange, J′.

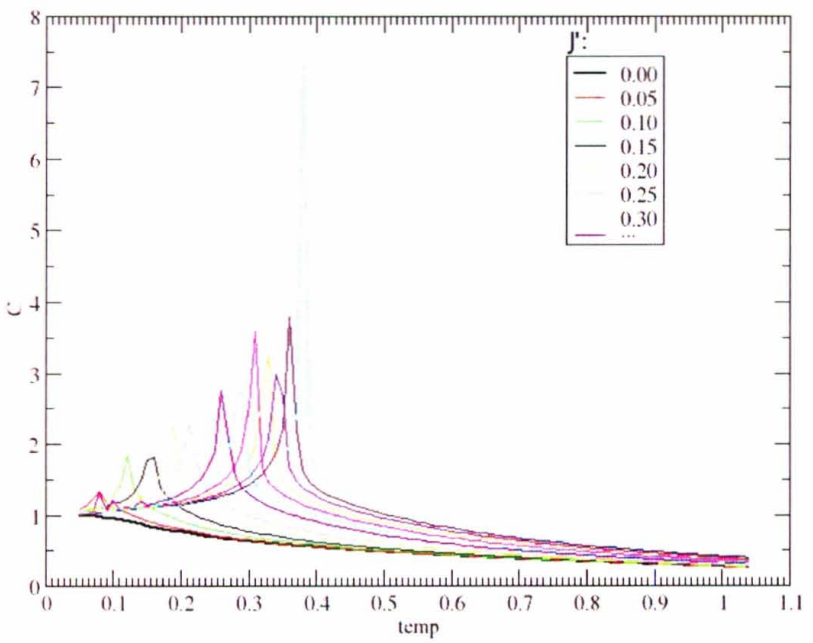

Figure 4.8: Simulation results of C vs temperature in Heisenberg 3D Kagome with different inter-layer exchange, J′.

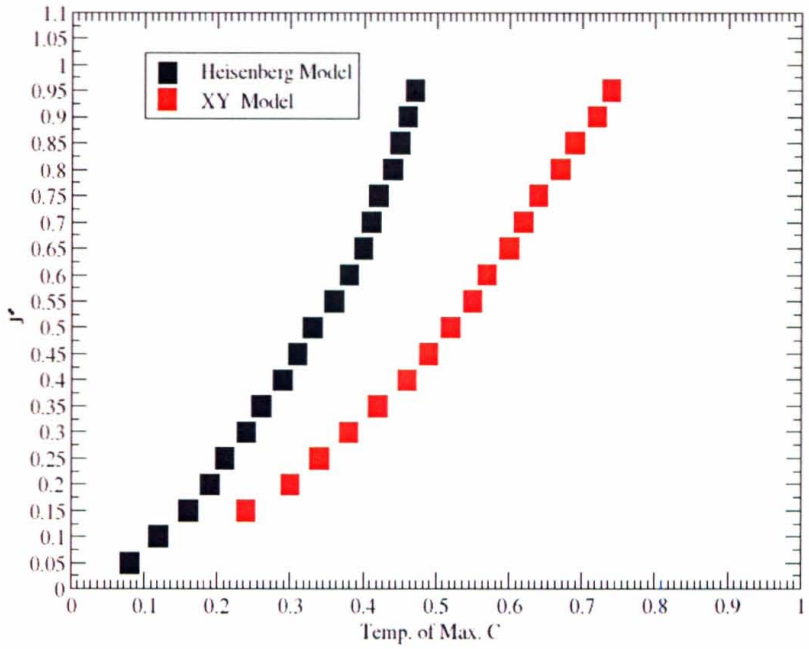

Figure 4.9: Simulation results of the position of C peaks for different J′.

sensitivity of specific heat, the relative variance of data shown in Fig. 4.9 is used.

$$\begin{aligned} \textbf{XY Model} \quad &: \quad \frac{\mathbf{Vr}(T_{peak})}{\mathbf{Vr}(\mathrm{J}'/J)} = 0.36 \\ \textbf{Heisenberg Model} &: \quad \frac{\mathbf{Vr}(T_{peak})}{\mathbf{Vr}(\mathrm{J}'/J)} = 0.19 \end{aligned} \tag{4.1}$$

where Vr(x) denotes the variance of x. This may mean that magnetic structure of Heisenberg model is more stable through a structural phase transition from fcc to fct where the inter-layer spacing changes.

4.4 Size Effects and the Order of the Phase Transition

To observe the effect of lattice sizes on the specific heat and critical temperature, simulations with different lattice sizes, from 12×12×12 to 36×36×36, have been performed through independent temperatures process and for 10^7 MCS. In principle, the critical temperature, T_c, must shift to the exact value when the lattice size goes to infinity. In

the infinite system, the peak of specific heat also has its maximum height and minimum width; therefore, the critical temperature can be determined more precisely with a bigger lattice.

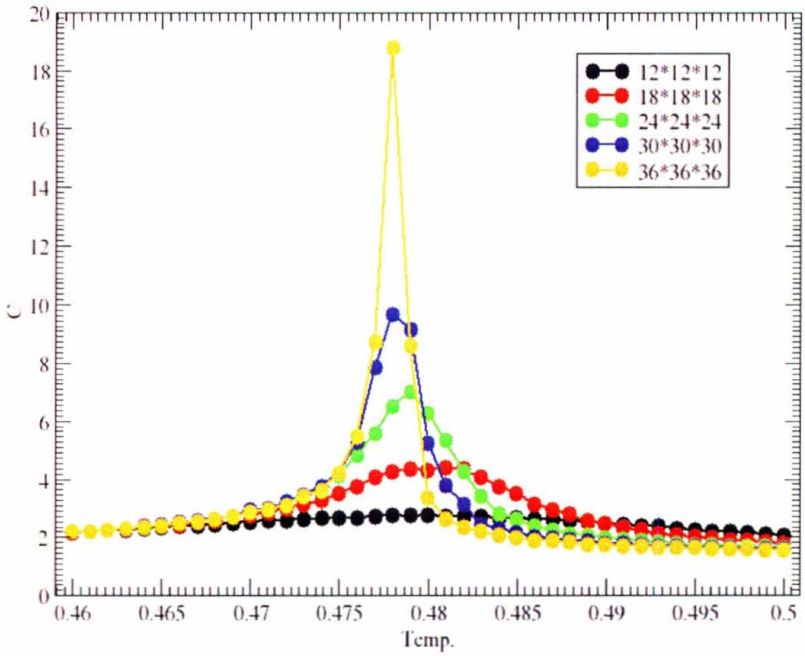

Figure 4.10: Simulation results of C of the Heisenberg fcc Kagome lattice with different lattice sizes.

As can be seen in Fig. 4.10, while the C curve with the lattice size of 12×12×12 is nearly a horizontal line. The result of 36×36×36 lattice size shows a clear peak at around T=0.4756. Also, it seems the peak of specific heat shifts to lower temperatures by increasing the lattice size, such a behavior has been reported in other simulations [28].

As Fig. 4.3 shows, the first order nature of the phase transition in the xy fcc Kagome model would appear obvious due to existence of the discontinuity in the energy at the critical temperature; however, the order of the phase transition in the Heisenberg case is ambiguous. As can be seen in Fig.4.5, this phase transition may be weakly first order or second order. The order of these phase transitions were studied by examining histograms of the internal energy. First, the internal energy of every ensemble is saved in an output file of the Monte Carlo code, then another code, in Fortran 90, produced the histograms

at each temperature. The Heisenberg fcc, xy fcc Kagome and Heisenberg fcc Kagome systems are used to produce energy histograms. The AF Heisenberg fcc is selected because the crystallographic structure of fcc lattice is close to the fcc Kagome and there are published results available from previous MC simulation which shows a first order phase transition at T=0.4470 for a lattice size of 16×16×16 [56].

As can be seen in Fig. 4.11, below (shown in A) and above (shown in C) T=0.4435, there is only one peak in the histograms, but at the temperature of T_c=0.4435, two peaks are seen. At this temperature, there is a discontinuity in the possible values for internal energy. These results have been produced in the fcc Heisenberg AF with the lattice size of 24×24×24 after 10^7 MCS through the independent temperatures process. The slight difference between critical temperature in our results and the reported results can be the effect of lattice size on critical temperature (See Fig. 4.10).

As can be seen in Fig. 4.12, the histograms of xy fcc Kagome lattice show the same pattern which observed in Heisenberg fcc AF. Below (shown in A) and above (shown in C) T= 0.760 only one peak shows the most possible energy for the system, but at T_c=0.760 two peaks appear. To compare with the Heisenberg fcc AF, these results have been produced with the same lattice size, MCS, and in the same MC process.

As can be seen in Fig. 4.4, the order of phase transition of the Heisenberg fcc Kagome lattice is not as clear as in the fcc and xy fcc Kagome. To produce more clear results, the lattice size of 60×60×60 was used to plot histograms in the independent temperatures process.

Fig. 4.13 part B shows an obvious discontinuity in energy values; therefore, a first order phase transition can be considered likely for the Heisenberg fcc Kagome lattice. Also, the discontinuity in the internal energy in the Heisenberg fcc Kagome for bigger lattice size, $36 \times 36 \times 36$ after 10^5 MCS, confirms the weakly first order phase transition in this structure (See Fig. 4.14). It is important to note that based on the definition of the Delta used to plot the data in Figs. 4.11, 4.12, and 4.13 , the scales and ranges of the Delta (x axises) depened on the values of E_{Max} and E_{Min} and are therefore not

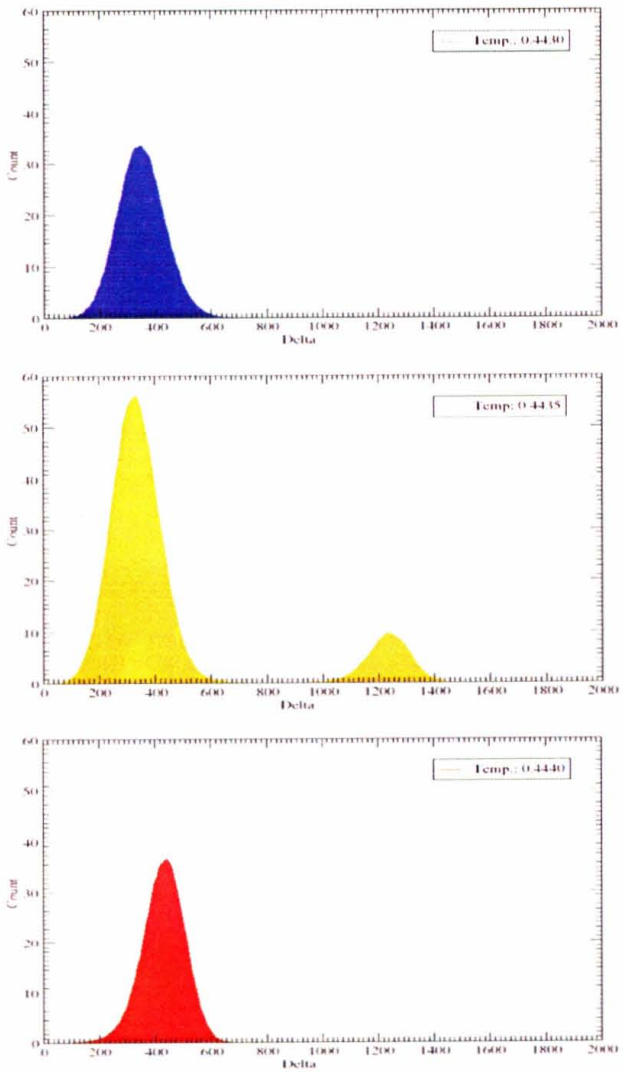

Figure 4.11: Simulation results of energy histogram in the fcc Heisenberg model at around T=0.4435.

$Delta = \frac{(|E|-|E_{Min}|)}{(|E_{Max}|-|E_{Min}|)} \times 2000$, where E_{Min} and E_{Max} are the minimum and the maximum of the calculated energy at each temperature.

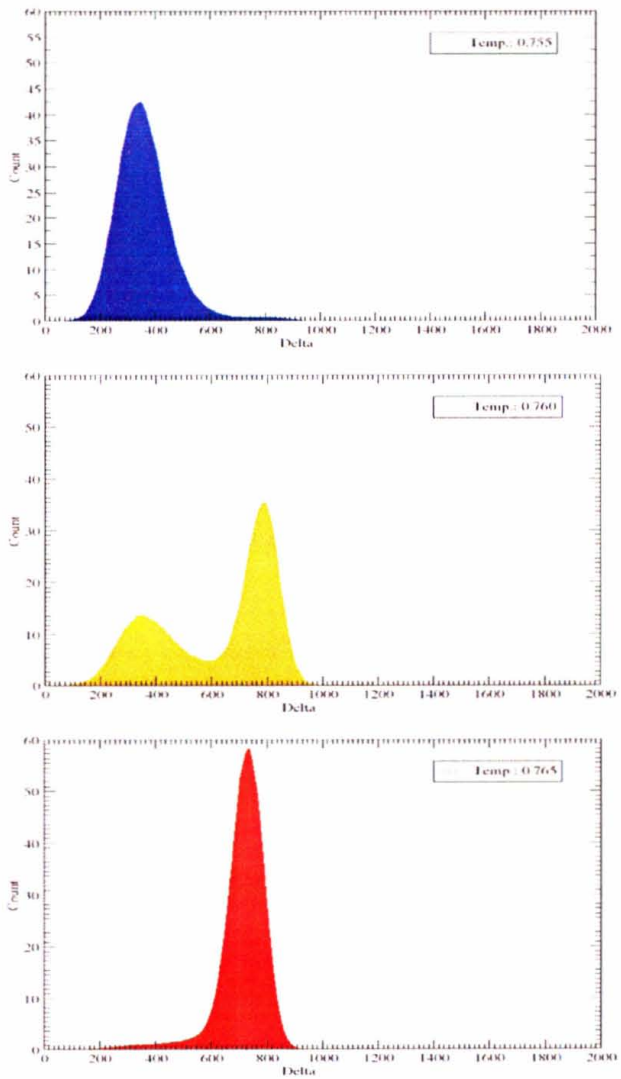

Figure 4.12: Simulation results of energy histogram in xy fcc Kagome lattice at around T=0.760.

$Delta = \frac{(|E|-|E_{Min}|)}{(|E_{Max}|-|E_{Min}|)} \times 2000$, where E_{Min} and E_{Max} are the minimum and the maximum of the calculated energy at each temperature.

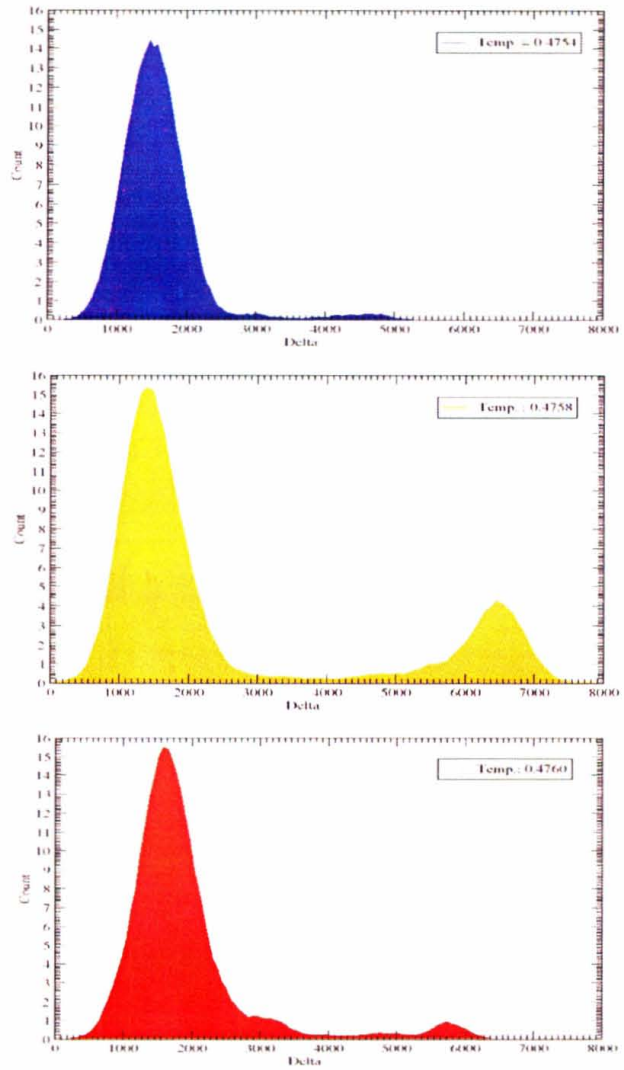

Figure 4.13: Simulation results of energy histogram in Heisenberg fcc Kagome lattice at around T=0.4758.

$Delta = \frac{(|E|-|E_{Min}|)}{(|E_{Max}|-|E_{Min}|)} \times 8000$, where E_{Min} and E_{Max} are the minimum and the maximum of the calculated energy at each temperature.

comparable at different temperatures.

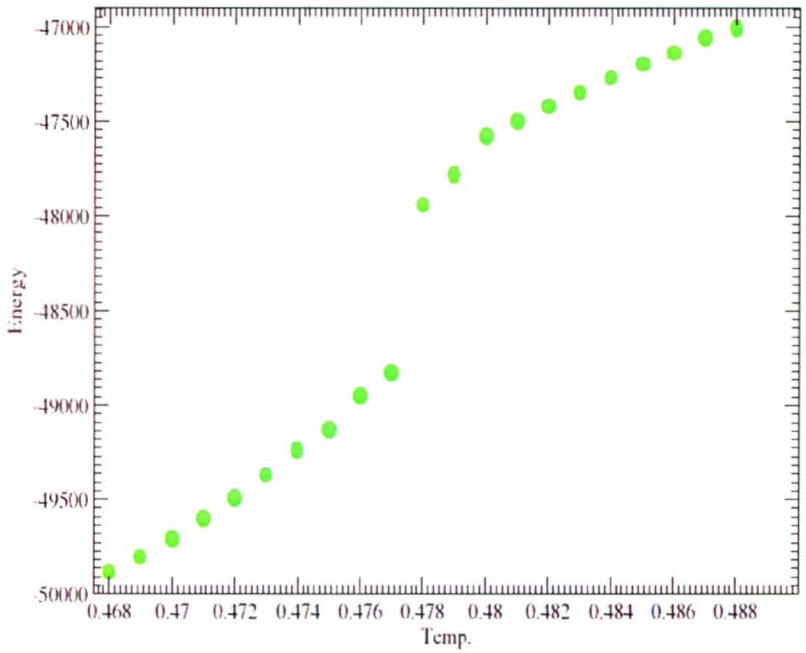

Figure 4.14: Simulation results of energy vs temperature Heisenberg fcc Kagome (L=36).

The critical temperatures of the three systems are listed in Table 4.1. There are some publications which discuss the effect of the spins degree of freedom on the value of critical temperature. Despite the fact that these studies do not focus on the fcc Kagome lattice, they outline the general effect of the degrees of freedom on the critical temperature. Adler and colleagues, based on theoretical arguments, predicted the critical temperatures of Heisenberg and xy simple cubic (sc) structures [57]. Despite the different structure, the theoretical ratio of $\frac{T_c^{Hsn}}{T_c^{Xy}}$ is around 0.655 and the simulation ratio for the fcc Kagome is around 0.626. The only 4.4 percent deviation from this theory can be the effect of the different crystallographic structures.

Another quantity which plays an important role in determining the critical temperature is the number of nearest neighbors. Because changing the number of the nearest neighbors causes a fundamental change in magnetic structure of these systems, the analogy between (Heisenberg) fcc and (Heisenberg) fcc Kagome is not trivial due to the

Table 4.1: Critical Temperatures in Heisenberg fcc, xy fcc Kagome and Heisenberg fcc Kagome

Structure	No. Nearest Neighbors	Degree of Freedom	T_c
fcc	12	3	0.4435
xy fcc Kagome	8	2	0.7600
Heisenberg fcc Kagome	8	3	0.4758

completely different magnetic order.

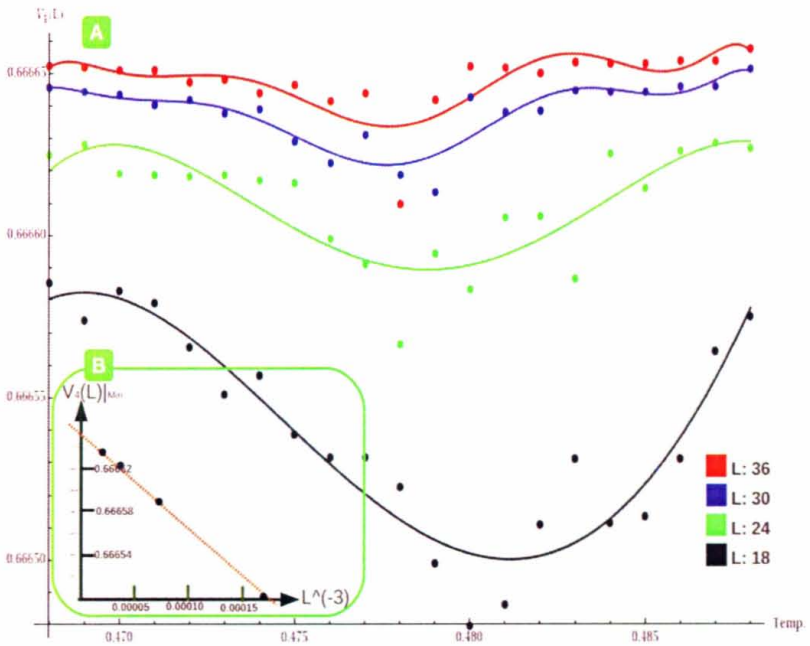

Figure 4.15: Simulation results of (A) Binder's $V_4(L)$ vs temperature, (B) Minimum of $V_4(L)$ vs L^{-3} Heisenberg fcc Kagome.

In Fig. 4.15, results for the Binder's fourth cumulant vs temperature show a minimum for each lattice size (L: 18, 24, 30, and 36)(see Sec. 1.7). The best curves are fitted to the discrete points of the Monte Carlo results with using Mathematica software. Based on the positions of minimums of these curves, the $V_4(L)|_{Min}$ vs L^{-3} is plotted in the part B of Fig. 4.15. The best fit line to the points in the part B of the figure has the slope of -0.901781. This linear behavior is almost matched with the published results shown in

Fig. 1.21, and provides further evidence of a first order transition.

4.5 Order Parameter and Spin Structure

As explained in chapter 1, the ground-state (GS) spin-configuration plays a crucial role in the definition of the OP. To study the thermal behavior of the OP in the 3D fcc Kagome lattice, we generalize the 2D q=0 GS to 3D by stacking the layers as shown in Fig. 4.2, such that the angle between nearest-neighbor spins is 120°. The q=0 GS therefore consists of three inter-penetrating sub-lattices, denoted by A, B and C, which the spins are arranged ferro-magnetically, and which are aligned at 120° to each other. While it can be shown that this spin structure does indeed minimize the energy of the system, we will show that it is not the only GS of the fcc Kagome lattice.

Based on the 3D q=0 GS and using the expressions 3.4, and 3.5, the temperature dependence of the OP for the fcc Kagome lattice has been calculated through the three processes of cooling, heating, and independent temperatures. As stated previously, our simulations show no difference in the energy of the systems for the different initializations in these processes; however, our results show a significant role of the initialization in the temperature dependence of the OP. This is a result of spin-configuration degeneracies.

Figs. 4.16 and 4.17 show the temperature dependence of the OP in the xy and Heisenberg fcc Kagome lattices, respectively. As can be seen, the OP curves obtained by heating the system from its 3D q=0 GS in both models are smooth, monotonically decreasing functions of temperature with OP=1 at zero temperature. The OP curves in the cooling process are also smooth functions of temperature, but they do not converge to the 3D q=0 GS value (See Fig. 4.2) at zero temperature (OP<1). In the case of the independent temperatures process, the fluctuations in the OP below critical temperature does not show a smooth behavior, but instead show many possible configurations which have the same energy. The fact that we simulate states with the same energy but with different values for the OP implies that the system must be highly degenerate.

Another interesting point about the results of the independent temperature process is

the quantization of the OP at zero temperature. As can be see in the figures, the values of the OPs usually lie between the heating and cooling curves. The extensions of these curves to lower temperature cross the OP axis only at some discreet points.

In order to understand this degeneracy, it is useful to examine the OP of the A, B and C sub-lattices. According to the definitions 3.4 and 3.5 which are used to calculate the OP and the sub-lattice OP, the value of each sub-lattice in the total OP of 3D q=0 GS is $\frac{1}{3}$; consequently, all calculated values shown in Fig. 4.18 and 4.19 are below $0.\bar{3}$. In the heating processes in both models, all sub-lattices, A, B, and C, follow the 3D q=0 GS alignment with a maximum possible value, $0.\bar{3}$, at zero temperature.

In cooling process, two of the sub-lattice OPs do not obtain the orientation of the 3D q=0 GS, while one of the sub-lattice OP completely matches with the 3D q=0 GS (Sub-lattice B for xy model and sub-lattice C for Heisenberg model converge to $\bar{3}$). The interesting point is that two other sub-lattices (A, C in the *xy* case, A and B in the Heisenberg case) show exactly the same deviation from the 3D q=0 GS alignment. In the *xy* system A and C sub-lattices finally converge to around 0.22, and in the Heisenberg model A and B sub-lattices converge to 1.7 at zero temperature. This means that a symmetric deviation has occurred for these two sub-lattices.

$$xy \;\; Model: \begin{cases} \Delta M_B = 0 \\ \Delta M_A = \Delta M_C \approx 0.11 \end{cases} \tag{4.2}$$

$$Heisenberg\ Model: \begin{cases} \Delta M_C = 0 \\ \Delta M_A = \Delta M_B \approx 0.16 \end{cases} \tag{4.3}$$

where $\Delta M_\eta = 0.\bar{3} - M_\eta$ and η= A, B, or C.

In independent temperatures processes, none of the curves show values lower than OP=0.15 at zero temperature. This suggests that there is a lower limit for the deviation from the 3D q=0 GS alignment. On the other hand, the majority of the calculated OP for both models in this process follow the same pattern for at least two of sub-lattices.

That the observed behavior of OP may be explained in terms of the domain wall

model discussed in Sect. 1.6.1.

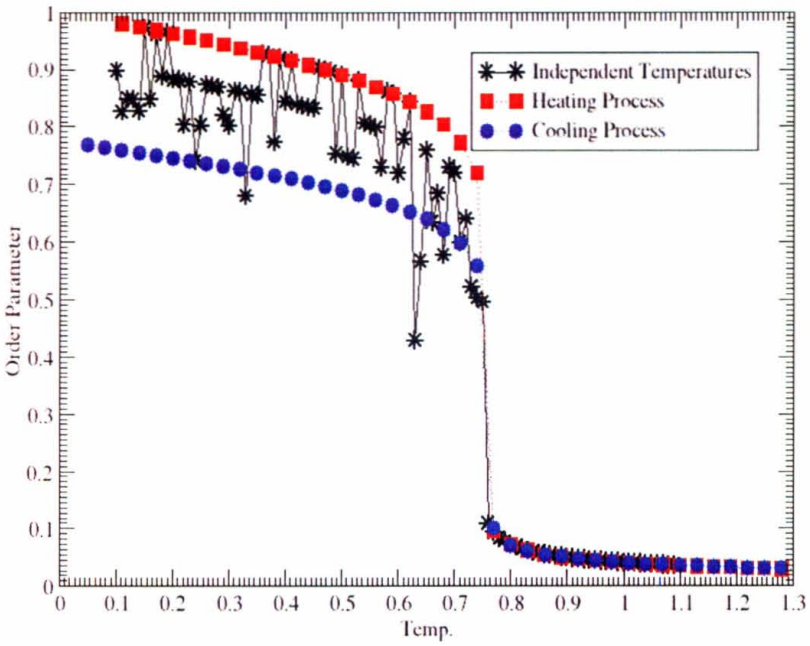

Figure 4.16: Simulation results of the OP vs temperature in the xy fcc Kagome model. L=24, MCS=10^6 (Heating and Cooling), and 10^7 (Independent Temperatures).

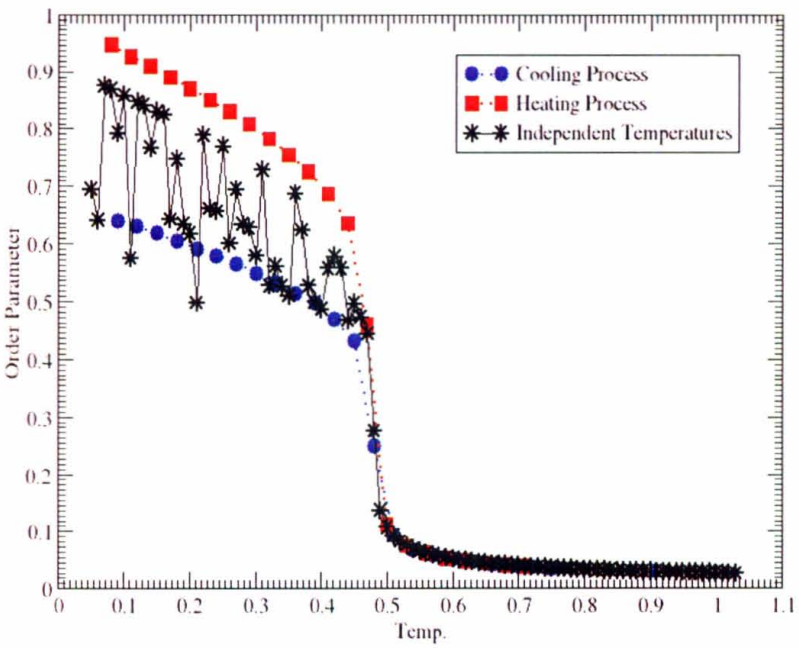

Figure 4.17: Simulation results of the OP vs temperature in the Heisenberg fcc Kagome model.

L=24, MCS=10^6 (Heating and Cooling), and 10^7 (Independent Temperatures).

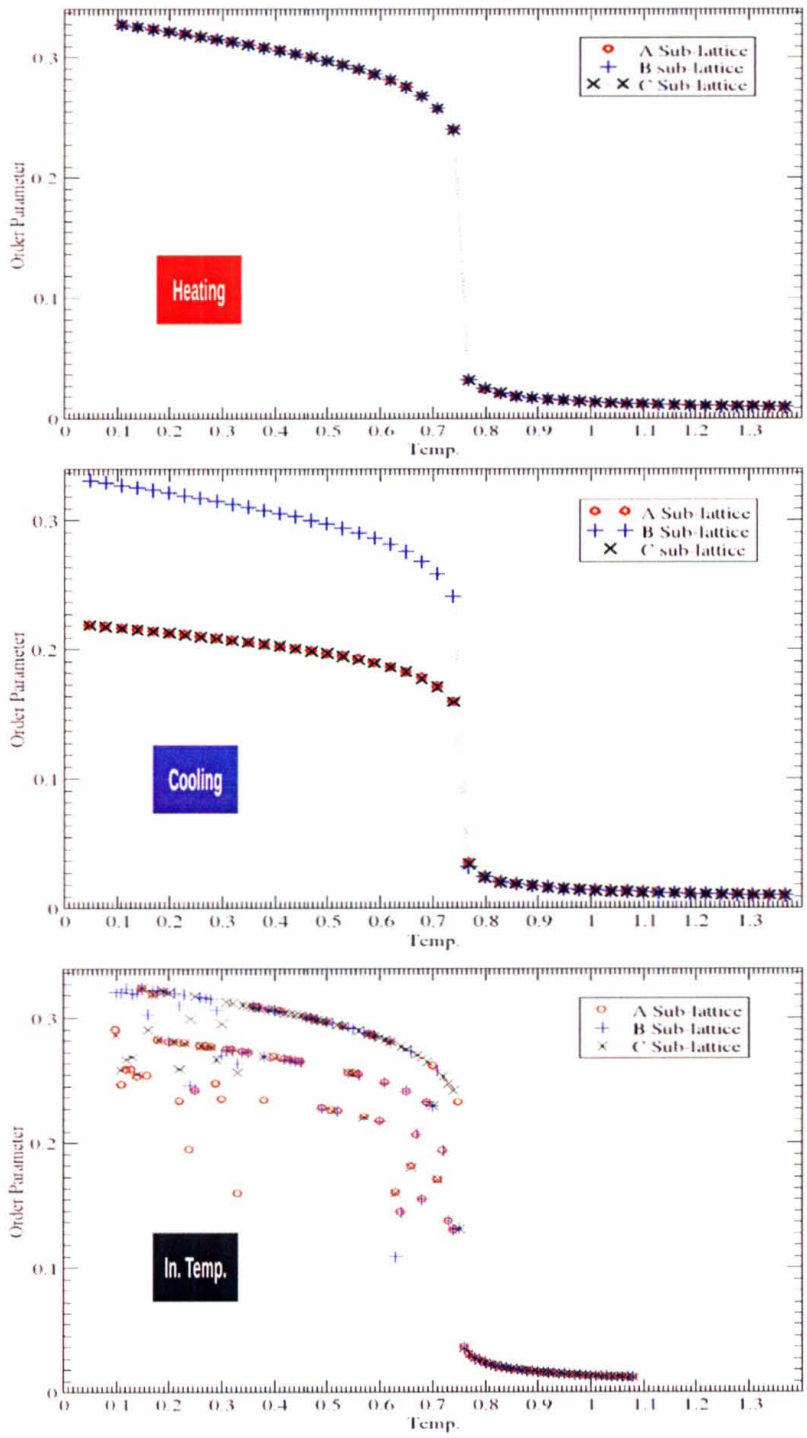

Figure 4.18: Simulation results of the sub-lattice OP vs temperature for the xy fcc Kagome lattice.

L=24, MCS=10^6 (Heating and Cooling), and 10^7 (Independent Temperatures).

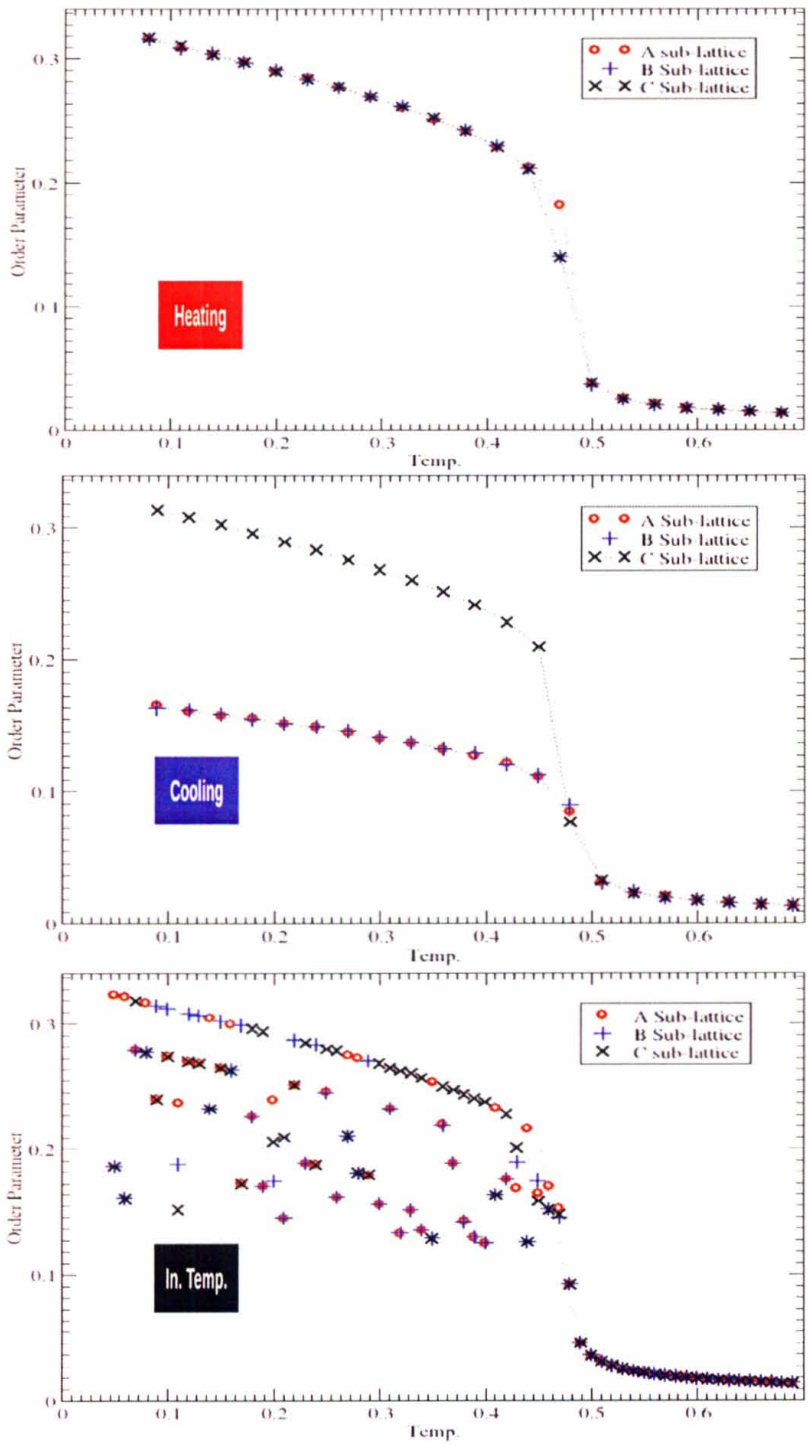

Figure 4.19: Simulation results of the sub-lattice OP vs temperature for the Heisenberg fcc Kagome lattice.

L=24, MCS=10^6 (Heating and Cooling), and 10^7 (Independent Temperatures).

4.6 A Model for Degeneracy

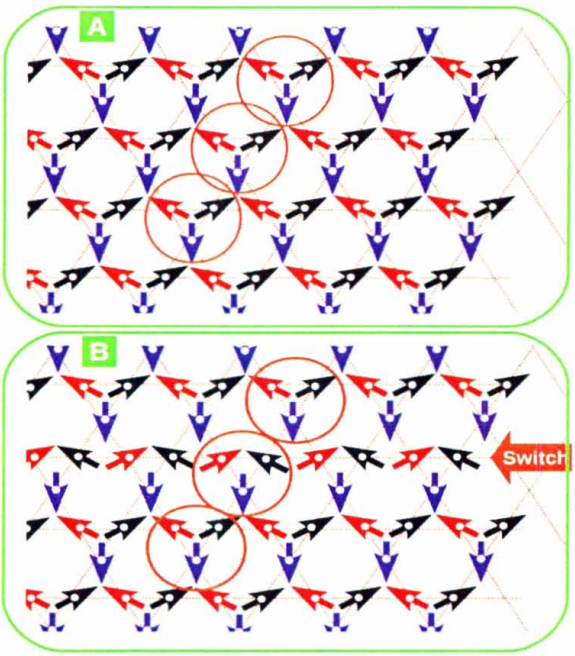

Figure 4.20: Domain wall in 2D q=0 GS.
The positions the spins of sub-lattice are shown by Blue, Sub-lattice B by red, and sub-lattice C by black

As described in Sec. 1.6.1, the locations of non-magnetic atoms in fcc Kagome lattice permit two of the sub-lattices to simultaneously rotate by the angle of 120° without any cost in the energy of the system. The result of such a rotation is shown in Fig. 4.20. As can be seen, this rotation has to affect the entire row of spins in the lattice to conserve the energy of system (part B of the figure). In the 3D system, this rotation has to occur for all spins located on a sheet in 3D space, and this sheet defines the wall of a domain. The effect of this rotation is to interchange the spins on the B and C sub-lattices, while the spins on the A sub-lattice are unchanged. The observed pattern of the sub-lattice OPs may be understood in terms of these domain walls. This possibly explains why in cooling processes one sub-lattice OP converges to $0.\bar{3}$, while the other two sub-lattices OP converge to common value that is less than $0.\bar{3}$. In the following argument, we calculate

the effect of domains on OP of sub-lattices. First we confine our system to a subset of the lattice consisting of nine spins (only including one switch in the orientation) of the lattice shown by three orange circles in Fig. 4.20. Then, the result of this simple example is expanded to whole lattice.

4.6.1 Sub-lattice OP in One B↦C Switch

Part A1 of Fig. 4.21 shows arrangement of nine spins from q=0 GS . In the diagram of spin configuration (part A2 of the figure), the spin orientation of A, B, and C sub-lattices are shown. The summation over all spins in sub-lattice C is illustrated in part A3. The magnitude of the vector, $\mathbf{R}_1$, is used to calculate the OP of Sub-lattice C (see expressions 3.4 and 3.5). As can be seen in part B1 of Fig. 4.21, the two spins in orange ellipse are switched without any cost in the energy of the system. The new diagram of the spin configuration of sub-lattices is shown in part B2 of the figure. After switching these spins, the magnitude of the (new) vector, $\mathbf{R}_2$, has to be used to calculate the OP of sub-lattice C.

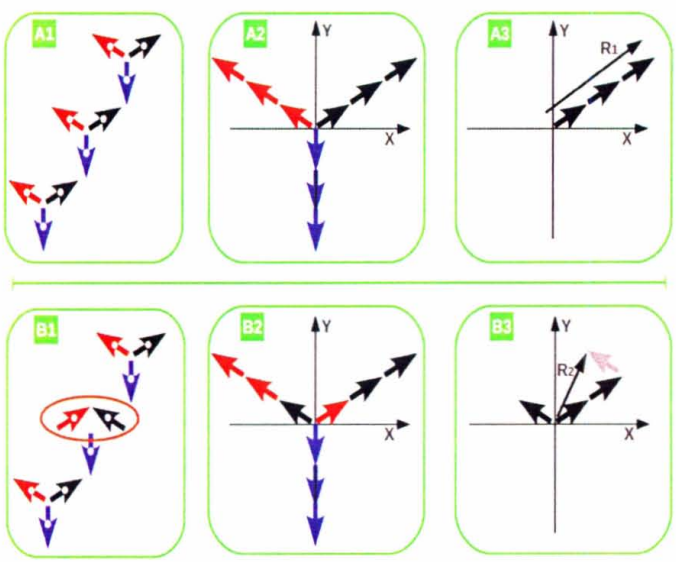

Figure 4.21: The wall affects on sub-lattice OP
The positions the spins of sub-lattice are shown by Blue, Sub-lattice B by red, and sub-lattice C by black

As shown in Fig. 4.21, the sub-lattice A (in blue) remains fixed. The order parameter of sub-lattice C, M_C, in part A3 Fig. 4.21 is given by:

$$M_C = \sqrt{M_{C,x}^2 + M_{C,y}^2} \tag{4.4}$$

$$\begin{cases} M_{C,x} = \frac{1}{N} \sum_{i \in C} S_{i,x} & \Rightarrow \quad M_{C,x} = \frac{R_{1,x}}{N} \\ M_{C,y} = \frac{1}{N} \sum_{i \in C} S_{i,y} & \Rightarrow \quad M_{C,y} = \frac{R_{1,y}}{N} \end{cases} \tag{4.5}$$

where N is the number of spins (N=9). Using Eq. 4.5 in Eq. 4.4 gives:

$$M_C = \frac{1}{N} \sqrt{R_{1,x}^2 + R_{1,y}^2} = \frac{|\mathbf{R_1}|}{N} \tag{4.6}$$

In the example shown Fig. 4.21, the $|\mathbf{R_1}|$=3 giving M_C=0.$\bar{3}$, as we expected for the perfect alignment with the ground-state. The same argument for the part B3 of Fig. 4.21 gives:

$$M_C = \frac{|\mathbf{R_2}|}{N} \tag{4.7}$$

The magnitude of $\mathbf{R}_2$ is needed to calculate the OP of sub-lattice C, It is preferred to calculate the magnitude of $\mathbf{R}_2$, as a scaler quantity, in the $X'OY'$ coordinate system instead of XOY(See Fig. 4.22).

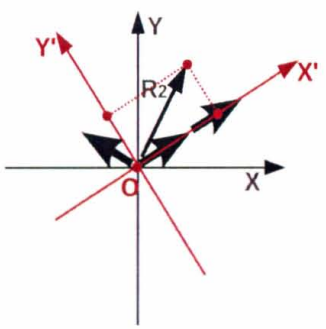

Figure 4.22: The magnitude of $\mathbf{R}_2$ remains invariant due to rotation of the coordinate system.

$$\begin{cases} R_{2,x'} = 2\,|\mathbf{S}| - \sin(30^\circ)\ \ |\mathbf{S}| = (2 - \frac{1}{2})\,|\mathbf{S}| \\ R_{2,y'} = \cos(30^\circ)\ \ |\mathbf{S}| = \frac{\sqrt{3}}{2}\ \ |\mathbf{S}| \end{cases} \tag{4.8}$$

Therefore, the magnitude of $\mathbf{R}_2$ is given by:

$$|\mathbf{R}_2| = \sqrt{R_{2,x'}^2 + R_{2,y'}^2} = \sqrt{(\frac{3}{2})^2 + (\frac{\sqrt{3}}{2})^2} \tag{4.9}$$

and the OP of sub-lattice C is:

$$M_C = \frac{|\mathbf{R}_2|}{N} = 0.1924 \tag{4.10}$$

Before expanding this example to the general case of the system with size of N×N×N, two important facts about this simple example must be noticed:

1. The OP of sub-lattices of this system are quantized. The OP is changed by switching spins and the number of switched spins are quantized. In this example, M_B and M_C change by the step of 0.14 [2].

2. The minimum value for the OP of sub-lattices B and C is 0.1924, because in the case of switching more than one spin from sub-lattice C to the orientation of sub-lattice B, the same system, with the same OP, would be reproduced. The only effect of two spins switching is only change the label of B and C sub-lattices which has no effect on the calculated values of the OP of the sub-lattices. As can be seen in Fig. 4.21, if two spins switch, a similar system to what is shown in the B2 part of the figure, would be reproduced, but a different label for B and C would appear. Generally, we can assume that switching of less than half of each sub-lattice population is effective on the OP value of the system. This fact sets a lower limit for the calculated OP which is seen in our simulation results.

4.6.2 Sub-lattice OPs in Domain Wall

To expand the result of Sec. 4.6.1 to a system with N×N×N lattice size, first we must consider the fact that only $\frac{3}{4}$ of lattice points are occupied by magnetic atoms; also, $\frac{1}{3}$ of these magnetic atoms make each sub-lattice. Therefore, in a case of spins making the

[2] the only possible values for M_B and M_C are $\{0.1924, 0.3\}$, and M_A only 0.3.

switch B↦C the components of vector $\mathbf{R}$ in the $X'OY'$ coordinate system is as follows:

$$\begin{cases} R_{x'}: & \frac{3}{4} \times N^3 \times \frac{1}{3} - n - n \ \sin(30^\circ) = \frac{1}{4} \ N^3 - \frac{3}{2} \ n \\ R_{y'}: & n \ \cos(30^\circ) = \frac{\sqrt{3}}{2} \ n \end{cases} \tag{4.11}$$

where n is the number of spins making the switch B↦C. Thus, the magnitude of the vector $\mathbf{R}$ is given by:

$$|\mathbf{R}| = \sqrt{\left(\frac{1}{4} \ N^3 - \frac{3}{2} \ n\right)^2 + \left(\frac{\sqrt{3}}{2} \ n\right)^2} \tag{4.12}$$

where the vector $\mathbf{R}$ is equivalent to $\mathbf{R}_1$ and $\mathbf{R}_2$ in the previous example. Therefore, similar to Eq. 4.7, the OP of the sub-lattice is given by:

$$M_\eta = \frac{\sqrt{\left(\frac{1}{4} \ N^3 - \frac{3}{2} \ n\right)^2 + \left(\frac{\sqrt{3}}{2} \ n\right)^2}}{\frac{3}{4} \ N^3} \tag{4.13}$$

where η can be B or C. Eq. 4.13 has interesting properties, some of these properties are as follow:

1. The calculated OP for finite lattice size (N=24 in our simulation) is quantized. The discontinuity in the sub-lattice OP, ΔM_η, in switching the n^{th} spin from one sub-lattice to another one is given by:

$$\Delta M_\eta = M_\eta(N, n) - M_\eta(N, (n-1)) \tag{4.14}$$

   Note that in only one domain wall in 2D, all of spins on one row must switch, and this means n = N/2. In the case of only one domain wall in 3D, the spins of one sheet have to switch and this means n = N/2×N/2.

2. The OP of an infinite lattice is continuous, because the ΔM_η drops to zero when lattice size goes to infinity.

$$\begin{aligned} &\mathbf{lim} \ \ \Delta M_\eta = 0 \\ &N \to \infty \end{aligned} \tag{4.15}$$

3. In the case of N=24, the population of each sub-lattice is $\frac{1}{4} \times 24^3$. The lowest OP,

M_{Min}, is in the state that half of this population switches to another sub-lattice. This means n=$\frac{1}{8} \times 24^3$=1728.

$$M_{Min} = M_\eta\,(N = 24, n = 1728) = 0.166667 \tag{4.16}$$

This means that for the fcc Kagome model the OP of sub-lattice is limited to lie in $[\frac{1}{6}, \frac{1}{3}]$.

The proposed model of switching spins in a single sheet of one sub-lattice to another one provides a possible explanation of simulation results for the OP, except at a few temperatures in independent temperatures processes where three different OPs are calculated for A, B, and C sub-lattices. It is important to recall such results are achieved only in the independent temperatures process where the simulation at each temperature starts from random configurations. One explanation for such unusual points can be the existence of some local domains in the system at finite temperature. As can be seen in Fig. 4.21, we assumed that the sub-lattice A follows the perfect pattern of the q=0 GS and the spins of this sub-lattice do not switch in our model. As a matter of fact, there is nothing special in sub-lattice A which makes this sub-lattice unique. As can be seen in the q=0 GS shown in Fig. 4.2, sub-lattices B and C also can play the role which was only assumed for sub-lattice A in our example. It is possible when the system starts to produce a spin-configuration from a random structure in some part of the sample, sub-lattice A and in other parts sub-lattices B and C take the role of non-switching sub-lattice; therefore, the calculation of OP for sub-lattices could be three different numbers. The interesting point is that such local domains structure is not observed in cooling and heating processes. This means that all the walls formed in the cooling and heating processes and majority of the points in the independent temperatures processes are parallel; however, at the unusual points (with three different sub-lattice OPs) some of the walls intersect each other. The spin-configurations at these intersections impose an extra energy on the system. In a slow cooling process, these costly spin-configurations at the intersections of the domain walls are eliminated by thermal relaxation, and finally all the domain walls

are aligned parallel. However, it may be possible to trap these costly spin-configurations in a fast cooling process (such phenomenon has not seen in our results due to slow cooling).

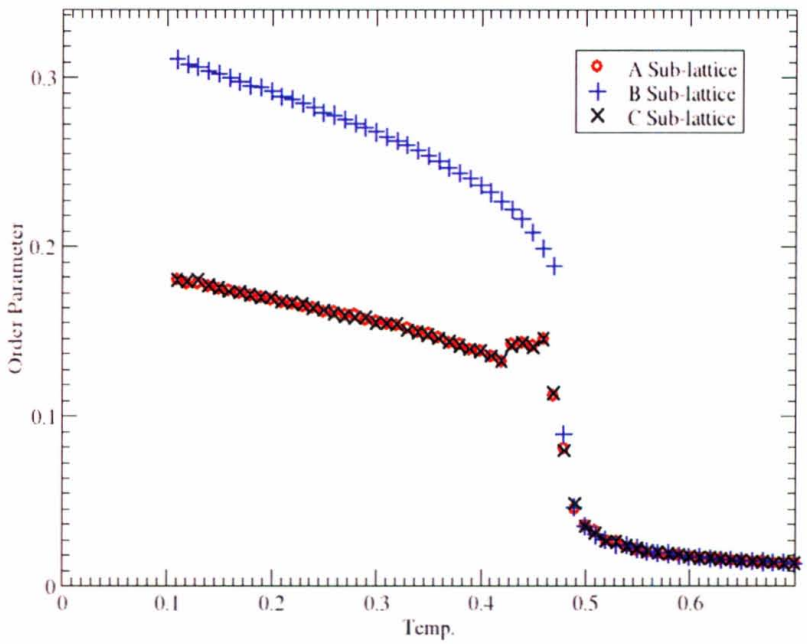

Figure 4.23: Simulation results for sub-lattices in the Heisenberg fcc Kagome model using the new algorithm.

Cooling process, L=24, MCS= 10^5

To show that the proposed model for cooling and heating processes has a physical source, another spin-updating algorithm has been used. In this new algorithm, spins for trial change are randomly chosen. Previous results are based on systematically updating spins on the lattice, row by row. This new method removes the doubt about a biased computer code. Starting from one point in the lattice and expanding the updating spin-configuration from this point may make the computer code biased, and the existence of only one sub-lattice non-switching in the entire system could be the result of this bias computer code. As can be seen in Fig. 4.23 this algorithm also gives the same pattern of only one non-switching sub-lattice (B sub-lattice) and the same value of deviation from the perfect ground-state for two other sub-lattices (A and C sub-lattices). This result

not only confirms the previous results, but also shows that the domain wall has a root in the geometry of the fcc Kagome lattice.

4.7 Suceptibility

The susceptibilities (see Sec. 1.7) for the xy and Heisenberg fcc Kagome lattices are shown in Figs. 4.24 and 4.25, respectively. The figures include only heating and cooling processes. The OP fluctuates below the critical temperature in the independent temperatures processes (see Figs. 4.16 and 4.17). The susceptibility as derivations of the OP also shows the same discontinuity for independent temperature MC runs. As a matter of fact, the heating and cooling processes explain the real procedure of studying thermal behavior of quantities such as susceptibility as this mimics the experimental procedure. The clear peaks in the simulation results of the susceptibility vs temperature in the system with the L=24 after MCS=10^6 confirm the previous results of phase transitions at T_C= 0.76 and T_C=0.47 in xy and Heisenberg models, respectively.

Results for the susceptibility of each sub-lattice as defined based on the sub-lattice OP in Fig. 4.26, these simulation results, with L=24 and after MCS=10^6, confirm the phase transitions at the previous identified critical temperatures. In addition, the figures show almost the same behavior in the heating and cooling processes. Note that the sub-lattice susceptibility in heating and cooling processes show some hysteresis, especially near the critical temperature. This is expected at a first order phase transition.

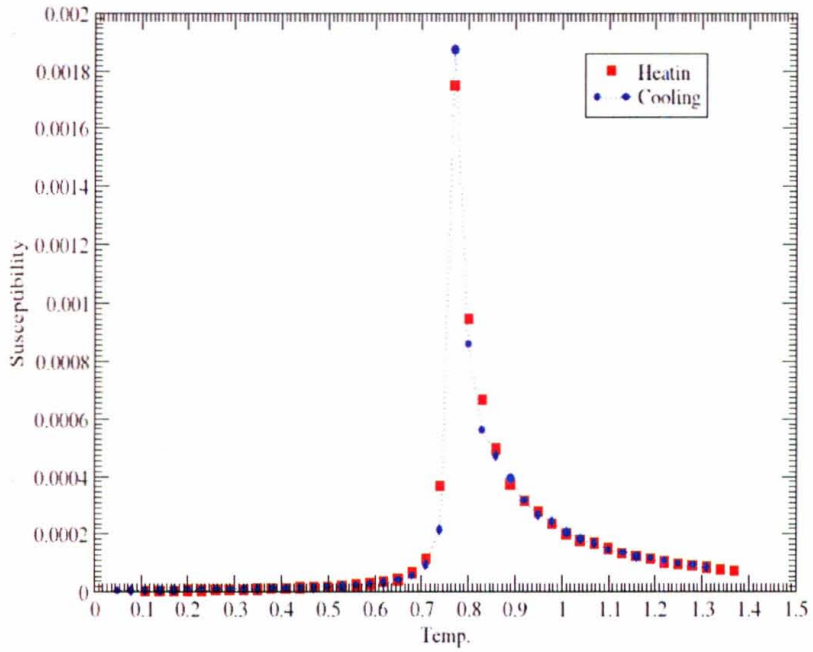

Figure 4.24: The simulation results for the susceptibility vs temperature in xy fcc Kagome lattice.

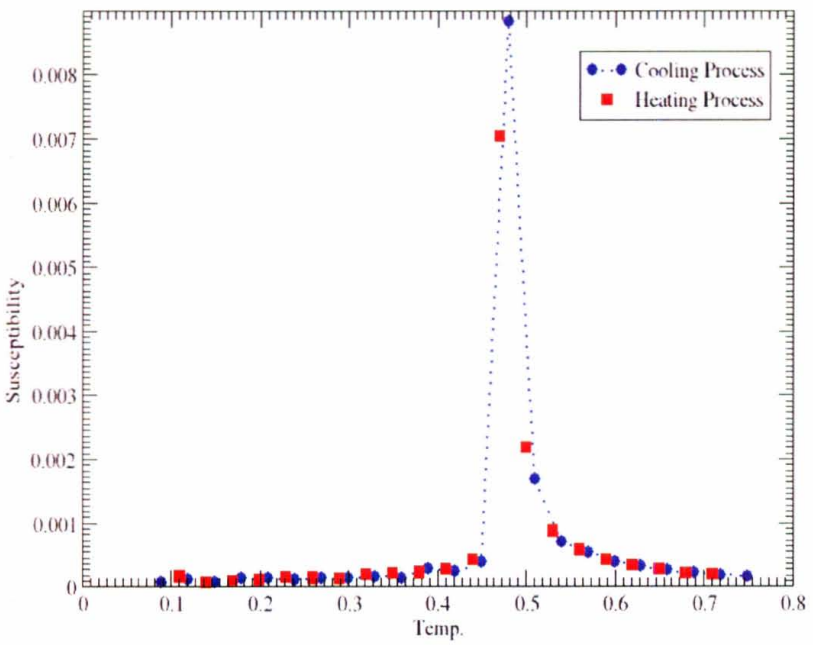

Figure 4.25: The simulation results for the susceptibility vs temperature in Heisenberg fcc Kagome lattices.

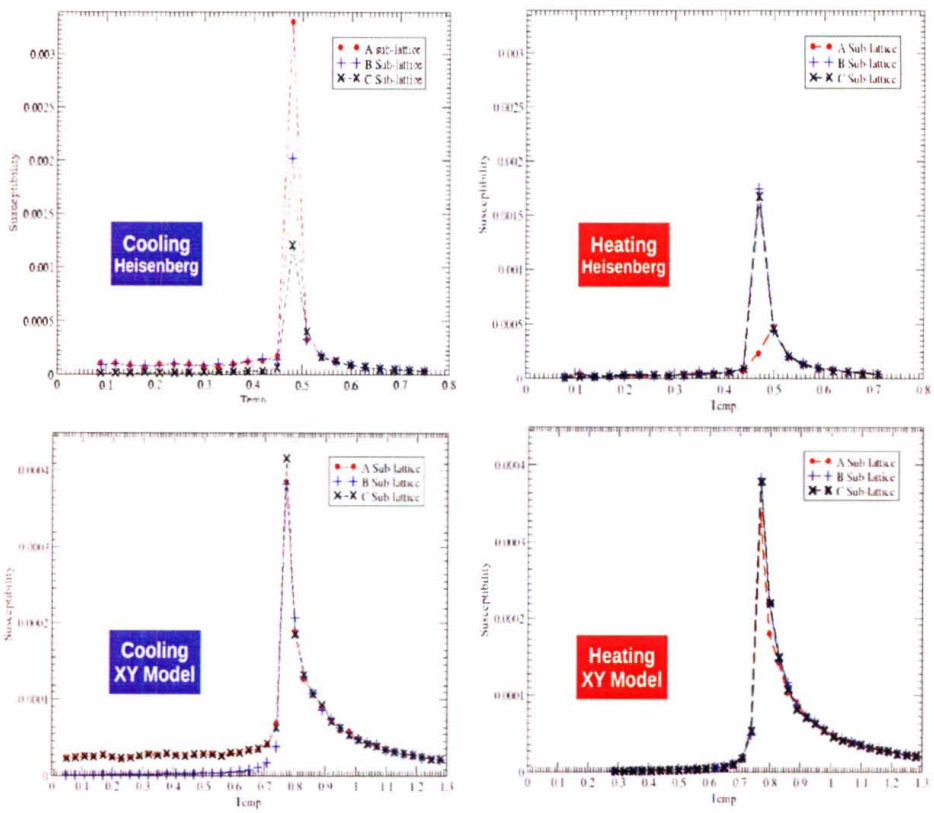

Figure 4.26: The simulation results of sub-lattices susceptibilities vs temperature for the Heisenberg and xy fcc Kagome lattice.

4.8 Magnetic Cumulant and Phase Transition

The definition of magnetic cumulant is similar to energy cumulant, but the OP replaces the energy in Eq. 1.40. The magnetic cumulant is given by:

$$V_4^M(L) = 1 - \frac{\langle M^4 \rangle_L}{3\langle M^2 \rangle_L^2} \tag{4.17}$$

Simulation results for the magnetic cumulants are shown in Fig. 4.27. All the curves converge to $0.\bar{6}$ at T=0 as expected from the definition and replacing the thermal average values for the OP (almost 1) in the ordered phase which is formed below critical temperature [26]. The important point can be the position of the minimum on these plots. The lower minimum value is related to to the strength of the first order phase transition.

In two first plots, the simulation results of the xy and Heisenberg fcc Kagome lattice with the size of L=24 are illustrated. As can be seen, in the same lattice size, the xy fcc Kagome shows a lower minimum and (from the previous results we know) stronger first order phase transition. Also by increasing the lattice size to L=36, the minimum of the curve drops down to a number around 0.35. This plot is similar to the results published by Challa and colleague [28], but the published results show negative value at minimum for the 2D square lattice.

4.9 Thin-films of the fcc Kagome Lattice

To simulate thin-films of the Heisenberg fcc Kagome lattice, we replace the periodic boundary condition (BPC) along the z-axis with free boundary condition. Removing the PBC reduces the number of bonds of the surface spins, thereby increasing the energy per spin of the system. The results from simulations performed on systems 12×12×N, N$\in$ $\{3, 6, 9, 12\}$, after MCS=10^6 are presented in Fig. 4.28. The data show the energy per spin decreasing as the number of layers decreases. This reflects the decreasing contribution of the surface spins. The specific heat plotted in Fig. 4.29 for several thicknesses. The data show that the peak with increasing thickness in the heat capacity becomes more pronounced and shifts to a higher temperature with increasing layer thickness.

Simulation results of the OP and susceptibility of the thin film are shown in Figs. 4.30 and 4.31. Note that in this quasi-2D system, we can expect that there is not a true phase transition to long range order since the model contains no anisotropy. However, the propensity toward long range order as N increases is evident in the sharpening for C vs temperature and that the peak location is converging toward the bulk value T_N=0.47.

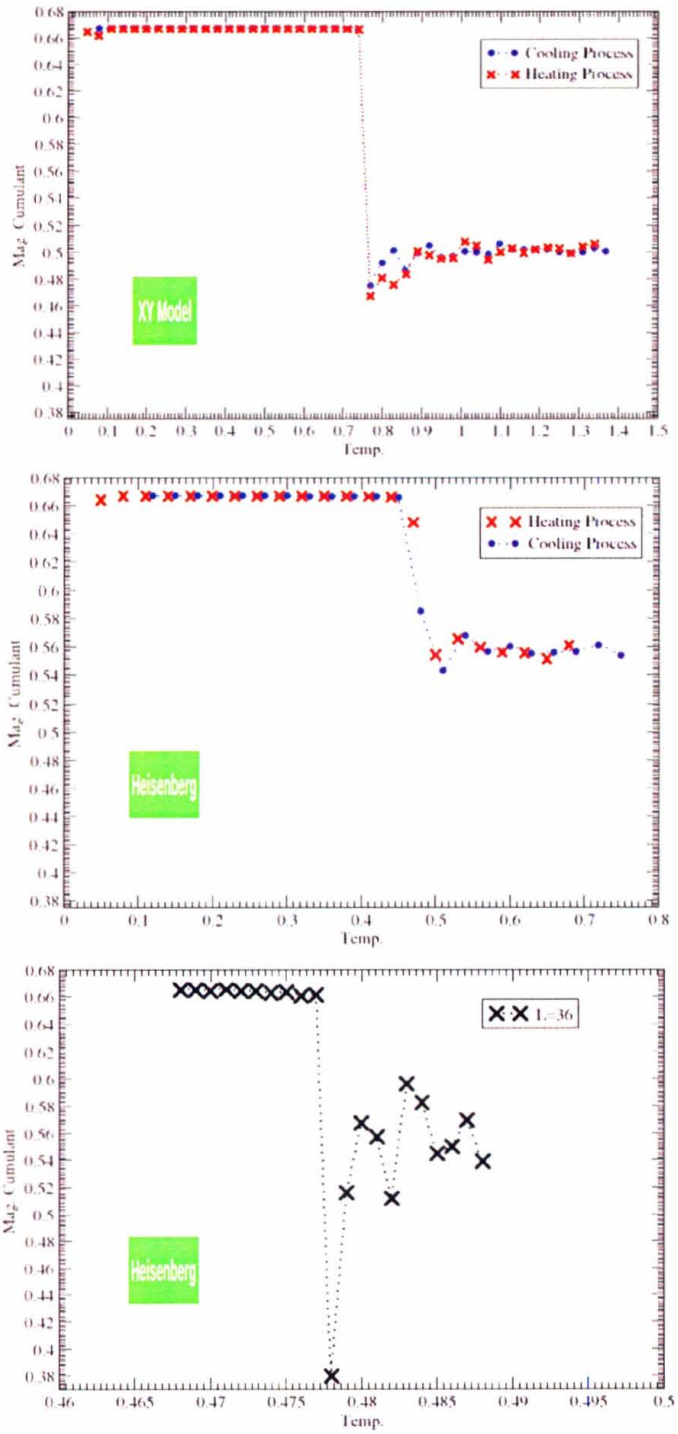

Figure 4.27: Simulation results for the magnetic cumulant vs temperature in the xy and Heisenberg fcc Kagome lattices.

In the two first plots: L=24, MCS=10^6, in the last plot: L=36, MCS=10^6.

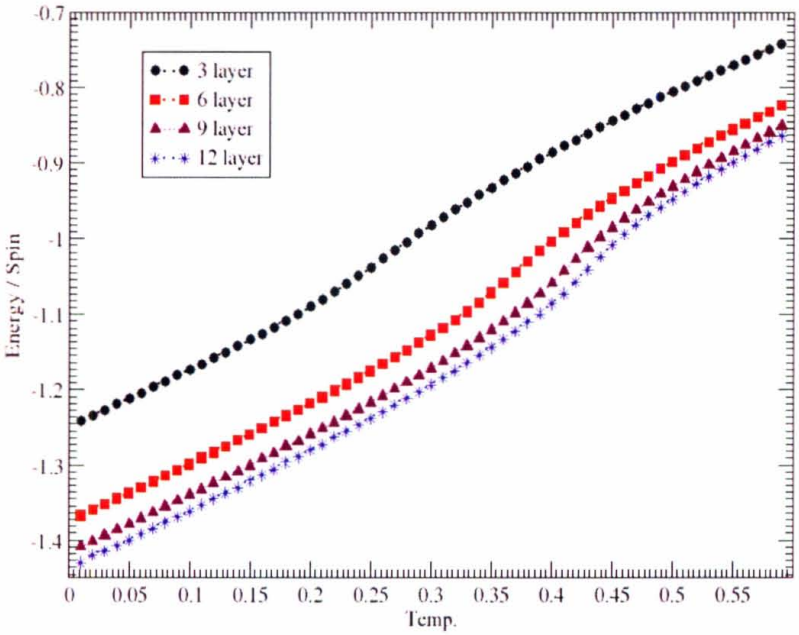

Figure 4.28: Simulation results of energy per spin vs temperature for the Heisenberg fcc Kagome thin-film.

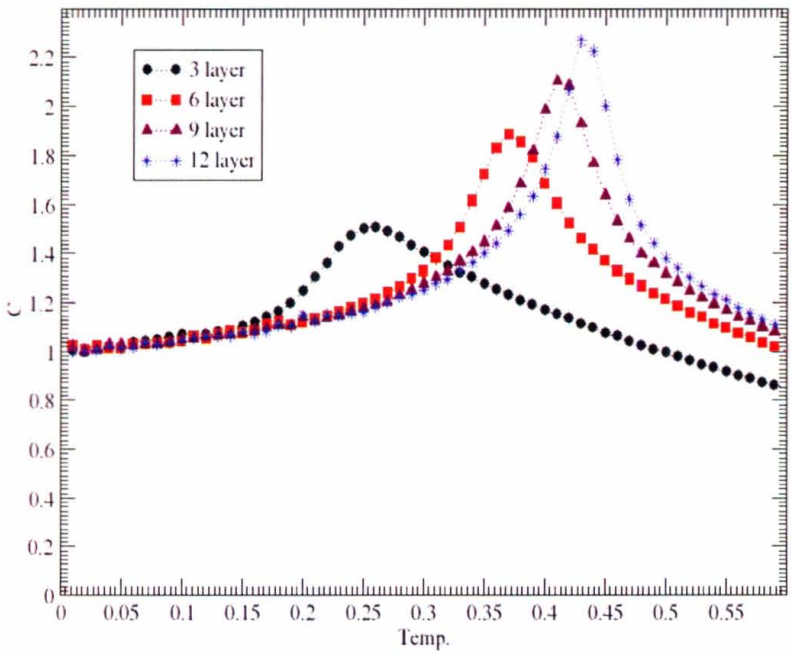

Figure 4.29: Simulation results of C vs temperature for the Heisenberg fcc Kagome thin-film.

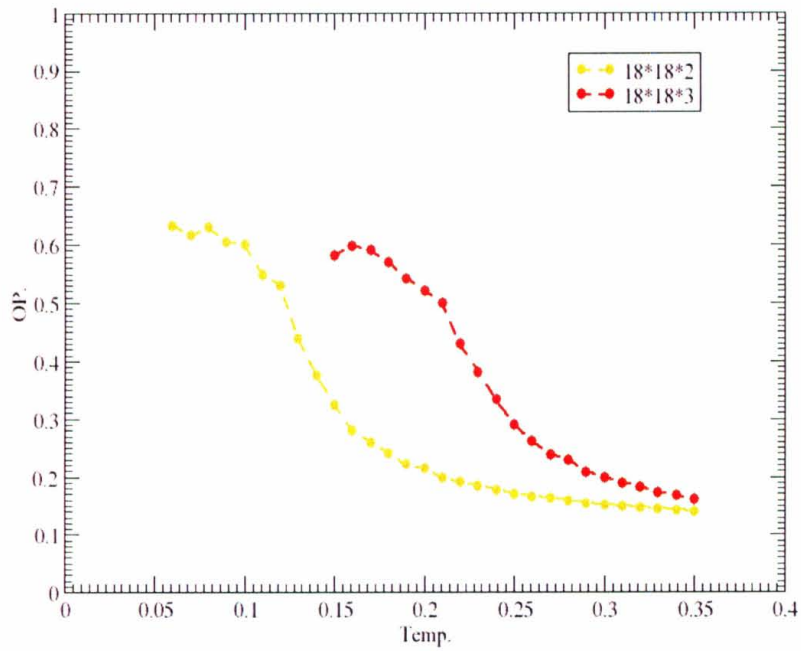

Figure 4.30: Simulation results of OP vs temperature for the Heisenberg fcc Kagome thin-film.

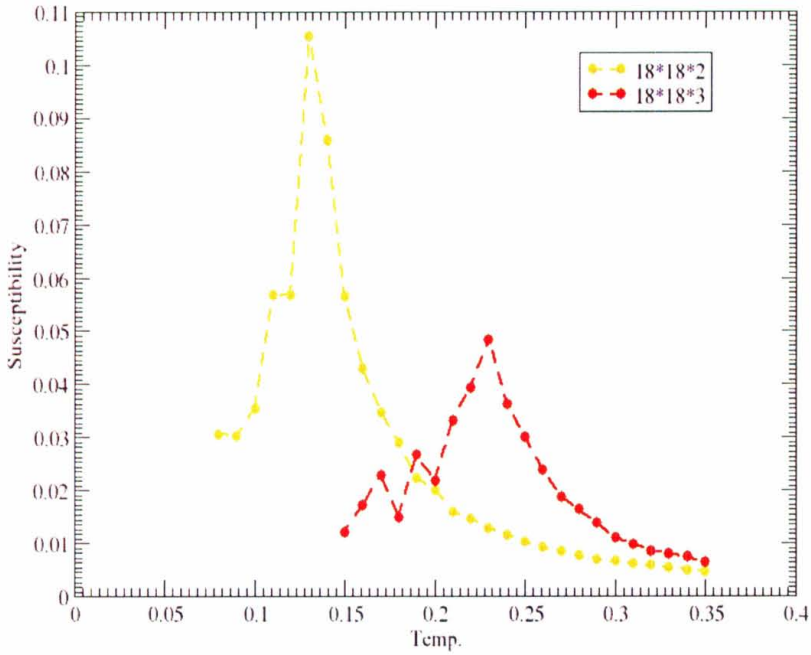

Figure 4.31: Simulation results of susceptibility vs temperature for the Heisenberg fcc Kagome thin-film.

Chapter 5
Discussion and Conclusion

5.1 Summary and Conclusion

In this thesis, $IrMn_3$ was studied to better understand its AF spin-configuration and magnetic phase transition. This alloy is widely used for pinning the magnetization of FM metals in spin-valve transducers. Various theories of exchange pinning were reviewed in order to have a general picture of this phenomenon. As explained in chapter 1, almost all the theories on exchange pinning are based on details of the AF spin-configuration in the FM/AF bi-layer. This fact was our motivation to focus on the $IrMn_3$ alloy. The Malozemoff model, explaining the exchange pinning phenomenon based on random field exchange, is widely used in the simulation of exchange pinning. According to this theory, the roughness in FM/AF interface produces domains on AF surface which reduce the idealized exchange field, H_E, to more realistic values.

The experimental results show that $IrMn_3$ has an fcc structure. No magnetic moment is detected for Ir atoms which occupy 25 percent of crystal points at the vertexes of the fcc structure. Therefore, the magnetic structure is the fcc Kagome lattice viewed as ABC stacked Kagome layers along $< 111 >$ direction. Monte Carlo computer code based on metropolis algorithm was written using Fortran 90 to simulate the Mn-ion magnetic order and phase transition. The code was first tested by simulating the 2D Kagome lattice, A-A stacked triangular lattice and pure fcc lattices. As shown in the chapter 3, our computer code is able to reproduce previously published results.

The main new results are discussed in chapter 4. The xy and Heisenberg fcc Kagome

systems were simulated through three different processes (cooling, heating, and independent temperatures). The results suggest a first order phase transitions for the xy and Heisenberg fcc Kagome lattice at T=0.76, and T=0.47, respectively. The magnetic order corresponds to three spins on a triangle forming the 120° structure, also known as 'q=0' and 'T1'. Furthermore, our results for the OP illustrate the large degeneracy of this spin-configuration. A proposed model, based on domain wall formation, seems to explain the degeneracy of this system. Formation of such domains in the fcc Kagome lattice may be a good indication that Malozemoff model is relevant for exchange pinning. Also, some preliminary simulations on thin-films have been performed. Peaks were seen in both the specific heat and the susceptibility curves of the quasi-2D system.

5.2 Future work

The indication of domain formation would be of interest to study further in thin films. The symmetry of the bulk system which gives long range order will be broken in the 2D system. This phenomenon may cause short range order observable in forming many random domains on the surface spin-configuration of the thin-film. One of the future works can be to investigate this possibility. Another important effect would be to study anisotropy terms added to the Hamiltonian on the thermal behavior of the system. As discussed in chapter 2, this term is necessary to compare model results with the real system. Also, adding a FM layer to AF thin-film and simulating the hysteresis loop would be of interest. As the simulation of exchange pining was explained in chapter 3, a random roughness is generated by removing the magnetic moments of some spins on the surface. In the case of a Kagome surface, where the existence of roughness of non-magnetic atoms in strategic locations may cause random domains, it would be interesting to check whether the random cancelation of spins is required to see exchange pinning or not.

Bibliography

[1] N. Smith, A. M. Zelterr, D. L. Yang and P. V. Koeppe, *IEEE Transaction on Magnetics.* **33**, 3385 (1997).

[2] M. Viret, D. Vignoles, D. Cole, J. M. D. Coey, W. Allen, D. S. Daniel and J. F. Greeg, *Phys. Rev. B* **53**, 8464 (1995).

[3] W. H. Meiklejohn and C. P. Bean, *Phys. Rev.* **105**, 904 (1956).

[4] D. Mauri, H. C. Siegmann, P.S. Bagus and E. Kay, *J. Appl. Phys.* **64**, 3047 (1987).

[5] I. A. Campell and A. Fert, *Ferromagnetic Materials* **3**, 3 (1982).

[6] M. N. Baibich, J. M. Broto, A. Fert, F. Nguyyen Van Dau, F. Petroff, P. Eitenne, G. Creuzet, A. Friederich and J. Chazelas, *Phys. Rev. Lett.* **61**, 2472 (1988).

[7] A. P. Malozemoff, *Phys. Rev. B* **35**, 3679 (1988).

[8] A. Scholl, F. Nolting, J. W. Seo, et al. *Appl. Phys. Lett.* **85**, 4085 (2004).

[9] T. C. Schulthess and W. H. Bulter, *Phys. Rev. Lett.* **81**, 4516 (1998).

[10] S. Lukaschuk, S. Ashkenazi, v. Lebedev and V. Steinberg, *Europhys. Lett.* **56**, 808 (2001).

[11] N. C. Koon, *Phys. Rev. Lett.* **78**, 4865 (1996).

[12] T. C. Schulthess and W. H. Butler, *J. App. Phys.* **85**, 5510 (1999).

[13] A. Mailhot, M. L. Plumer and A. Caille, *J. Appl. Phys.* **67**, 5418 (1990).

[14] H. E. Stanley, *Introduction to Phase Transitions and Critical Phenomena*, Oxford University Press, 1971.

[15] S. Blundell, *Magnetism in Condensed Matter*, Oxford University Press, 2003.

[16] W. Nolting, *Quantemtheorie des Magnettismus* **I, II**, Teubner, Stuttgart (1986).

[17] P. J. Jensen and K. H. Bennemann, *Surface Science Report* **61**, 129 (2006).

[18] Ising, Ernst (1924). "Beitrag zur Theorie des Ferro-und Paramagnetismus" (in German). Thesis, Hamburg.

[19] M. H. Krieger "Constitution of matter: mathematicaly modeling the most everyday of physical phenomena ", (University of Chicago Press),(1996)

[20] P. Bruno, *Phys. Rev. B* **39**, 865 (1989).

[21] M. L. Plumer and A. Mailhot, *Springer Proceeding in Physics* **80**, 44 (1995).

[22] A. S. Wills, A. Harrison, C. Ritter and R. I. Smith, *Phys. Rev. B* **61**, 6156 (1999).

[23] P. Mendels and F. Bert, *"International Conference on Frustration in Condensed Matter"*, (ICFCM), Sendai, (2011).

[24] Wikipedia, *http://en.wikipedia.org/wiki/*

[25] R. H. Landau, M. J. Paez and C. C. Bordeianu, *A Survey of Computational Physics: Introductory Computational Science*, Princeton University Press (2008)

[26] S. Tsai, *Brazilian Journal of Physics* **28**, 58 (1998).

[27] J. Lee and J. M. Kosterlitz, *Phys. Rev. B* **43**, 3265 (1990).

[28] M.S.S. Challa, D. P. Landau and K. Binder, *Phys. Rev. B* **34**, 1841 (1986).

[29] M. P. Allen and D. J. Tildesley, *Computer Simulation of Liquids*, Oxford University Press (1987).

[30] I. Tomeno, H. N. Fuke, H. Iwasaki, et al., *J. Appl. Phys.* **86**, 3853 (1999).

[31] A. E. Berkowitz and Kentaro Takano, *Journal of Magnetism and Magnetic Materials* **200**, 552 (1999).

[32] H. N. Fuke, K. Saito, Y. Kamiguchi, H. Iwasaki and M. Sahashi, *J. Appl. Phys.* **81**, 4004 (1997).

[33] T. Yamaoka, M. Mekata and H. Takaki, *J. Phys. Soc. Japan* **31**, 301 (1971).

[34] L. Szunyogh,B. Lazarovits, L. Udvardi, J. Jackson and U. Nowak, *Phys. Rev. B* **79**, 020403 (2009).

[35] G. Vallejo-Fernandez, L. E. Fernandez-Outon and K. O'Grady, *Appl. Phys. Lett.* **91**, 212503 (2007).

[36] N. P. Aley, G. Vallejo-Fernandez,R. Kroeger, B. Laafferty, et al. , *IEEE Trans. Magn.* **44**, 3131 (2008).

[37] R. Y. Ummetsu, M. Miyakawa, K. Fukamichi and A. Sakuma, *Phys. Rev. B* **69**, 104411 (2004).

[38] K. Selte, A. Kjekshus, A. F. Andresen and W. B. Pearson, *Acta Chem. Scand. (1947-1973)* **22**, 3939 (1968).

[39] A. Sakuma, K. Fukamichi, K. Sasao and R. Y. Umetsu, *Phys.Rev. B* **67**, 024420 (2003).

[40] L. Udvardi, L. Szunyogh, K. Palotas and P. Weinberger, *Phys. Rev. B* **68**, 104436 (2003).

[41] A. I. Liechtenstein, M. I. Katsnelson, V. P. Antropov and V. A. Gubanov, *J. Magn. Magn. Mater.* **67**, 65 (1987).

[42] H. Yasui, M. Ohashi, S. Abe, *et al.* , *J. Magn. Magn. Mater.* **104-107**, 927 (1992).

[43] R. Yamauchi, K. Fukamichi, H. Yamauchi, A. Sakuma and Echigoya, *J. Appl. Phys.* **85**, 4741 (1999).

[44] A. Sakuma,*J. Phys. Soc. Jpn.* **69**, 3072 (2000).

[45] L.R. Walker and R.E. Walstedt, *Phys. Rev. B* **22**, 3816 (1980)

[46] J. S. Kouvel, J. S. Kasper, in *Proceeding of the International Conference on Magnetism, Nottingham England* 1964,(The Physical Society, London, 1964), p. 169.

[47] A. Sakuma, *J. Phys. Soc. Jpn.* **67**, 2815 (1998).

[48] A. Sakuma, *IEEE Trans. Mag.* **35**, 3349 (1999).

[49] T. Yamaoka, *J. Phys. Soc. Jpn.* **36**, 445 (1974).

[50] M. ALi, C. H. Marrows, M. Al. Jawad, B. J. Hickey, A. Misra, U. Nowak and K. D. Usadel, *Phys. Rev. B* **68**, 214420 (2003).

[51] L. Szunyogh, L. Udvardi, J. Jackson, U. Nowak and R. Chanttrell, *Phys. Rev. B* **83**, 024401 (2011).

[52] H. B. Harris, C. Kallin and A. J. Berlinsky, *Phys. Rev. B* **54**, 2899 (1992).

[53] M. E. Zhitomirsky, *Phys. Rev. B* **78**, 094423 (2008).

[54] M. L. Plumer and A. Caille, *Phys. Rev. B* **37**, 7712 (1988).

[55] J. F. Fernandez, H. A. Farach, C. P. Poole and M. Puma, *Phys. Rev. B* **27**, 4274 (1983).

[56] H. T. Diep and H. Kawamura, *Phys. Rev. B* **40**, 7019 (1989).

[57] J. Adler, C. Holm and W. Jake, *Physica* **A201**, 58 (1993).

Appendix A

Exchange Pinning and Hysteresis Loop

A.1 Hysteresis Loop of a Ferromagnetic Material

The hysteresis loop of a ferromagnetic (FM) material shows the magnetization vs applied external field in a complete cycle. Generally, the hysteresis loop is a path-dependent curve, and for simple ferromagnets, the hysteresis loops are symmetric with respect to the magnetization axes (see Fig. A.1[1]).

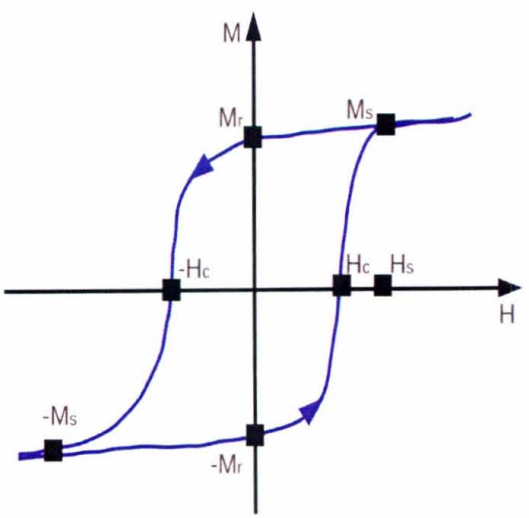

Figure A.1: Hysteresis Loop of a FM Material.

Fig. A.1 illustrates the hysteresis loop of a typical FM sample. As can bee seen, the saturation point is indicated by M_s. Beyond the saturation point, the magnetization

[1] http://uweb.txstate.edu

remains fixed. The remnant magnetization of the sample is demonstrated by M_r . The remnant magnetization is the residual magnetization when the external field is completely removed. The coercivity, H_c, shows the external field that is required to return the magnetization of system to zero. H_s displays the external magnetic field corresponding to the saturation point.

A.2 Possible Hysteresis Loop for Some FM/AF Bi-layers

As can be seen in Figure A.2, the hysteresis loop a system composed of a sandwich of thin FM and AF films can shift with respect to the origin and along the external field axis. The average of H_{C1} and H_{C2} is not zero. This loop-shift phenomenon which is seen in FM/AF multi-layers is called exchange bias.

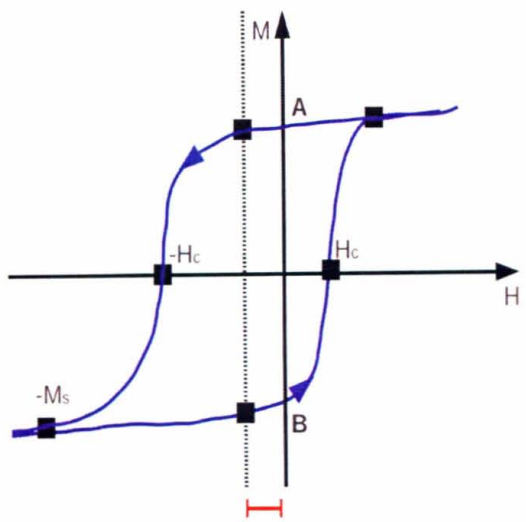

Figure A.2: Hysteresis Loop of a FM/AF Bi-layer.

The red bar in Fig. A.2 shows the exchange bias/pinning field(H_{EB}). Around the origin, the orientation of the magnetization of this system is more stable than magnetization of the simple FM layer shown in Fig. A.1. The exchange pinning field acts like an external field which pins the direction of the magnetization of the system. From Fig. A.2, it is obvious when the system is initialized in point A, a stronger negative external field

is required to flip the magnetization than corresponding point(M_r) in Fig. A.1.

Appendix B

Perl Code for Independent temperature Process:

```
#!/usr/bin/perl

system("pgf90 HK3D.f90");

for($n=24; $n<=48; $n+=6)
{
    system("mkdir File_$n");

    system("cp ./gather.pl ./File_$n");

    for($temp=0.476; $temp<=0.480; $temp+=0.0002)
    {
         system("mkdir ./File_$n/temperary_$temp");
         system("cp ./a.out ./File_$n/temperary_$temp/");
         system("echo \"$n 10000000 1 1 0.0 $temp\">./File_$n/temperary_$temp/input");

         system("echo \"#\$ -S /bin/bash\">>./File_$n/temperary_$temp/sub.sh");
         system("echo \"#\$ -cwd\">>./File_$n/temperary_$temp/sub.sh");
         system("echo \"#\$ -N Heis_Kagome_$temp\">>./File_$n/temperary_$temp/sub.sh");
         system("echo \"#\$ -j y\">>./File_$n/temperary_$temp/sub.sh");
         system("echo \"#\$ -o Heis_kagome_$temp.out\">>./File_$n/temperary_$temp/sub.sh");
         system("echo \"#\$ -l h_vmem=2000M\">>./File_$n/temperary_$temp/sub.sh");
         system("echo \"#\$ -l h_rt=480:00:00\">>./File_$n/temperary_$temp/sub.sh");
         system("echo \"./a.out\">>./File_$n/temperary_$temp/sub.sh");


         system("cd ./File_$n/temperary_$temp && qsub sub.sh");

      }
    system("cd ../../");
}
```

Note: HK3D.f90 is the name of MC simulation code in fortran 90.

Appendix C
Computer Code

The following is the Fortran90 code for the cooling process in the Heisenberg fcc Kagome lattice:

```
 program pr2
 implicit none

 real, allocatable, dimension(:,:,:) :: ph
 real, allocatable, dimension(:,:,:) :: ta
 real, allocatable, dimension(:,:,:) :: x
 real, allocatable, dimension(:,:,:) :: y
 real, allocatable, dimension(:,:,:) :: z
 real, allocatable, dimension(:,:,:) :: sx
 real, allocatable, dimension(:,:,:) :: sy
 real, allocatable, dimension(:,:,:) :: sz
 integer, allocatable, dimension(:,:,:)::s


 real, allocatable, dimension(:,:,:) :: ssx
 real, allocatable, dimension(:,:,:) :: ssy
 real, allocatable, dimension(:,:,:) :: ssz
 real, allocatable, dimension(:,:,:) :: ssxt
 real, allocatable, dimension(:,:,:) :: ssyt
 real, allocatable, dimension(:,:,:) :: sszt


 double precision ::temp,r,w,j1,j2,j3,pi,ph2,a,c,&
                    aenergy,aenergy2,aM,aM2,&
                    energy1,energy2,energy,cv,sum_x,&
                    sum_y,sum_z,nor,norm,kapa,&
                    Mx_A,Mx_B,Mx_C,My_A,My_B,&
                    My_C,Mx,My,M,MAT,MBT,MCT,&
                    aMAT,aMBT,aMCT,ta2,aM4,aenergy4,&
                    Mz_A,Mz_B,Mz_C,MATx,MATy,MATz,&
                    MBTx,MBTy,MBTz,MCTx,MCTy,MCTz,&
                    sumx,sumy,sumz,kap_A,kap_B,kap_C,&
                    aMAT2, aMBT2, aMCT2

 integer::n,i,j,k,t,p,loop,counter,mcs0,counter2,&
          si,sj,sk,mi,mj,mk,q,te

!input file contains n=lattic size, loop, mcs0=discarded loops

 n=24
 loop=100000
 j1=1.0
 j2=1.0
 j3=0.0


 allocate(ph(n,n,n))
 allocate(ta(n,n,n))
 allocate(x(n,n,n))
 allocate(y(n,n,n))
 allocate(z(n,n,n))
 allocate(sx(n,n,n))
 allocate(sy(n,n,n))
 allocate(sz(n,n,n))
 allocate(s(n,n,n))


 allocate(ssx(n,n,n))
 allocate(ssy(n,n,n))
 allocate(ssz(n,n,n))
 allocate(ssxt(n,n,n))
 allocate(ssyt(n,n,n))
 allocate(sszt(n,n,n))


call random_seed
```

```
mcs0=loop/10
pi=3.14159265


   s=1
   !Zeros
   do k=1,n
     do p=0,n-2,2
     do q=0,n-2,2
       s(2+p,2+q,k)=0
     end do
     end do
    end do


  !computing the position of each spinor
   do i=1,n
   do j=1,n
   do k=1,n
   x(i,j,k)=(i-1)*(0.5)+(j-1)+(k-1)
   y(i,j,k)=(i-1)*(0.866025404)+(k-1)*(0.577350269)
   z(i,j,k)=(k-1)*(0.816496581)
   end do
   end do
   end do


!Put out the Spin and make Kagome
   do i=1,n
   do j=1,n
   do k=1,n
   !Intial Values
     call random number(r)
       ph(i,j,k)=2*pi*r
     call random number(r)
       ta(i,j,k)=acos(1-(2*r))

   sx(i,j,k)=s(i,j,k)*cos(ph(i,j,k))*sin(ta(i,j,k))
   sy(i,j,k)=s(i,j,k)*sin(ph(i,j,k))*sin(ta(i,j,k))
   sz(i,j,k)=s(i,j,k)*cos(ta(i,j,k))
   end do
   end do
   end do




   counter2=0
  ! Temperature LOOP
   Do te=0,22!BIG TEMP
   temp=0.75-(te*0.03)

   counter2=counter2+1
   counter=0
   aenergy=0
   aenergy2=0
   aM=0;aM2=0
   ssxt=0;ssyt=0;sszt=0
   aMAT=0;aMBT=0;aMCT=0
   MATx=0;MATy=0;MATz=0
   MBTx=0;MBTy=0;MBTz=0
   MCTx=0;MCTy=0;MCTz=0
   aMAT2=0; aMBT2=0; aMCT2=0
```

```
  do t=1,loop
   counter=counter+1
do i=1,n
do j=1,n
do k=1,n
   !finding nearest neighbors
  if(s(i,j,k).eq.1)then
   si=0;mi=0;sj=0
   mj=0;sk=0; mk=0


    if (i.eq.n)then
        si=1
    else
        si=i+1
    end if
    if (i.eq.1)then
       mi=n
    else
       mi=i-1
    end if

    if (j.eq.n)then
        sj=1
    else
        sj=j+1
    end if
    if (j.eq.1)then
       mj=n
    else
       mj=j-1
    end if

    if (k.eq.n)then
        sk=1
    else
        sk=k+1
    end if
    if (k.eq.1)then
       mk=n
    else
       mk=k-1
    end if
   sum_x=sx(si,mj,k)*s(si,mj,k)+&
         sx(si,j,k)*s(si,j,k)+&
         sx(i,mj,k)*s(i,mj,k)+&
         sx(i,sj,k)*s(i,sj,k)+&
         sx(mi,j,k)*s(mi,j,k)+&
         sx(mi,sj,k)*s(mi,sj,k)+&
         sx(i,sj,mk)*s(i,sj,mk)+&
         sx(si,j,mk)*s(si,j,mk)+&
         sx(si,sj,mk)*s(si,sj,mk)+&
         sx(mi,mj,sk)*s(mi,mj,sk)+&
         sx(mi,j,sk)*s(mi,j,sk)+&
         sx(i,mj,sk)*s(i,mj,sk)
   sum_y=sy(si,mj,k)*s(si,mj,k)+&
         sy(si,j,k)*s(si,j,k)+&
         sy(i,mj,k)*s(i,mj,k)+&
         sy(i,sj,k)*s(i,sj,k)+&
         sy(mi,j,k)*s(mi,j,k)+&
         sy(mi,sj,k)*s(mi,sj,k)+&
         sy(i,sj,mk)*s(i,sj,mk)+&
         sy(si,j,mk)*s(si,j,mk)+&
         sy(si,sj,mk)*s(si,sj,mk)+&
         sy(mi,mj,sk)*s(mi,mj,sk)+&
         sy(mi,j,sk)*s(mi,j,sk)+&
         sy(i,mj,sk)*s(i,mj,sk)
```

```
 sum_z=sz(si,mj,k)*s(si,mj,k)+&
       sz(si,j,k)*s(si,j,k)+&
       sz(i,mj,k)*s(i,mj,k)+&
       sz(i,sj,k)*s(i,sj,k)+&
       sz(mi,j,k)*s(mi,j,k)+&
       sz(mi,sj,k)*s(mi,sj,k)+&
       sz(i,sj,mk)*s(i,sj,mk)+&
       sz(si,j,mk)*s(si,j,mk)+&
       sz(si,sj,mk)*s(si,sj,mk)+&
       sz(mi,mj,sk)*s(mi,mj,sk)+&
       sz(mi,j,sk)*s(mi,j,sk)+&
       sz(i,mj,sk)*s(i,mj,sk)


   energy1=0
   energy1=j1*sx(i,j,k)*sum_x+&
           j1*sy(i,j,k)*sum_y+&
           j1*sz(i,j,k)*sum_z



!chang spin direction of spin(i,j)
 ph2=ph(i,j,k)
 ta2=ta(i,j,k)

!chang spin direction of spin(i,j)
 call random number(r)
  ph(i,j,k)=2*pi*r
 call random number(r)
  ta(i,j,k)=acos(1-(2*r))


  sx(i,j,k)=sin(ta(i,j,k))*cos(ph(i,j,k))
  sy(i,j,k)=sin(ta(i,j,k))*sin(ph(i,j,k))
  sz(i,j,k)=cos(ta(i,j,k))


 !calculating new part of Spin(i,j) in energy 2
  energy2=0
  energy2=j1*sx(i,j,k)*sum_x+&
          j1*sy(i,j,k)*sum_y+&
          j1*sz(i,j,k)*sum_z



   w=exp((energy1-energy2)/temp)
   call random number(r)
  if (w.lt.r) then !not accepted return
  ph(i,j,k)=ph2
  ta(i,j,k)=ta2


  sx(i,j,k)=sin(ta(i,j,k))*cos(ph(i,j,k))
  sy(i,j,k)=sin(ta(i,j,k))*sin(ph(i,j,k))
  sz(i,j,k)=cos(ta(i,j,k))


  end if

end if! for only S(i,j,k)=1
end do
```

```
  end do
  end do
if (counter.gt.mcs0) then!discard first Mcs0
!Computing the Energy of Whole system
    energy=0
    ssx=0;ssy=0;ssz=0
    do i=1,n
    do j=1,n
    do k=1,n


    if(s(i,j,k).eq.1)then
      si=0;mi=0;sj=0
      mj=0;sk=0; mk=0


     if (i.eq.n)then
         si=1
     else
         si=i+1
     end if
     if (i.eq.1)then
        mi=n
     else
        mi=i-1
     end if

     if (j.eq.n)then
         sj=1
     else
         sj=j+1
     end if
     if (j.eq.1)then
        mj=n
     else
        mj=j-1
     end if

     if (k.eq.n)then
         sk=1
     else
         sk=k+1
     end if
     if (k.eq.1)then
        mk=n
     else
        mk=k-1
     end if
    sum_x=sx(si,mj,k)*s(si,mj,k)+&
          sx(si,j,k)*s(si,j,k)+&
          sx(i,mj,k)*s(i,mj,k)+&
          sx(i,sj,k)*s(i,sj,k)+&
          sx(mi,j,k)*s(mi,j,k)+&
          sx(mi,sj,k)*s(mi,sj,k)+&
          sx(i,sj,mk)*s(i,sj,mk)+&
          sx(si,j,mk)*s(si,j,mk)+&
          sx(si,sj,mk)*s(si,sj,mk)+&
          sx(mi,mj,sk)*s(mi,mj,sk)+&
          sx(mi,j,sk)*s(mi,j,sk)+&
          sx(i,mj,sk)*s(i,mj,sk)
    sum_y=sy(si,mj,k)*s(si,mj,k)+&
          sy(si,j,k)*s(si,j,k)+&
          sy(i,mj,k)*s(i,mj,k)+&
          sy(i,sj,k)*s(i,sj,k)+&
          sy(mi,j,k)*s(mi,j,k)+&
          sy(mi,sj,k)*s(mi,sj,k)+&
          sy(i,sj,mk)*s(i,sj,mk)+&
```

```
              sy(si,j,mk)*s(si,j,mk)+&
              sy(si,sj,mk)*s(si,sj,mk)+&
              sy(mi,mj,sk)*s(mi,mj,sk)+&
              sy(mi,j,sk)*s(mi,j,sk)+&
              sy(i,mj,sk)*s(i,mj,sk)
        sum_z=sz(si,mj,k)*s(si,mj,k)+&
              sz(si,j,k)*s(si,j,k)+&
              sz(i,mj,k)*s(i,mj,k)+&
              sz(i,sj,k)*s(i,sj,k)+&
              sz(mi,j,k)*s(mi,j,k)+&
              sz(mi,sj,k)*s(mi,sj,k)+&
              sz(i,sj,mk)*s(i,sj,mk)+&
              sz(si,j,mk)*s(si,j,mk)+&
              sz(si,sj,mk)*s(si,sj,mk)+&
              sz(mi,mj,sk)*s(mi,mj,sk)+&
              sz(mi,j,sk)*s(mi,j,sk)+&
              sz(i,mj,sk)*s(i,mj,sk)



          energy=energy+j1*sx(i,j,k)*sum_x+&
                        j1*sy(i,j,k)*sum_y+&
                        j1*sz(i,j,k)*sum_z


        ssx(i,j,k)=ssx(i,j,k)+sx(i,j,k)
        ssy(i,j,k)=ssy(i,j,k)+sy(i,j,k)
        ssz(i,j,k)=ssz(i,j,k)+sz(i,j,k)

          end if

        end do
        end do
        end do
        energy=energy/2.0
!!!!!!!!!!!!!!!!!!!!!!!!!!!!!!!!!!!!!!!!!!!!!!!!!!!
       M=0;Mx=0;My=0
       Mx_A=0; My_A=0;Mz_A=0
       Mx_B=0; My_B=0;Mz_B=0
       Mx_C=0; My_C=0;Mz_C=0
       MAT=0;MBT=0;MCT=0
        do p=0,n-2,2
         do q=0,n-2,2
           do k=1,n
            if (mod(k,2).eq.1)then
            !C:
             Mx_C=Mx_C+sx(2+p,1+q,k)
             My_C=My_C+sy(2+p,1+q,k)
             Mz_C=Mz_C+sz(2+p,1+q,k)

            !B
             Mx_B=Mx_B+sx(1+p,2+q,k)
             My_B=My_B+sy(1+p,2+q,k)
             Mz_B=Mz_B+sz(1+p,2+q,k)

            !A:
             Mx_A=Mx_A+sx(1+p,1+q,k)
             My_A=My_A+sy(1+p,1+q,k)
             Mz_A=Mz_A+sz(1+p,1+q,k)

            else
            !B:
             Mx_B=Mx_B+sx(1+p,2+q,k)
             My_B=My_B+sy(1+p,2+q,k)
```

```
            Mz_B=Mz_B+sz(1+p,2+q,k)

           !C:
            Mx_C=Mx_C+sx(2+p,1+q,k)
            My_C=My_C+sy(2+p,1+q,k)
            Mz_C=Mz_C+sz(2+p,1+q,k)

           !A:
            Mx_A=Mx_A+sx(1+p,1+q,k)
            My_A=My_A+sy(1+p,1+q,k)
            Mz_A=Mz_A+sz(1+p,1+q,k)

           end if

         end do
       end do
     end do


     MAT=sqrt(Mx_A*Mx_A+My_A*My_A+Mz_A*Mz_A)
     MBT=sqrt(Mx_B*Mx_B+My_B*My_B+Mz_B*Mz_B)
     MCT=sqrt(Mx_C*Mx_C+My_C*My_C+Mz_C*Mz_C)

     MAT=(MAT)/(0.75*n*n*n)
     MBT=(MBT)/(0.75*n*n*n)
     MCT=(MCT)/(0.75*n*n*n)


     M= MAT+MBT+MCT
!!!!!!!!!!!!!!!!!!!!!!!!!!!!!!!!!!!!!!!!!!!!!!!!
       !calculating total mag for averag


         aenergy2=aenergy2+(energy**2)
         aenergy4=aenergy4+(energy**4)
         aenergy=aenergy+energy

         MATx=MATx+Mx_A
         MATy=MATy+My_A
         MATz=MATz+Mz_A

         MBTx=MBTx+Mx_B
         MBTy=MBTy+My_B
         MBTz=MBTz+Mz_B

         MCTx=MCTx+Mx_C
         MCTy=MCTy+My_C
         MCTz=MCTz+Mz_C


         aMAT=aMAT+MAT
         aMBT=aMBT+MBT
         aMCT=aMCT+MCT

         aMAT2=aMAT2+MAT**2
         aMBT2=aMBT2+MBT**2
         aMCT2=aMCT2+MCT**2


         aM=aM+M
         aM2=aM2+(M**2)
         aM4=aM4+(M**4)
```

```
 end if!dicarding

end do!loop
 !Computing Cv and kapa
  aenergy2 = aenergy2/(loop-mcs0)
  aenergy4 = aenergy4/(loop-mcs0)
  aenergy = aenergy/(loop-mcs0)
  cv=(aenergy2-(aenergy**2))/(0.75*n*n*n*temp*temp)


   MATx=MATx/(loop-mcs0)
   MATy=MATy/(loop-mcs0)
   MATz=MATz/(loop-mcs0)

   MBTx=MBTx/(loop-mcs0)
   MBTy=MBTy/(loop-mcs0)
   MBTz=MBTz/(loop-mcs0)

   MCTx=MCTx/(loop-mcs0)
   MCTy=MCTy/(loop-mcs0)
   MCTz=MCTz/(loop-mcs0)



  aM=aM/(loop-mcs0)
  aM2=aM2/(loop-mcs0)
  aM4=aM4/(loop-mcs0)

  aMAT2=aMAT2/(loop-mcs0)
  aMBT2=aMBT2/(loop-mcs0)
  aMCT2=aMCT2/(loop-mcs0)

  aMAT=aMAT/(loop-mcs0)
  aMBT=aMBT/(loop-mcs0)
  aMCT=aMCT/(loop-mcs0)

  kapa=(aM2-(aM**2))/(temp)

 kap_A=(aMAT2-(aMAT**2))/(temp)
 kap_B=(aMBT2-(aMBT**2))/(temp)
 kap_C=(aMCT2-(aMCT**2))/(temp)

   do i=1,n
   do j=1,n
   do k=1,n
   if(s(i,j,k).eq.1)then
   ssxt(i,j,k)=(ssxt(i,j,k)+ssx(i,j,k)/(loop-mcs0))*s(i,j,k)
   ssyt(i,j,k)=(ssyt(i,j,k)+ssy(i,j,k)/(loop-mcs0))*s(i,j,k)
   sszt(i,j,k)=(sszt(i,j,k)+ssz(i,j,k)/(loop-mcs0))*s(i,j,k)
   end if
   end do
   end do
   end do

   do i=1,n
   do j=1,n
   do k=1,n

   nor=1
   if (s(i,j,k).eq.1) then
   nor=((ssxt(i,j,k)**2)+(ssyt(i,j,k)**2)+(sszt(i,j,k)**2))**(0.5)
   ssxt(i,j,k)=ssxt(i,j,k)/nor
   ssyt(i,j,k)=ssyt(i,j,k)/nor
   sszt(i,j,k)=sszt(i,j,k)/nor
   end if
```

```
      end do
      end do
      end do

      do i=1,n-1
      do j=1,n-1
      do k=1,n
           if(mod(i,2).eq.1.and.mod(j,2).eq.1)then
            sumx=ssxt(i,j,k)+ssxt(i,j+1,k)+ssxt(i+1,j,k)
            sumy=ssyt(i,j,k)+ssyt(i,j+1,k)+ssyt(i+1,j,k)
            sumz=sszt(i,j,k)+sszt(i,j+1,k)+sszt(i+1,j,k)
         !out put 4
            open(6,file='abc-4')
            write(6,*)temp,i,j,k,sumx,sumy,sumz
         end if
      end do
      end do
      end do




     !out put 1
      open(2,file='abc')
       write(2,*)temp,aM,aMAT,aMBT,aMCT

     !out put 2
      open(3,file='abc-1')
       write(3,*)temp,kapa,cv,aenergy

     !out put 3
      open(4,file='abc-2')
       write(4,*)temp,aM2,aM4,aenergy2,aenergy4

     !out put 3
      open(5,file='abc-3')
       write(5,*)temp,MATx,MATy,MATz,MBTx,MBTy,MBTz,MCTx,MCTy,MCTz


     !out put 5
      open(15,file='abc-5')
       write(15,*)temp,kapa,kap_A,kap_B,kap_C


      do i=1,n
      do j=1,n
      do k=1,n
       !out put 6
       open(16,file='spin')
       write(16,*)sx(i,j,k),sy(i,j,k),sz(i,j,k),temp
       flush(16)
    end do
    end do
    end do


end do!BIG TEMP



deallocate(ph)
deallocate(ta)
deallocate(x)
deallocate(y)
```

```
deallocate(z)
deallocate(sx)
deallocate(sy)
deallocate(sz)
deallocate(s)

deallocate(ssx)
deallocate(ssy)
deallocate(ssz)
deallocate(ssxt)
deallocate(ssyt)
deallocate(sszt)


 end program pr2
```